HI JENA

Helmholtz Institute Jena

ANNUAL REPORT 2024

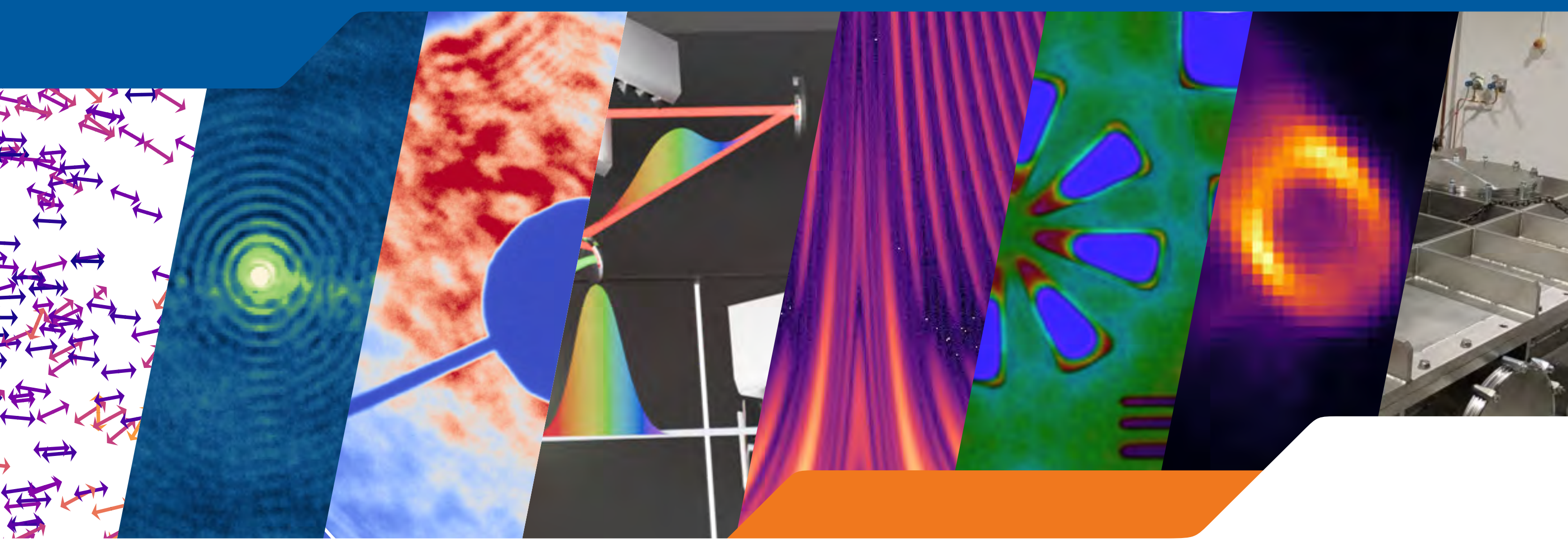

GSI

FRIEDRICH-SCHILLER-UNIVERSITÄT JENA

HZDR
HELMHOLTZ ZENTRUM DRESDEN ROSSENDORF

DESY.

HELMHOLTZ INSTITUTE JENA

ANNUAL REPORT 2024

IMPRINT

Publisher:	Helmholtz-Institut Jena, Fröbelstieg 3, 07743 Jena, Germany (http://www.hi-jena.de) @ GSI Helmholtzzentrum für Schwerionenforschung GmbH Darmstadt, Germany (http://www.gsi.de) GSI is member of the Helmholtz association of national research centers (http://www.helmholtz.de).
Editors:	Daniel Seipt and Arno Klenke
DOI:	10.15120/GSI-2025-00807
Publication date:	July 2025

CONTENTS

FOREWORD

Dear friends and members of the Helmholtz Institute Jena,

welcome to the latest collection of research activities from the Helmholtz-Institute Jena which took place during the last 12 months. This volume showcases the breadth and depth of our investigations, spanning fundamental physics to cutting-edge technological developments.

Being hosted at the campus of the FSU, the close contact of HI-Jena with the research groups from the university helped establish the high-power laser systems POLARIS and JETi200 and also specialized detector, x-ray and cryo laboratories, bolstering the institute's active involvement in the strategic missions of GSI and our partners at Helmholtz DESY and HZDR. In addition, the unique research infrastructures of the large-scale facilities at GSI and DESY are utilized in numerous experimental research projects, including the flagship projects FAIR and XFEL. In connection with the latter facilities, a joint experiment to validate the darkfield concept for vacuum birefringence was carried out during the reporting period. Based on the results, an application was submitted to carry out the most precise measurement of vacuum birefringence to date at the HIBEF beamline at the European XFEL.

We also report on the targeted exploration of QED in the strong-coupling regime, where we investigate the K_α ground-state transition in He-like uranium at the CRYRING@ESR facility, a Swedish contribution to FAIR. In this experiment, the substructure splitting of the transition was observed for the first time, using quantum sensors that offer unprecedented energy resolution compared to conventional solid-state detectors. These are just two examples of our ongoing research work, and in our current report you will find many more challenging research activities related to our central research pillars: the development of high-power lasers, laser particle acceleration, photon and particle spectroscopy as well as the corresponding theoretical activities.

In connection with the research infrastructure of our institute, considerable efforts are being invested in the development of the target area in the institute's new building, which has been in operation since 2022. This infrastructure enables joint experiments with the two laser systems JETI and POLARIS. Last year, a timing system was installed that allows the oscillators to be synchronized with a precision of less than 10 fs. The control systems are currently being upgraded so that AI can be integrated into the experimental campaigns by directly controlling the laser in response to the experimental diagnoses. In addition to the infrastructure itself, the development of suitable beam diagnostics for 'extreme' beams poses a particular challenge. Plasma wakefield accelerators are ideally suited to generate electron beams with unprecedented emittance and attosecond pulse duration. These extreme beams require a new generation of diagnostic methods that are adapted to these extreme capabilities. Recent work has shown that laser-based diagnostic methods are capable of measuring emittances in the nanometer range.

Third-party funding is of the utmost importance for all these activities and the endeavors to keep the experimental infrastructure, including equipment such as lasers and detectors, up to date. HI-Jena continues to successfully attract funding from the Free State of Thuringia and the European Regional Development Fund and in October 2024 raised over 900,000 euros for a period

Figure 1: Group photo of the HI Jena team along with members of the atomic and plasma physics departments of GSI. The photo was taken during the center evaluation at GSI in April 2025 (© Michael Lestinsky).

of two years to expand the research infrastructure. This funding is flanked by a contribution from the institute's basic funding amounting to 10 % of the total project sum. In one sub-project, a femtosecond laser system is to be installed in order to produce novel thin-film systems with atomically smooth interfaces using laser deposition and to analyze them using extreme ultraviolet (XUV) spectroscopy. A second sub-project is dedicated to modernizing the laboratory for X-ray optics by procuring a precision cutting machine equipped with X-ray diagnostics, which will enable the production of unique X-ray optics.

One focus of activities in the reporting period was the preparation of the Helmholtz Science Evaluation, which took place from 6 to 11 April 2025 at the GSI campus in Darmstadt. The originally planned on-site visit to the HI Jena was cancelled at short notice and replaced by a separate event on the GSI campus. Nevertheless, in order to provide a comprehensive impression of the institute, various lectures, including a virtual laboratory tour, and an extensive poster session with a total of 30 posters and 18 poster presentations were organized. The posters presented the scientific achievements of the institute in the POF IV period (2021–2024) as well as a detailed discussion of the scientific infrastructure of the institute on the campus of the Friedrich Schiller University. In conclusion, the results of the evaluation for the various research programs and program topics were rated as very positive and encouraging. The final step of the evaluation will be a strategic evaluation in May 2026. Preparations for this event are already underway.

The current report will also look at the Institute's public relations activities. HI-Jena has established itself as a permanent player in various public relations initiatives in Jena. In addition to joining the Particle World Network, the Institute took part in the 'Day of Physics', which is organized annually by the Faculty of Physics and Astronomy at the University of Jena to get schoolchildren and the general public interested in physics. In addition, HI-Jena also took part in the city-wide 'Long Night of Science' on 22 November 2024 with an exhibition stand and various hands-on experiments, which attracted more than 200 visitors. At this point, we would like to add that the Helmholtz Institute Jena supports the 'Weltoffenes Thüringen' initiative. This decentralized, networked initiative is intended to send out a signal that many people, institutions, associations and companies in the state are committed to a democratic, diverse and cosmopolitan Thuringia.

The young researchers, postdocs and doctoral students who are actively involved in research and the close collaboration with our partners, in particular our colleagues at the University of Jena, are crucial to the success of the institute. In this context, it should be emphasized that an ERC award has once again been acquired. An ERC Consolidator Grant was awarded to Dr. Christoph Heyl, research group leader at DESY and the Helmholtz Institute Jena, for his project 'GASONIC – Gas Phase Sonophotonics'. The research project, funded with 2 million euros over five years, will extend Dr. Heyl's pioneering work on deflecting intense laser pulses using intense ultrasound waves directly in the air. This approach was initially investigated as part of the SOPHIMA collaboration, which was supported by a wildcard grant from the Carl Zeiss Foundation.

Finally, we would like to report on the promotion of young scientists, which is a cornerstone of the institute. The Research School for Advanced Photon Science (RS-APS) at the Helmholtz Institute Jena continues to be an integral part of the institute and successfully aims to promote and support young scientists during their doctoral studies. The number of participants remains constant at between 50 and 60 doctoral students, with around half of the students being funded directly by the Institute and the other half receiving third-party funding. The proportion of female early career researchers is stable at around 20 %, while the school has a diverse international flavor, with more than 50 % of doctoral students coming from abroad. At the end of November 2024, the RS-APS and the HGS-HIRe organized their eleventh annual lecture week. The lecture week, organized in collaboration with the Helmholtz AI Consultant Team for Matter Research under the motto 'Machine Learning from Scratch', included in-depth lectures, practical programming exercises and a poster session for the participants and was very well received by the approximately 25 participating students from GSI and the affiliated universities.

This volume of research demonstrates the scientific activities and successes of 2024.

Enjoy reading.

EDUCATIONAL ENGAGEMENT

Doctoral student program and public outreach at the Helmholtz Institute Jena

R. Märtin*[1], C. Hahn[1], and G. Weber[1]

[1] *Helmholtz Institute Jena, Fröbelstieg 3, 07743 Jena, Germany*

The HI Jena is committed to the training and education of young scientists as well as to science communication to the general public with a particular focus on high school students.

For the doctoral students at the HI Jena the Research School for Advanced Photon Science (RS-APS) continues to provide a structured PhD education, supporting young scientists during their studies. The number of participants lies consistently at between 50 and 60 doctoral students, with about half of the students being directly financed by HI Jena and the other half being third-party-funded. The number of female young scientists remains stable at about 20 %, while the school exhibits a high degree of internationality with more than 50 % of the students coming from abroad. In the 2024 reporting period ten PhD students successfully graduated.

A main pillar of the graduate program is the education offered by RS-APS and its partners, namely the graduate school for Hadron and Ion Research HGS-HIRe for FAIR and the Graduate Academy Jena. In late November 2024, RS-APS and HGS-HIRe hosted the eleventh iteration of their annual Lecture Week. Organized in cooperation with the Helmholtz AI Consultant Team for Matter Research under the headline "Machine Learning from Scratch" the Lecture Week included in-depth lectures, hands-on programming exercises as well as a participant poster session, and was very well received by the about 25 attending students from HI Jena/GSI and affiliated universities.

Figure 1: Group picture taken during the Lecture Week in November 2024.

Figure 2: Members of the HI Jena at "Tag der Physik" PAF (© Falk Ronneberger/PAF).

In addition, HI Jena has established itself as a constant contributor to various outreach initiatives in Jena. Beyond its recent accession as a site partner of the federal network "Netzwerk Teilchenwelt", the institute took part in the "Tag der Physik", a yearly event organized by the Faculty of Physics and Astronomy of the University of Jena to inspire enthusiasm for physics in both high-school students and the general public. Moreover, HI Jena also joined the citywide "Lange Nacht der Wissenschaft" on 22 November 2024 with an exhibition booth and various hands-on experiments, which managed to attract more than 200 visitors. In addition Prof. Malte Kaluza gave a popular science lecture on the "Physics of string instruments" during the afternoon program of the Physics Olympics of the State of Thuringia.

High-school students with interest in getting insight view into science were again offered to work on their own scientific projects with the supported by the institute. For example, two students spent two weeks for an individual internship, one working on the trigger counter for the POLARIS Laser while the second high school student built a Geiger-Müller Counter which ended up being part of a weather ballon project on the "Tag der Physik".

To improve the outreach activities, the institute bought a CZT gamma spectrometer, which will be used in the introduction to radioactivity of high school students. In addition, a team of high school students uses the detector for their "Seminarfacharbeit" with the goal to investigate the radon exposure in various buildings.

* r.maertin@hi-jena.gsi.de

Supporting Day of Physics and Astronomy @UniJena

V. Tympel*[1,2]

[1]Helmholtz Institute Jena, Fröbelstieg 3, 07743 Jena, Germany; [2]GSI, Planckstraße 1, Darmstadt

The flight of a stratospheric balloon is an exciting undertaking and suitable to arouse an interest in the STEM (science, technology, engineering, and mathematics) subjects among high school students. The Regener-Pfotzer maximum (extremum of secondary cosmic rays) at an altitude of about 20 km is a worthwhile target that can be easily measured with Geiger-Müller counters (GMCs).

In March 2024, the Day of Physics and Astronomy 2024 took place in the main building of the Faculty of Physics and Astronomy in Jena. The faculty had invited to a foretaste of science, studies and professional life. HI Jena supported the Institute of Solid State Physics (IFK) in organizing the event. A highlight was the launch of the stratospheric balloon from the roof terrace of the main building of the faculty. The payload (Fig. 1) consisted of four measuring instruments and two transmitters, which provided live transmission of the measurement data and telemetry to the lecture hall (Fig. 2).

The radio connection was made in the 70-cm amateur radio band with the support of the German Amateur Ra-dio Club local chapter Jena (DARC X-22). The general transmitter with Automatic Packet Reporting System (APRS) was received by stations in Germany, Poland, the Czech Republic, Austria and Luxembourg and the trajectory was put on the Internet. The measurement data from the RS41 transmitter were received with an antenna on the roof of the IFK building and transmitted to the lecture hall.

For the first time, all 6 available data transfer slots were used. Three were used for Geiger Müller counters (GMC). Two GMC41 from the student soldering kit [1] with one tube each. A first test of a GMC42 with two slightly larger tubes, one of them with an energy filter (blocked $p^+ < 10$ MeV, gamma < 100 keV). The Regener Pfotzer Maximum (RP-Max) could be clearly measured (Fig. 3). GMC42 showed that the measured events had energies that the filter could not stop. The GMC41 showed that aging drift was undetectable after 10 flights. Slot#3 was a maiden flight of a GMC built by an 11th grade student from Hanover during an internship at HI Jena in February 2024. Comparisons to older measurements with the GMC41 match Indian measurements that describe an anti-correlation between RP-Max and solar activity. Flights in the next 6 years should provide more clarity here.

The results of the 3-channel spectral UV-A/B/C (ams-osram AS7331) were somewhat surprising. Unfortunately, the ozone effect at UV-C was not obvious, which was confirmed on a later second flight in August 2024.

*v.tympel@hi-jena.gsi.de

Figure 1: Payload with APRS transmitter, UV sensor, 2x GMC41, 1x GMC42, RS41 transmitter (top l. to bottom r.).

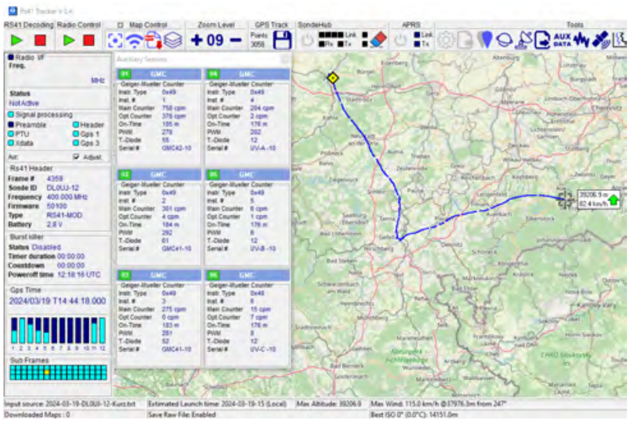

Figure 2: Decoding software RS41Tracker with measurement data of 6 slots, telemetry and trajectory on the map.

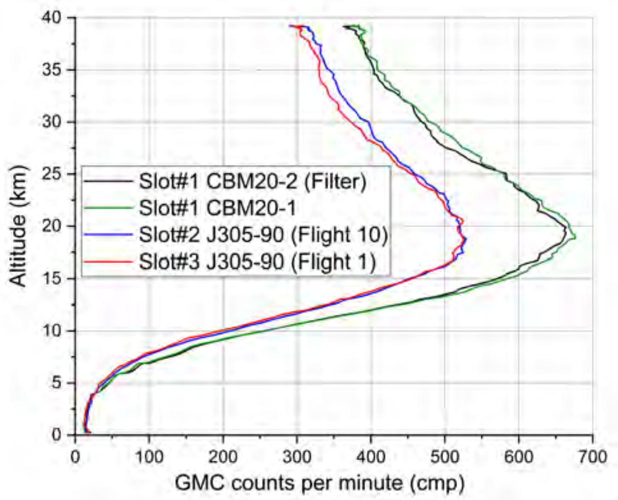

Figure 3: RPM measured with the 4 tubes, one GMC42 (CBM20, one with energy filter), two GMC41 (J305-90).

References

[1] V. Tympel, I. Kadner, *Outreach via stratosphere*, HI Jena Annual Report 2023.

HIGH POWER LASER DEVELOPMENT

Update on the Front-End Upgrade for the POLARIS Laser System

G. A. Becker*[1], M. Hornung[1,2], M. B. Schwab[1], M. Hellwing[1], F. Schorcht[2], and M. C. Kaluza[1,2]

[1]*IOQ, FSU Jena, 07743 Jena, Germany;* [2]*HI Jena, Fröbelstieg 3, 07743 Jena, Germany*

We present an update on the front-end of the POLARIS laser system including the active pulse stretcher system (AS). The output pulses of the AS were used to seed the 2nd regenerative amplifier (A2) of POLARIS for further amplification. The amplified pulses were then recompressed to the Fourier transform limit and the temporal intensity contrast (TIC) was measured.

For future experiments with the POLARIS laser system in the new target area Fraunhofer, a new pulse compressor with a monolithic grating designed for an angle of incidence of 54° will be used (described in another part of this annual report). The new AS had previously been tested at that angle [1]. However, the gain profile of the AS was not optimized at that time, resulting in a spectral bandwidth of only 17 nm (full width at half maximum (FWHM)).

To increase the bandwidth, the gain profile was shaped using tunable spectral filters [2] to support short pulse durations close to 100 fs. The AS with the improved gain profile was seeded with pulses containing 90 µJ of pulse energy that have been stretched to pulse duration of 500 fs before. These pulses were amplified and stretched in 16 passes to an energy of 200 µJ and a pulse duration of 1.3 ns. Then, the pulses passed through a DAZZLER HR45-1030 [3] to correct spectral phase aberrations before seeding the A2. The cleaned pulses could be amplified to the mJ level in the A2. After amplification, the pulses were directed to a test compressor, where they were temporally recompressed. They were then characterized using an IR-Spider [4] and a WIZZLER [3].

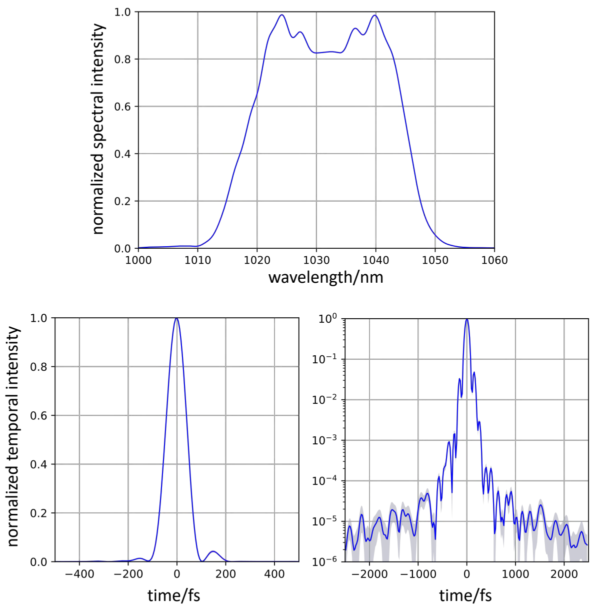

Figure 1: The top and the bottom left images show the spectral and temporal shapes of the laser pulses, respectively, measured with a Spider on a linear scale. The image on the bottom right shows a measurement averaged over 60 consecutive pulses on a logarithmic scale, as measured with a WIZZLER. The blue shaded area indicates the standard deviation of the pulse shapes.

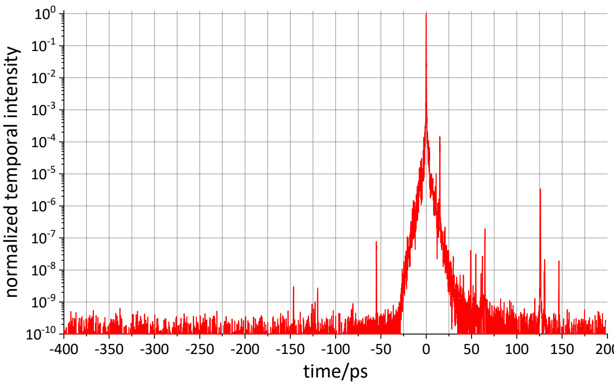

Figure 2: Temporal intensity contrast (TIC) of the laser pulses measured by a SEQUOIA.

Figure 1 shows the measured temporal and spectral shapes of the laser pulses. These measurements revealed a pulse duration of 95 fs (FWHM) and a spectral bandwidth of 27 nm (FWHM), as measured by the Spider. The WIZZLER measured 60 consecutive nearly identical pulses on a logarithmic scale, showing an average duration of (91 ± 1) fs. This result is very close to the Fourier transform limit of 90 fs.

Figure 2 shows the TIC of the laser pulses, as measured by a SEQUOIA [5]. The rising edge of the laser pulses reaches the detection threshold of the Sequoia device around -25 ps before the arrival of the pulse peak. Three pre-pulses can be identified at -148 ps, -120 ps, and -55 ps before the arrival of the pulse peak, and their origin in the AS and A2 will be investigated. The pulse shape and TIC shown here represent a significant improvement over the previously used version of the stretcher [6].

References

[1] G. A. Becker *et al.*, HI Jena Annual Report, p. 17 (2023).

[2] S. Keppler *et al.*, Opt. Lett. **41**, 4708 (2016).

[3] `https://fastlite.com`

[4] `https://www.ape-berlin.de`

[5] `https://amplitude-laser.com`

[6] H. Liebetrau *et al.*, Opt. Lett. **42**, 326 (2017).

* `georg.becker@uni-jena.de`

Gain compensation of a $Yb:CaF_2$ laser amplifier with spectral filters

M. Beyer*[1,2], C. Anschütz[1], J. Hein[1], and M.C. Kaluza[1,2]

[1] Institute of Optics and Quantum Electronics Jena, Germany; [2] HI Jena, Fröbelstieg 3, 07743 Jena, Germany

We present the process and results of designing tunable spectral filters (TSF's) to compensate for gain narrowing effects in a $Yb:CaF_2$-based, high power, ultrashort laser amplifier system. We start with a sophisticated characterization of the spectral gain of $Yb:CaF_2$ as a basis for spectral gain compensation. In order to test different TSF designs, we developed a python-based library to simulate the temporal and spectral output profile of a laser-diode pumped CPA amplifier in combination with the spectral losses of a TSF. Using this, we can determine the optimal design parameters to achieve the desired output spectrum in the A2-amplifier stage of POLARIS.

At the POLARIS laser system, the Yb:FP15 glass is limited to output fluences of $\approx 3\,\mathrm{J/cm^2}$ due to its thermo-mechanical properties. In comparison, Yb^{3+}-doped calcium fluoride ($Yb:CaF_2$) has a significantly larger thermal conductivity supporting higher output fluences and laser repetion rates [1]. However, the spectral gain is more complex, thus making the design of suitable spectral filters for broad-bandwidth laser pulses challenging. To characterize the spectral amplification of $Yb:CaF_2$, the spectrum of the amplified laser pulses as a function of the number of cavity round trips was measured. From the change in the shape of the spectrum per round trip and the measured pulse energy, the spectrally dependent small signal amplification $G_0(\lambda, \beta)$ can be determined for each wavelength. In order to gain access to parts of the gain spectrum with lower gain, a Dazzler (fastlite) was placed in transmission into the beam path to diffract central parts of the spectrum out of the cavity. The obtained results are then combined into a single curve, which can be fitted to the small signal gain

$$G_0 = (1 - L) \cdot \exp[N_{\mathrm{dop}}(\beta\sigma_{\mathrm{em}} - (1-\beta)\sigma_{\mathrm{ab}})d], \qquad (1)$$

where d is the crystal thickness, L a loss term, $N_{\mathrm{dop}} = 3.3 \cdot 10^{-20}/\mathrm{cm}^3$ the doping concentration, and $\sigma_{\mathrm{em}}, \sigma_{\mathrm{ab}}$ the absorption and emission cross sections of the material. The measured gain spectrum of $Yb:CaF_2$ is shown in Fig. 1.

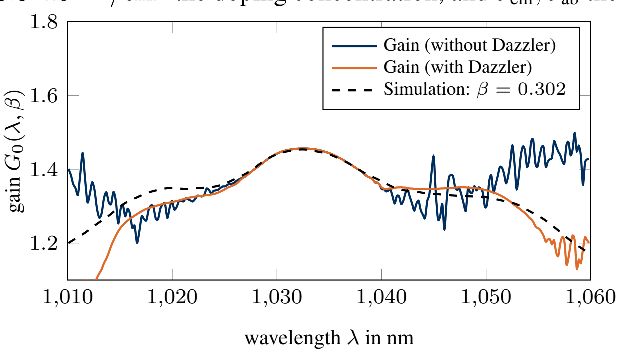

Figure 1: Spectral gain measurement of $Yb:CaF_2$ and comparison with the small signal gain G_0 (dashed line).

Tunable spectral filters (TSF) are dielectric layer systems on a glass substrate with a wavelength and angle-of-incidence dependent reflectivity. Placing them in transmission into the laser cavity allows for a precise adjustment of the spectral losses. For their design, we implemented the Frantz-Nodvik solution [2] of a 3-level system [3] for the energy extraction process in a python-based simulation. The TSF was included as a spectral loss term at each round trip in the laser cavity. To achieve a high flexibility we distributed the required reflectivity profile among four filters whose angles can be controlled independently. Using the simulation, a TSF design of a Gaussian profile with a maximum reflectivity of $4.5\,\%$ and $13\,\mathrm{nm}$ (FWHM) spectral bandwidth yielded the best results. Fig. 2 shows the simulated output spectrum of the A2-amplifier stage with an input spectrum centered at $\lambda = 1035\,\mathrm{nm}$ and a bandwidth of $28\,\mathrm{nm}$ (FWHM), which was maintained after amplification of 32 cavity round trips and a total gain of $G = 3.2 \cdot 10^3$.

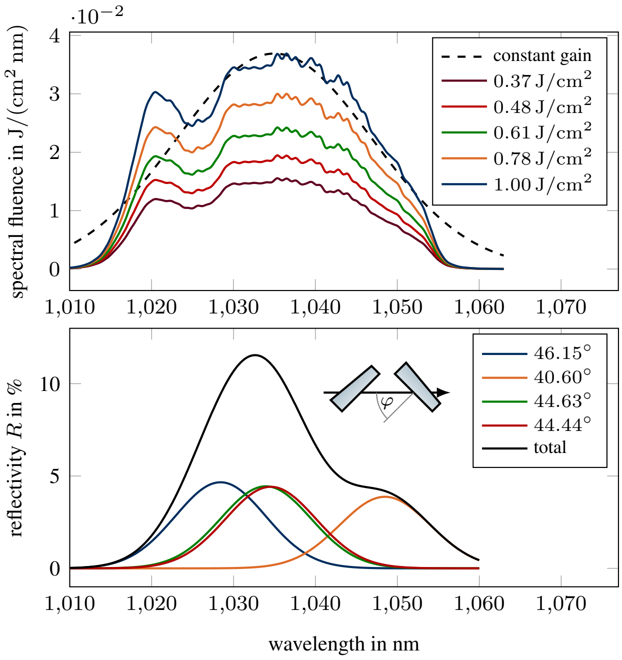

Figure 2: Top: Simulated output spectrum for the last 5 round trips in the amplifier cavity and the amplified seed spectrum with a constant gain (dashed). Bottom: Optimized angles of the TSF with the total reflectivity profile.

References

[1] S. Keppler, PhD thesis, University of Jena, (2017).

[2] L. M. Frantz and J. S. Nodvik, J. Appl. Phys. **34**, 2346 (1963).

[3] J. Körner, PhD thesis, University of Jena, (2014).

*m.beyer@uni-jena.de

Characterization of Yb:LiMgAS as a new laser material for diode-pumped, high power laser systems

M. Beyer*[1,2], M. Hellwing[1], and M. C. Kaluza[1,2]

[1] Institute of Optics and Quantum Electronics Jena, Germany; [2] HI Jena, Fröbelstieg 3, 07743 Jena, Germany

We present the spectral characterization of Yb^{3+}-doped Lithium-Magnesium-Alumino-Silicate glass (Yb:LiMgAS) as a new laser material suitable for high power laser applications at 1030 nm such as POLARIS due to its beneficial thermo-mechanical properties. We discuss its thermal lensing behaviour and characterize the spectral gain for different pump intensities showing its potential for broadband amplification.

Yb^{3+}-doped Li-Mg-Alumino-Silicate (Yb:LiMgAS) glass is a new laser material, which was first manufactured by the company Vitron [1, 2] in 2015. It exhibits similar spectral properties to the currently used Yb:FP15 glass in the POLARIS laser system, but it has a reduced thermal expansion coefficient and a higher fracture strength, promising a larger resistance to laser induced damage [3].

The cross sections (c.f. Fig. 1) of Yb:LiMgAS show broad, smooth absorption and emission bands with increased values compared to Yb:FP15 or $Yb:CaF_2$ at 1030 nm, however, this is mainly attributed to the reduced radiative lifetime of $\tau_r \approx 1\,\mathrm{ms}$ [2].

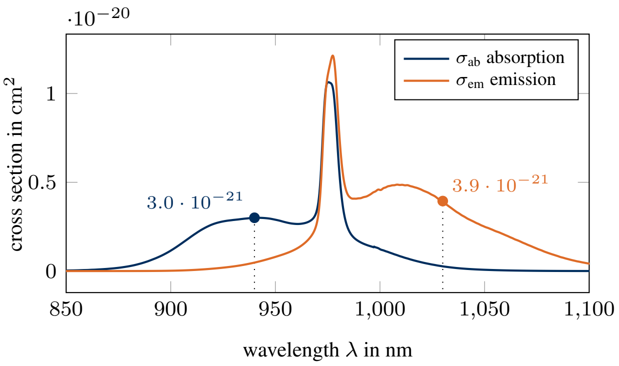

Figure 1: Absorption and emission cross sections of Yb:LiMgAS at 300 K. The spectroscopic measurements were performed by Vitron. [1]

Even though the thermo-mechanical properties of Yb:LiMgAS lead to a much higher laser induced damage threshold (LIDT) of $> 15\,\mathrm{J/cm^2}$ [2] compared to Yb:FP15 glass ($\approx 3\,\mathrm{J/cm^2}$), the new glass exhibits a strong thermal lensing effect. In a preliminary test, this was demonstrated by recording the beam profile of an alignment laser propagating through the pumped material at various pump currents as shown in figure 2. The strong lensing effect can be reduced by shortening the diode-laser pump duration to 1 ms and placing a corresponding lens with a focal length of $f = -2\,\mathrm{m}$ in front of the sample (double pass setup). This allows the formation of a stable mode in the cavity for pump intensities in a range of 40 to $50\,\mathrm{kW/cm^2}$.

*m.beyer@uni-jena.de

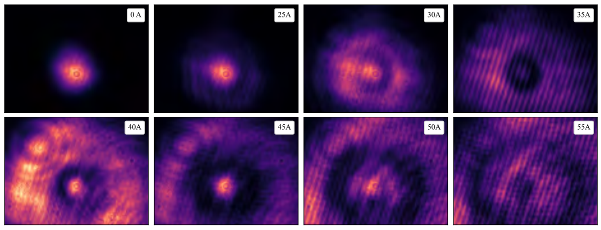

Figure 2: Beam profile of an alignment laser propagating through the pumped Yb:LiMgAS sample at different diode currents, demonstrating thermal lensing. The camera was placed at around 3 m distance to the sample.

For the gain characterization, spectra of the amplified laser pulses were measured as a function of the number of cavity round trips. The small signal gain $G_0(\lambda, \beta)$ can be determined for each wavelength from the change in the shape of the spectrum per round trip and the measured pulse energy. This is then fitted to the small signal gain

$$G_0 = (1 - L) \cdot \exp[N_{\mathrm{dop}}(\beta\sigma_{\mathrm{em}} - (1 - \beta)\sigma_{\mathrm{ab}})d], \quad (1)$$

where $d = 12\,\mathrm{mm}$ is the crystal thickness, L a loss term, $N_{\mathrm{dop}} = 6 \cdot 10^{-20}/\mathrm{cm}^3$ the doping concentration, and $\sigma_{\mathrm{em}}, \sigma_{\mathrm{ab}}$ the emission and absorption cross sections of the material. The measurement (double pass setup) is shown in Fig. 3. The spectral gain profile is very similar to Yb:FP15 glass [4], but the measured gain is larger, even though the losses L are higher due to thermal lensing.

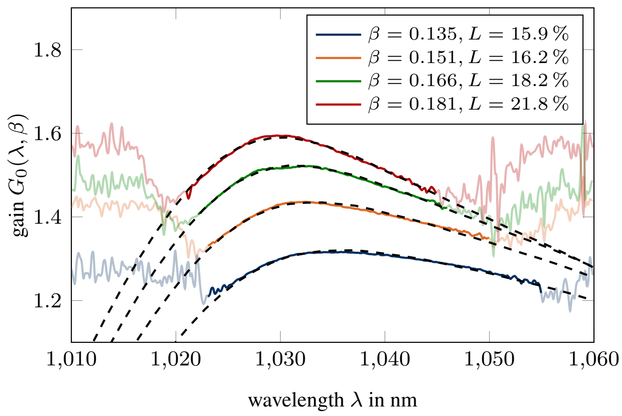

Figure 3: Spectral gain measurement of Yb:LiMgAS for different pump intensities and fit to the small signal gain.

References

[1] `https://www.vitron.de/`

[2] J. Körner *et al.*, Proc. of SPIE Vol. **9513**, 95130S (2015).

[3] M. Tiegel *et al.*, Laser Phys. Lett. **11**, 115811 (2014).

[4] M. Beyer *et al.*, HIJ annual report (2023).

Development of the Terawatt mid-IR Laser System CHROMEO

C. Anschütz*[1,2], J. Hein[1,2], and M. C. Kaluza[1,2]

[1]HI Jena, Fröbelstieg 3, 07743 Jena, Germany; [2]IOQ, FSU Jena

Various laser-driven plasma experiments such as particle acceleration or high harmonic generation can benefit from using mid-IR laser pulses as the driver [1, 2]. CHROMEO is aiming at reaching TW peak powers delivering 100 mJ pulses at 2400 nm with 100 fs duration. Following the successful development of a stretcher-compressor pair [3], the focus has shifted to the design and optimization of the amplifier chain.

After the successful design, simulation, and implementation of the stretcher and compressor module for $2400\,\mathrm{nm}$ pulses [4], the amplifier development phase has commenced. The first amplifier follows a regenerative architecture using a closed cavity formed by two concave mirrors. To account for the low saturation fluence of Cr:ZnSe ($\approx 65\,\mathrm{mJ/cm^2}$ at peak), the cavity design was optimized for a beam waist of $2.6\,\mathrm{mm}$, corresponding to a cavity length of $2500\,\mathrm{mm}$ with mirrors of $5000\,\mathrm{mm}$ radius of curvature. A RTP-based Pockels cell is employed in $\lambda/4$ mode with a double-pass configuration to reduce the risk of air breakdown under high voltage operation. As pump sources, two options are available: a custom-built cryogenically cooled Q-switched Tm:YAG laser producing up to $9\,\mathrm{mJ}$, and a commercial Tm:YAP system delivering over $10\,\mathrm{mJ}$. The cavity layout and Tm:YAP pump system, both designed using our in-house LaserCAD software [4], are shown in Figure 1.

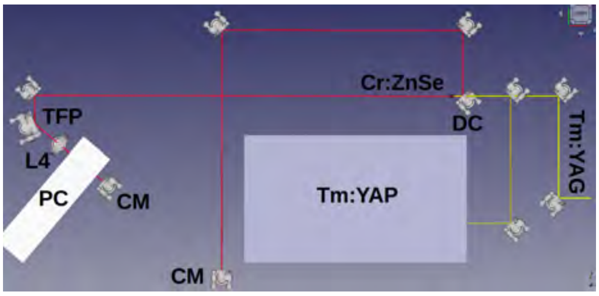

Figure 1: The regenerative amplifier's complete cavity design alongside the Tm:YLF laser, as designed with LaserCAD [4]. CM: curved mirror R=5000 mm, PC: RTP Pockels cell, L4: Quarter wave plate, TFP: thin film polarizer, DC: dichroic mirror. Both available pump laser beam lines are shown in yellow.

To address increased diffraction effects at mid-IR wavelengths, an adjustable mode adaptation telescope was developed and implemented. This allows for tuning both the input beam diameter and its complex-valued q-parameter to optimally match the regenerative cavity eigenmode. Amplification performance and saturation behavior were simulated using our new LaserSIM software [5]. The simulation results, presented in Figure 2, indicate that the regenerative amplifier is capable of boosting the pulse energy from the nJ to the mJ level.

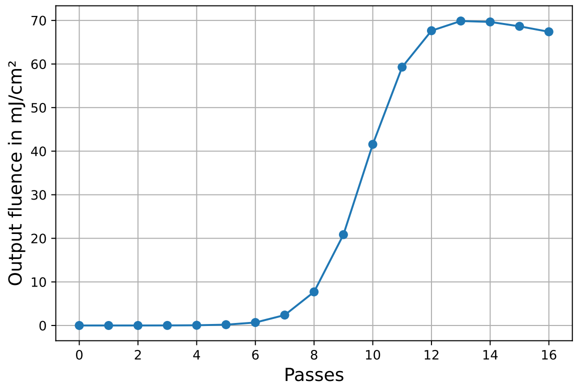

Figure 2: Simulated extraction fluence of the regenerative amplifier after each pass. A pump energy of 1 mJ and a seed energy of 5 nJ as well as a homogeneous pump profile were assumed. The simulations were done with the same tool as introduced in [5].

Initial single-pass amplification experiments already show a gain factor of 7 in the small-signal regime. Further improvements are expected by optimizing the pump mode overlap and increasing the round trip duration in the regenerative stage. Once this first stage is fully optimized and characterized, a subsequent multi-pass amplifier, pumped by the cryogenically cooled $300\,\mathrm{mJ}$ Tm:YAG system, is planned to reach the targeted energy of $100\,\mathrm{mJ}$.

References

[1] T. Gaumnitz *et al.*, Optics Express **25**, 27506 (2017).

[2] E. Esarey, C. B. Schroeder, and W. P. Leemans, Rev. Mod. Phys. **81**, 1229 (2009).

[3] C. Anschütz, J. Hein, Z. Zhang, and M. C. Kaluza, *Design of a stretcher-compressor-pair for a 2400 nm CPA system*, HI Jena Annual Report 2023.

[4] C. Anschütz, J. Hein, H. Zhuang, and M. C. Kaluza, *Description of optical design software LaserCAD*, HI Jena Annual Report 2023.

[5] M. Beyer, C. Anschütz, J. Hein, and M. C. Kaluza, *Gain compensation of a Yb:CaF$_2$ laser amplifier with spectral filters*, this report.

*clemens.anschuetz@uni-jena.de

140 W, in-band pumped, Q-switched, thulium-doped, fiber laser system delivering 7 mJ pulse energy

M. Lenski*[3], T. Heuermann[5], Z. Wang[3], C. Aleshire[3], C. Gaida[5], C. Jáuregui[3], and J. Limpert[1,2,3,4]

[1]HI Jena; [2]GSI; [3]IAP, FSU Jena; [4]IOF, Fraunhofer Jena; [5]Active Fiber Systems GmbH

A Q-switched, in-band pumped, Tm-doped MOPA sys-tem delivers 140 W average power and 7 mJ pulse energy with 77% slope efficiency. This is achieved by pumping at 1692 nm, which significantly reduces the heat load, enabling the development efficient, high-power, Tm-doped fiber lasers for demanding applications [1].

A plethora of applications in materials processing, medicine, and frequency conversion to the mid-IR and EUV spectral regions [2, 3] have created a growing demand for efficient, high-energy, high-power laser systems emitting in the 2µm range. In this context, Thulium (Tm)-doped fiber lasers constitute a promising technology due to their scalability and ability to deliver high pulse energy. However, traditionally, these lasers are pumped at 793 nm which severely limits their slope efficiency ($\approx$ 40%) due to a high quantum defect and related thermal issues. Even though a theoretical efficiency increase is possible by exploiting cross-relaxation (CR) processes, this only works reliably with low population densities of the upper laser level. Unfortunately, this requirement is difficult to meet high energy fiber laser systems, which usually rely on high inversion levels in short fibers. Therefore, in practice, there is a defacto trade-off between efficiency and high pulse energy output, as shown in Fig. 1.

To address this, our study investigates in-band pumping (1550-1900 nm) of Tm-doped fibers, which significantly reduces the quantum defect and heat load. In fact, our simulations show that an in-band wavelength between 1622-1700 nm offers a good balance between stored energy and acceptable fiber absorption length. A Q-switched, master oscillator power amplifier (MOPA) setup was developed using two 1.3m rod-type, Tm fibers; one for the oscillator and one for the amplifier. The system was tested with both 1692 nm (in-band) and 793 nm pump wavelength. The oscillator delivered 375 µJ pulses at 20 kHz. In the amplifier, in-band pumped system achieved 77% slope efficiency, more than two times that achieved by with the 793 nm pumping (32%). This yielded an average output power of 140 W and a pulse energy of up to 6.95 mJ, corresponding to 75 kW peak power.

By spectrally tuning the emission to 1888.5 nm (which falls in between two water vapor absorption lines) ensured good beam quality without the need for a special atmosphere. Our simulations confirmed that in-band pumping significantly reduces the heat load (44 W/m vs. 114 W/m for 793 nm) at higher output powers.

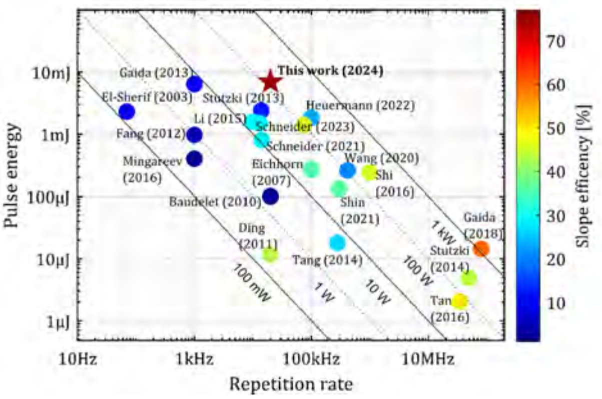

Figure 1: Published ns-class, 2 µm fiber laser systems with corresponding pulse energy, repetition rate and average power. The slope efficiency is indicated by the colorbar. The result of this work is represented by a red star (corresponding to the achived slope efficency of 77 %).

Conclusion—This system has demonstrated the highest slope efficiency (77%) ever reported for a mJ-class, Tm-doped, fiber laser system. Additionally, the system developed is a scalable, energy-efficient platform ideal for nonlinear optics applications, including mid-IR and EUV generation. Future improvements include a further pulse shortening, better fiber designs for improving in-band absorption, and beam combination techniques using multicore fibers. These improvements will allow developing J-class, Tm-doped, fiber laser systems in the future.

The authors acknowledge funding from TAB (FGR0022), FhG CAPS, ERC SALT, BMBF (13N15244, PINT), DFG (416342637, 416342891)

References

[1] M. Lenski *et al.*, Opt. Lett. **49**, 4042 (2024).

[2] X. Wie *et al.*, Opt. Laser Technol. **161**, 109135 (2023).

[3] Y. Mostafa *et al.*, Appl. Phys. Lett. **123**, 234101 (2023).

[4] M. Lenski *et al.*, Opt. Express **30**, 44270 (2022).

*mathias.lenski@uni-jena.de

Progress of the POLARIS Pulse Compressor Upgrade

M. Hornung*[1,2], M. Hellwing[2], F. Schorcht[1], T. Köhler[2], and M. C. Kaluza[1,2]

[1]*HI Jena, Fröbelstieg 3, 07743 Jena, Germany;* [2]*IOQ, FSU Jena*

We report on the current progress of the POLARIS pulse compressor upgrade. In 2024, the compressor laboratory has beren renovated including a new floor. In the refurbished laboratory we installed a new pulse compression chamber and three additional vacuum chambers for beam transport.

After the complete dismanteling of the former POLARIS pulse compressor laboratory we started the installation of a novel vacuum system for beam transport and pulse compression [1].

In Figure 1 a photo of the POLARIS compression laboratory is shown. The main compression chamber, with an inner size of 4.59 m x 1.52 m x 1.13 m above the breadboard, consists of 3 segments and was manufactured by STREICHER, spol. s r.o. Plzeň (Czech Republic). The chamber is visible in the background on the left and includes a 10 cm thick 4.5 m x 1.5 m vibration decoupled breadboard to mount the compression optics with highest stability and lowest enviromental influences. An ultimate pressure of 3×10^{-8} mbar is achieved with a very high level of cleaniness. The formerly used pulse compression chambers were reworked with adapted flange sizes and positions for the new purpose. Furthermore the fixation of the breadboards was significantly improved with respect to their stability. To achieve the highest eigenfrequencies and hence stability for the optical breadboards we have installed massive granite blocks as close as possible to the optical breadboards to connect them on the ultra-stable floor while decoupling the breadboard from the vacuum chamber with bellows.

The two circular chambers are already connected to the main compression chamber (cf. Fig. 1). The switchyard chamber (foreground in Fig. 1) handles an adaptive optics system for wavefront flattening and manages the beam transport either to the existing target area one level below the compressor laboratory or to the new target area Fraunhofer.

*The authors acknowledge funding from European Union (*EFRE, *2022 FGI 0003).*

References

[1] M. Hornung, HI Jena annual report, p. 18 (2023).

*marco.hornung@uni-jena.de

Figure 1: View into the renovated compressor laboratory. The 3-segmented main compression chamber is positioned in the background on the left. The circular grating chamber in the center of the picture and a small turning chamber are directly attached to the main compression chamber. The switchyard chamber (in the foreground) will be connected in the future via a DN320-vacuum tube to the turning chamber. Within the switchyard chamber it is possible to decide if the compressed POLARIS pulses are sent to the existing target area or will be send towards the new target area Fraunhofer.

High performance few-cycle compression in the short-wave infrared

L. Eisenbach*[1,2,3,4], Z. Wang[4], T. Heuermann[4], J. Schulte[5, 6], P. Gierschke[3, 4], P. Russbüldt[5], M. Lenski[4], R. Meyer[5], R. Klas[1, 2, 3], C. Jauregui[4], M. Sugiura[7], K. Tamura[7], C. Häfner[5, 6], J. Rothhardt[1, 2, 3, 4], and J. Limpert[1, 2, 3, 4]

[1] *HI Jena;* [2] *GSI;* [3] *IOF, Fraunhofer Jena;* [4] *IAP, FSU Jena;* [5] *ILT, Fraunhofer Aachen;* [6] *RWTH Aachen University;* [7] *Tokai Optical Co., Ltd, Japan*

The project develops ultrafast laser sources in the short-wave infrared range (1.4–3 µm, SWIR) with high pulse energies and repetition rates. Enabled by an in-house Tm-doped fiber CPA system, we achieved mJ-level, >100 W few-cycle pulses using two post-compression scheme. Sub-two-cycle pulses were generated via a gas-filled hollow-core fiber (HCF), while the multipass cell (MPC) supports 20 fs compression with 95% efficiency. These results highlight strong potential for post-compression technique in the SWIR region and its great promise for subsequent applications.

In recent years, there has been a growing interest in laser sources with high pulse energy and high repetition rates in the short-wave infrared range (1.4-3 µm) for scientific and industrial applications. Compared to established radiation sources at 1 µm, the longer wavelength provides fundamental advantages for certain nonlinear conversion processes, such as the generation of THz [1], mid infrared (mid-IR) [2] or soft X-ray radiation [3]. For efficient frequency conversion, for example by generating high harmonics (HHG), pulse durations of only a few cycles per pulse are preferred. Over the last years, we have built a high-power Tm-fiber CPA system, which delivers about 90 fs pulses with 1.6 mJ pulse energy at 101 kHz repeti-tion rate. However, for subsequent applications, pulse shortening down to few-cycle regime is demanded.

Pulse compression using HCF scheme—The first post-compression is performed using an argon-filled HCF, providing 10.2 fs pulses (sub-two cycle at 1.87 µm central wavelength). The output pulses exceed 1.3 mJ of pulse energy and >130 W of average power, presenting the highest reported average power for a sub-two-cycle SWIR source to date [4]. Moreover, the system provides an excellent output beam quality and power stability.

Pulse compression using a multipass cell—In the recent years, MPC have emerged as an effective alternative for post-compression, offering superior trans-mission and maintaining beam quality. While this method was already demonstrated successfully at the HIJ several times in recent years at 1 µm, it has, until now, not yet reached mJ-energies or >100 W power in the SWIR.

Using our in-house built laser system, it was possible to spectrally broaden pulse energies of 1.6 mJ at a repetition rate of 100 kHz at a wavelength of 1.9 µm in a krypton-filled MPC. The subsequent temporal compression achieved a pulse duration of 20 fs, which corresponds

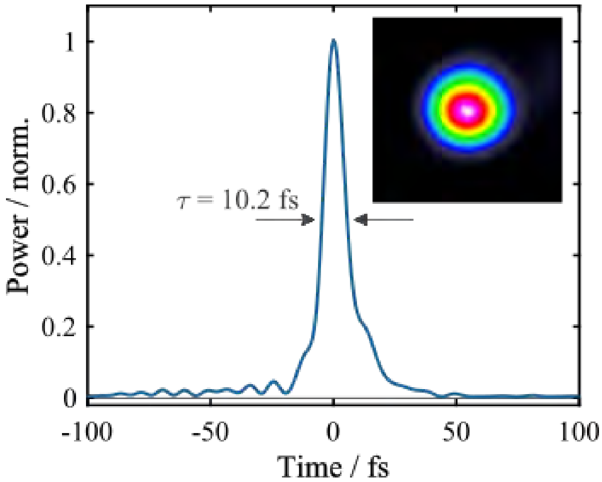

Figure 1: Retrieved output pulse profile of HCF-compression. Inset: Near-field imaged output beam profile.

to three optical cycles, at an overall transmission of 95 %. Combining the powerful Tm-laser and the excellent transmission efficiency of the post-compression stage, this achievement represents the highest average power ever reported for a sub-5-cycle SWIR source [5].

These unique results demonstrate the transferability of nonlinear compression techniques and peak power scal-ing potentials of ultrafast SWIR laser system. Moreover, the laser system serves as a powerful platform for effi-cient and broadband generation of THz, mid-IR, as well as soft X-ray in the water window.

References

[1] M. Clerici *et al.*, Phys. Rev. Lett. **110**, 253901 (2013).

[2] V. Petrov, Prog. Quantum Electron. **42**, 1 (2015).

[3] S. L. Cousin *et al.*, Opt. Lett. **39**, 5383-5386 (2014).

[4] Z. Wang *et al.*, Opt. Lett. **48**, 2647-2650 (2023).

[5] L. Eisenbach *et al.*, J. Phys. Photonics **6** 035015 (2024).

*lucas.eisenbach@uni-jena.de

Efficient amplification scheme for few-cycle laser pulses using an optical parametric multi-pass cell amplifier

S. Rajhans *[1] and C. M. Heyl[1,2,3]

[1] *Deutsches Elektronen-Synchrotron DESY, Notkestraße 85, 22607 Hamburg;* [2] *HI Jena, Fröbelstieg 3, 07743 Jena, Germany;* [3] *GSI Helmholtzzentrum für Schwerionenforschung GmbH, Planckstraße 1, 64291 Darmstadt*

Multi-pass cell (MPC) based post-compression offering high transmission, large compression factors, and excellent beam quality is a key technology for ultrafast laser source development. However, it is limited in spectral tunability and temporal contrast. In contrast, optical parametric chirped pulse amplification (OPCPA) provides superior spectral tunability and temporal contrast, but suffers from low pump-to-signal conversion efficiency (<20%) and suboptimal beam quality. Here we present a novel hybrid approach — the optical parametric multi-pass cell (OPMPC) amplifier, combining the strengths of MPC and OPCPA. Our numerical simulations demonstrate that OPMPC supports over 50% amplification efficiency, broad spectral bandwidth, and excellent spatio-temporal pulse quality, making it a promising scheme for high-power ultrafast lasers.

High-power, few-femtosecond laser sources primarily relies on two technologies: chirped pulse amplification with multi-pass cell (MPC) based post-compression [1], and optical parametric chirped pulse amplification (OPCPA) [2]. However, the limitations of the two technologies in terms of spectral tunability, efficiency and spatio-temporal pulse quality can introduce key constraints for applications such as strong-field physics, secondary sources, and many more. To address these challenges, we introduce the optical parametric multi-pass cell (OPMPC) amplifier, combining the benefits of MPC and OPCPA.

We present results from our (3+1) D simulations using the chi3D software [3]. The method uses thin nonlinear crystals in an MPC for parametric amplification. Collinear pump and signal pulses propagate through the MPC, while the idler is filtered out after each pass to prevent back-conversion due to phase mismatch and uneven pump depletion. Fig. 1(a) illustrates the scheme using MPM mirrors reflecting both pump (1.03 µm) and signal (1.6 µm) wavelengths. Four 0.15 mm thick $KNbO_3$ crystals are symmetrically placed near the focus, spaced 25 mm apart. Adjacent crystal pairs have complementary orientations to compensate for spatial walk-off. The pump pulses have a duration of 1 ps with 1 mJ pulse energy. A suitable seed spectrum spanning 1.3 µm to 2.1 µm is utilized. The seed is chirped to optimize the temporal overlap with the pump.

Fig. 1(b) shows the seed spectrum together with the amplified signal spectrum after 20 passes through the MPC. Linear losses occurring at crystal interfaces and mirrors are taken into account, leading to a linear transmission of the multi-pass cell of 80%. Our simulations predict conversion efficiencies exceeding 50% in a key spectral range. The simulated signal saturates at around 50% conversion efficiency due to cell transmission losses, limiting performance below the quantum limit of 64%. The compressed output pulse after second and third order dispersion optimization yields a 20 fs (FWHM) amplified output pulse, close to the ~18 fs Fourier limit, as shown in Fig. 1(d). The inset displays excellent signal beam profile, resulting from the quasi-waveguiding properties of the MPC.

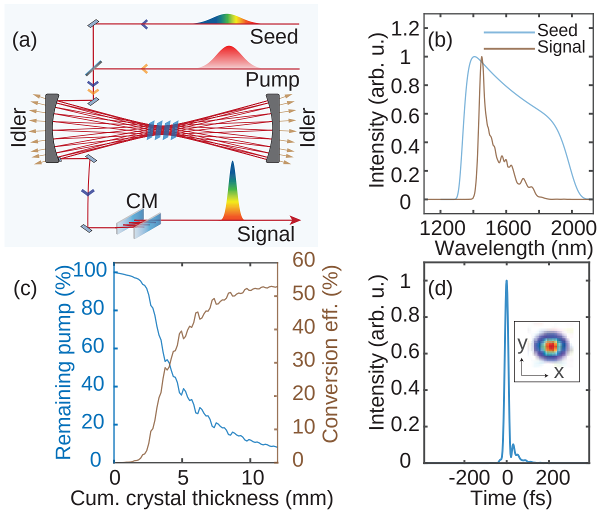

Figure 1: (a) Schematic of the OPMPC with collinearly propagating seed and pump pulses. CM: Chirped mirrors. Simulated (b) input seed and output signal spectra, (c) pump depletion and conversion efficiency, (d) compressed output pulse. Inset: output signal beam profile.

In conclusion, we introduce a novel optical parametric multi-pass scheme integrating nonlinear amplification within an MPC. Numerical simulations taking into account idler suppression after each pass through the MPC reveal excellent efficiency and spatio-temporal pulse quality.

The authors acknowledge funding from BMFTR, under grant 13N16678.

References

[1] A. L. Viotti *et al.*, Optica **9**, 197-216 (2022).

[2] H. Fattahi *et al.*, Optica **1**, 45-63 (2014).

[3] T. Lang *et al.*, Opt. Express **21**, 949-959 (2013).

[4] S. Rajhans *et al.*, manuscript in prep. (2025).

* supriya.rajhans@desy.de

Beam Transport and Beam Shaping System from POLARIS and JETi200 to the new Target Area Fraunhofer (TAF)

M. Hornung*[1,2], A. Sävert[1], T. Köhler[2], M. Zepf[1,2], and M. C. Kaluza[1,2]

[1]HI Jena, Fröbelstieg 3, 07743 Jena, Germany; [2]IOQ, FSU Jena

We present the status of the beam transport system from POLARIS and JETi200 to the new target area Fraunhofer. In particular, we describe the installation and commisioning of the wedding chamber and the progress in manufacturing the beam shaping chamber.

The layout of the beam transport system was described in detail in last year's annual report [1]. It consists of a number of vacuum chambers for beam guiding through the different laboratories. Finally, the JETi200, JETiOne and POLARIS laser pulses are combined in the so-called wedding chamber. From this point onward, the three laser pulses are propagating spatially separated in a DN630 vacuum tube towards the beam shaping chamber. This beam shaping chamber can be used to optimize, modify and focus the laser pulses individually. During the last year we continued the construction and planning of the overall system. With the commissioning of the wedding chamber an the design approval of the beam shaping chamber we achieved two significant milestones. A photo of the wedding chamber is shown in Fig. 1. The wedding chamber with an inner size 0.92 m x 0.80 m x 0.82 m above the 10 cm thick aluminum breadboard has a DN320-flange on the top as the entrance for the JETi200 and JETiOne laser pulses and a DN500-flange on one side as the entrance for the POLARIS laser pulses. Inside the wedding chamber two large aperture mirror mounts will direct all three laser pulses through a DN630-output flange towards the beam shaping chamber.

Figure 1: Wedding chamber on the stability optimized concrete block. For accurate attachment a glued and screwed granite block is used to connect the wedding chamber with the concrete block.

The cutted schematic layout of the beam shaping chamber is displayed in Fig. 2 to show the inner construction. Currently, the chamber is being produced by Pfeiffer Vacuum Components & Solutions GmbH (Germany) and the delivery and construction is planned for Q4/2025. The beam shaping chamber will be mounted onto a 75 cm high block of concrete.

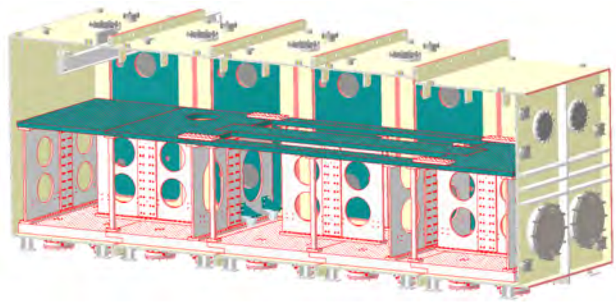

Figure 2: Cutted schematic view of the beam shaping chamber. The outer dimensions are 6.15 m x 1.94 m x 2.25 m and the chamber is separated in 5 segments to ensure the introduction.

One major challange for the beam shaping chamber is the ultra-stable mounting of optical mounts in two different heights at 2.5 m and 1.4 m above ground. To avoid vibrations and movements of the turning mirrors and focusing elements a complex setup is required. In coorparation with the Baudynamik Heiland & Mistler GmbH (Germany) an ultra-stable and flexible shear wall system was developed. The shear wall system is shown in Fig. 2, where the edges are marked in red. It offers two mounting levels. Due to the simulation and optimization of the overall system with respect to the highest eigenfrequencies the required stability for the optic mounts is ensured.

*The authors acknowledge funding from European Union (*EFRE, *2022 FGI 0005).*

References

[1] M. Hornung, HI Jena annual report, p. 19 (2023).

*marco.hornung@uni-jena.de

A Femtosecond Timing System for JETi200, JETi ONE and POLARIS

A. Sävert*[1], M. Hornung[1], and M. Zepf[1,2]

[1]Helmholtz Institute Jena, Fröbelstieg 3, 07743 Jena, Germany; [2]Institut für Optik und Quantenelektronik, Friedrich-Schiller-Universität Jena, Max-Wien-Platz 1, 07743 Jena Germany

Understanding the interaction of a high-intensity laser pulse with matter is a fundamental part of the scientific program at the Helmholtz Institute Jena. The combination of JETi200 and POLARIS in the new Target Area Fraunhofer (TAF) will open the path for a new type of high-intensity experiments.

The two high-power lasers JETi200 and POLARIS have a peak power of more than 200 TW each. This allows pump-probe experiments to be carried out in a new parameter space, e.g. use electron or ion beams as a probe. The transient nature of the observed phenomena also requires an additional optical probe pulse with a duration of a few femtoseconds only over a wide spectral range, from the visible to the short wave infrared, the JETi ONE.

For the experiments to be successful, all three laser systems must be synchronized with each other. The temporal jitter should be below 20 fs (rms) to ensure a reliable temporal overlap. Cycle GmbH provided the timing system to synchronize all three laser systems. The main component is a temperature-stabilized platform for the low noise optical master oscillator (OMO) running at 1550 nm, see Fig. 1.

Figure 1: Installaton of the Pulsed Timing System in the POLARIS lab

The pulses are split into four channels each equipped with an out-of-loop delay line to select the relative delay between the timing links and hence to the synchronized oscillators. The timing links have a length of 80 m and are distributed from the POLARIS lab to JETi200 lab and TAF. The synchronization between the timing link and the oscillators is based on Two-Colored Balanced Optical Cross-Correlators (2x 1550 nm/800 nm and 1550 nm/1030 nm) [1]. Depending on the noise level of the used oscillator a synchronization with a jitter below 5 fs was

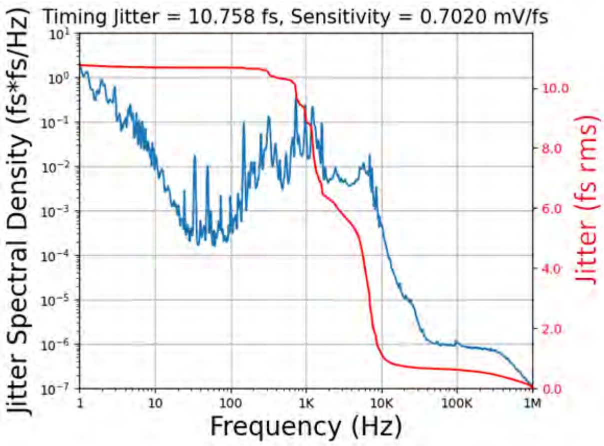

Figure 2: Temporal integrated jitter measurement between the Element 2 and Flint oscillator.

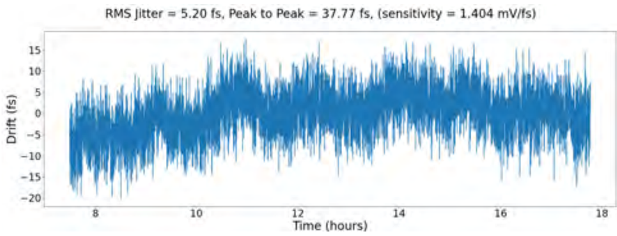

Figure 3: Long-term temporal integrated jitter measurement between the Element 2 and Flint oscillator.

achieved. Furthermore the temporal delay jitter between the new JETi200 oscillator (spectra physics Element 2) and the new POLARIS oscillator (light conversion Flint) have been measured in the frequency range between 1 Hz and 1 MHz to 11 fs (rms), see Fig. 2. The long-term drift over 10 hours was measured to 5 fs (rms), see Fig. 3.

The next step is to put the oscillators at their designated position at the beginning of each laser system.

The authors acknowledge funding from Thüringer Ministerium für Bildung, Wissenschaft und Kultur (2023 FGI 0022) and the Europäischen Fonds für regionale Entwicklung (EFRE).

References

[1] K.Safak *et al.*, Scientific Reports **8**, 11948 (2018).

* a.saevert@hi-jena.gsi.de

Reinforcement Learning Methods for Laser Amplifier Alignment

Matthew B. Schwab*[1,2] and Malte C. Kaluza[1,2]

[1]Helmholtz-Institute Jena, Jena, Germany; [2]IOQ, Friedrich-Schiller University, Jena, Germany

Laser Plasma Accelerators (LPAs) demand stable laser operation due to the non-linearity of various acceleration mechanisms, e.g., LWFA, TNSA, etc. Reinforcement Learning (RL), using the model-free Proximal Policy Optimization (PPO) algorithm, is tested as a control technique for alignment of the POLARIS laser's regenerative amplifiers using existing laser diagnostics. Control of two input mirrors into a regenerative amplifier was given to the trained RL agent. The stationary task of realigning to known references is performed in $\sim$ 5 laser shots, while the non-stationary task of finding a new optimal alignment is still being refined. Sequential and simultaneous control of the input alignment and the amplifier's cavity alignment is also the subject of ongoing tests. Similar work on automated laser alignment using RL can be found in [1].

The PPO algorithm [2] was introduced in 2017 as a successor to a more computationally intensive algorithm (TRPO [3]) and has seen wide success in a diverse range of applications. Like most RL algorithms, it is fundamentally based on the Markov Decision Process (MDP) framework used in learning optimal policies for sequential decision making. The goal of such a policy, which in modern RL is encoded into the weights and biases of a neural network (NN), is to maximize the expected sum of rewards collected by the agent depending on how it interacts with its environment. Observations (see Fig. 1) of the environment are given to the agent's NN which produces actions to be performed on the environment. The change in the environment's state is used to determine the reward signal.

In the work described here, observations include the laser beam's position on CCD sensors that monitor the amplifier chain, as well as the output laser energy from the amplifier. Actions are limited to the motion of stepper motors that control the orientation of laser mirrors in the amplifier chain. Training an agent to learn an optimal control policy requires, for "vanilla"-RL algorithms, millions of iterations with the system. Given the 1 Hz repetition rate of the amplifier, training an agent must be performed in simulation, meaning a simulation of the amplifier system must be available. Furthermore, the so-called "Sim2Real"-gap must be investigated. In short, this gap consists of all the hardware defects, noise sources and other biases that the simulation might not contain, which prevents the control policy, learned in simulation, from being optimal in the hardware environment.

Two methods of simulating the input mirror system were developed. The first implemented ray tracing using the measured geometry of the mirrors and detectors in the laboratory. The second method was based on a linear algebra

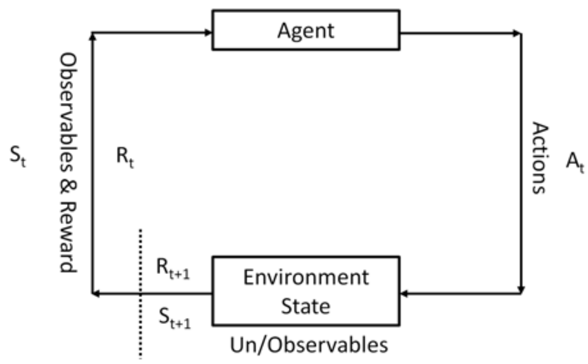

Figure 1: Typical reinforcement learning scenario.

model that was calibrated using laboratory measurements. Both methods exhibit advantages and disadvantages, and both are suitable for use in training an agent in simulation.

Other important factors in this work have been the calibration and modelling of backlash and the improvement of our beam diagnostics to resolve motion of the laser beam. Motor backlash, if improperly simulated, prevents the agent from learning the real result of driving the stepper motors in a back-and-forth fashion, which can be necessary for fine-tuning the laser alignment. The resolution of our beam position diagnostics also needed improvement, so that single motor steps are resolved at the CCD sensors.

Finally, two general alignment cases have been identified. In the stationary case, the laser beam is aligned to known references, defined as beam positions on the CCD sensors. In the non-stationary case, the amplifier's optimal energy no longer coincides with the CCD references. This forces the PPO agent to search in the vicinity of the previous CCD reference for the new optimal laser alignment.

The current status of the project is as follows. In the stationary case, trained PPO agents can realign the laser beam to known CCD references to sub-pixel accuracy in 5 laser shots. This performance exceeds that of most, if not all, human operators, especially when the laser mirrors cannot simultaneously be controlled by a single human. Development and testing of the non-stationary case are ongoing.

References

[1] N. Bruchon *et al.*, Electronics **9**, 781 (2020).

[2] J. Schulman *et al.*, arXiv:1707.06347v2[cs.LG].

[3] J. Schulman *et al.*, arXiv:1502.05477v5[cs.LG].

*matthew.schwab@uni-jena.de

Recovering Beamline Optics – A Plasma Downstream Asher for HI Jena

S. Kiesel*[1], G. Schäfer[1], Alexander Sävert[1], and Matt Zepf[1,3]

[1]HI Jena, Fröbelstieg 3, 07743 Jena, Germany; [2]Friedrich-Schiller-Universität Jena, 07743 Jena, Germany

Helmholtz Institute Jena has acquired a plasma downstream asher, dedicated to removing unwanted accumulated carbonaceous layers from JETi200 compressor gratings and beamline optics. A test chamber for evaluation of the device was built and first tests were performed. The downstream asher is readily installed and easy to use.

At the JETi200 laser system large scale optics, such as mirrors, gratings, or parabolic mirrors in vacuum beamline and pulse compressor are exposed to high intensity laser pulses, UV, or ionizing readiation. While these optical elements are kept under vacuum conditions, residuals of carbohydrates evaporate from contamination sources and reach optical surfaces, eventually. Exposure to high intensity laser pulses, or other mentioned types of radiation, leads to cracking of residing carbohydrates. Volatile compounds, as well as solid carbonaceous deposits [1] are produced. Progressive build-up of these carbonaceous layers gradually decreases reflectivity and efficiency of mentioned optical elements. As a result, laser beam intensity decreases over time, eventually prompting the need for replacement of optical elements. Considering, more than fifteen turning mirrors are installed in the JETi200 laser beam line, just minor changes to their reflectivity result in a huge drop in total transmission efficiency.

Cleaning approaches pose viable alternatives to replacement strategies, including ozone cleaning [2], laser cleaning [3], and plasma cleaning [1]. Most of these methods still require mirrors to be unmounted, entailing an effortful procedure of realignment. However, downstream plasma cleaning stands out, owing to its simple setup and in-situ application procedure to the installed optical element.

A plasma downstream cleaner houses a radio frequency plasma source, generating a plasma with oxygen radicals as active cleaning species. Emitted oxygen radicals reach carbonaceous deposits and subsequently transform solid deposits into volatile compounds, e.g. CO_2, that are readily pumped out.

In order to profit from such cleaning prospects High Intensity Laser Physics working group of Helmholtz Institute Jena has acquired a GV10x downstream asher from ibss in 2024. After ten years of successful operation, JETi200 Laser still employs most of the original beamline mirrors and optical gratings. While not begin damaged, their efficiency has decreased. By employment of the asher we aim to mitigate the exchange of contaminated optics, and save time and costs for the benefit of pursuing scientific goals.

In our evaluation phase we have constructed a simple test chamber, shown in Fig. 1 (a), to gain operation experience, try different cleaning recipies, and to prevent damaging critical parts due to possible improper operation. Our tests were carried out on several beamline mirrors and used gratings, showing dark imprints of the laser profile. Results are shown in Fig. 1. Before cleaning the mirror exhibits a black central spot (Fig. 1 (b)), that is completely removed (Fig. 1 (c)) after cleaning over five hours at a chamber pressure in the high 10^{-4} mbar range. Similar results were achieved with a gold coated grating and a silver coated parabolic mirror.

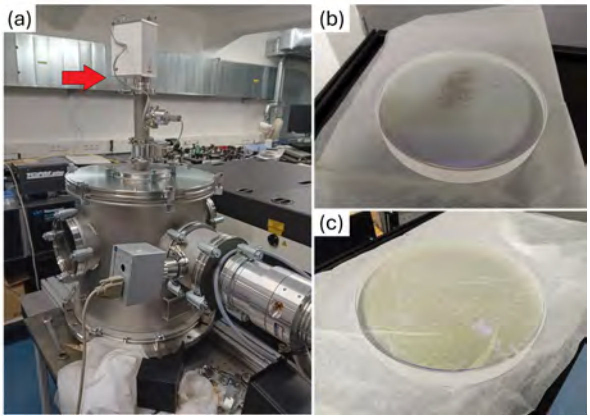

Figure 1: (a) Plasma cleaner test setup in the JETi200 lab. Downstream asher is indicated by a red arrow. Cleaning results are illustrated featuring a beamline mirror (b) before and (c) after cleaning.

One of the main goals was cleaning parts over the course of a few hours, while keeping the turbomolecular pump running. Since cleaning efficiencies wane with decreasing pressure, operating the pumps prolongs cleaning durations. However, in a live setup we refrain from turning off the pumps to reach much faster re-establishment of desired operation pressures after switching off the plasma cleaner. Such technique enables cleaning of optics over night without affecting experimental beam time schedules.

So far, our qualitative analysis shows huge improvements and a complete removal of dark imprints on tested optics. In a next step, we aim for quantifying these results by mounting the device at the JETi200 compressor chamber to clean the installed gratings. Further, we have planned cleaning several turning mirrors in-situ along the beam line.

References

[1] Z. Hubka *et al.*, Applied Optics **60**, 533–538 (2021)

[2] N. Bartels *et al.*, Proc. SPIE **11173**, 9–107 (2019)

[3] Y. Zhou *et al.*, Journal of Nuclear Materials **415**, S1206–S1209 (2011)

*s.kiesel@hi-jena.gsi.de

LASER PLASMA ACCELERATION

Observation of Coherent Emission from Relativistic Solitons

Y. Zhao*[1,2], X. Huang[1], D. Seipt[1,2], A. Sävert[1,2], and M. C. Kaluza[1,2]

[1]HI Jena, Fröbelstieg 3, 07743 Jena, Germany; [2]IOQ, FSU Jena

Instabilities are inevitable when high-power laser pulses interact with plasmas due to their highly nonlinear nature. In this study, we observed an undocumented coherent light-emitting structure following a high-power laser pulse in underdense plasma. The observation was done using our newly developed few-cycle burst-shot microscopy diagnostic. The results show that the structure is stationary, has micrometer-sized dimension, a broad spectral bandwidth, and a long lifetime. These distinct features strongly correlate the observed structure with previous simulation studies of relativistic solitons. Observing relativistic solitons substantially contributes to our understanding of laser-plasma instabilities and the fundamentals of plasma turbulence.

Interactions of high-power laser pulses with plasmas have been extensively studied over the past decades. In this study, we report the observation of an undocumented coherent light-emitting structure in the wake of high-power laser pulses propagating through underdense plasmas. Our experiment used a novel ultrafast burst-shot microscopic imaging system based on few-cycle microscopy. A few-cycle probe pulse (Fourier transform limited pulse duration $\tau_{\mathrm{FWHM}} = 8\,\mathrm{fs}$) was linearly chirped (GDD $= 434\,\mathrm{fs}^2$), and then back-illuminated the wakefield, which was imaged by a microscopic system. Three non-polarizing beamsplitters were placed after the tube lens to create four replicas of the probe. These replicas were individually imaged by cameras equipped different narrow bandpass filters with center wavelengths at $850\,\mathrm{nm}$, $800\,\mathrm{nm}$, $750\,\mathrm{nm}$ and $700\,\mathrm{nm}$, and a bandwidth of $\Delta\lambda = 10\,\mathrm{nm}$. One set of the four images taken during one single laser shot is shown in Fig. 1.

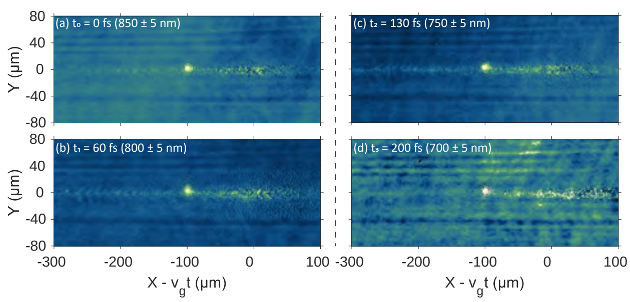

Figure 1: A relativistic soliton in the wake of a high-power laser pulse. The numbers on the upper-left corner denote the delay relative to the first frame and the corresponding wavelengths of each frame.

Fig. 1 shows a small bright emission spot ($< 5\,\mu\mathrm{m}$) with interference rings around its center, indicating coherence of the soliton emission and the probe pulse. The emission with interference rings was observed in all four frames across varying wavelengths, suggesting that the emission has a broad spectral bandwidth. Moreover, due to the linear chirping of the probe pulse, different wavelengths are transmitted through the interaction point at varying time delays $\approx 200\,\mathrm{fs}$ between the first and last frames. This indicates that the lifetime of the emission exceeds this duration. Nevertheless, no movement of the soliton was observed on this time scale. These findings demonstrate a good agreement with previous PIC simulations [1], as evidenced by the following characteristics: coherence, broad bandwidth, long-lifetime, and stationarity. PIC simulations for our experimental parameters are ongoing.

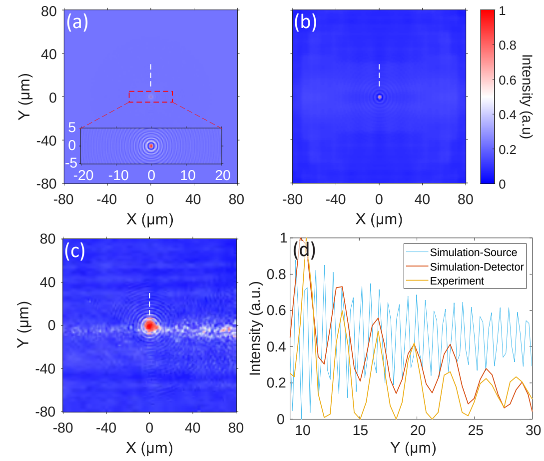

Figure 2: Comparison of the simulated (a,b) and experimentally observed (c) interference at $800\,\mathrm{nm}$ wavelength. Panel (b) shows the optical field on the source plane (a) imaged by an ideal image system onto a detector. (d) Comparison of the interference period. The intensity was extracted along the white dashed line on (a), (b) and (c), and normalized.

We hypothesized that the emission has the form of a spherical wave due to its μm source size. An optical field simulation was conducted to verify this hypothesis, and the results are shown in Fig. 2. In Fig. 2(a), the interference between a spherical wave and a plane wave at $800\,\mathrm{nm}$ wavelength was observed $0.8\,\mu\mathrm{m}$ after the point source of the spherical wave and the spatial period is $\approx 0.8\,\mu\mathrm{m}$. The optical field in this plane was imaged by an ideal imaging system with a numerical aperture of 0.26 and the intensity is presented in Fig. 2(b), with a spatial period of the $3.2\,\mu\mathrm{m}$, matching well with the experimental observation. A comparison of the simulation and experimenal lineouts is given in Fig. 2(d).

* yu.zhao@uni-jena.de

References

[1] T. Esirkepov *et al.*, Phys. Rev. Lett. **92**, 255001 (2004).

Accelerating Electron Beams Using D-Shaped and Ring-Shaped Near-Field Laser Beams

F. C. Salgado *[1,2,3], A. Kozan[1,2,3], K. Grafenstein[4], S. Karsch[4], and M. Zepf[1,2,3]

[1] *HI Jena, Fröbelstieg 3, 07743 Jena, Germany;* [2] *GSI Helmholtzzentrum für Schwerionenforschung, Planckstraße 1, 64291 Darmstadt, Germany;* [3] *IOQ, Friedrich-Schiller-Universität Jena, Germany;* [4] *Ludwig-Maximilians-Universität München, Germany*

Ultra-intense lasers and GeV electron beams from plasma accelerators offer a promising way to explore strong-field QED effects experimentally. The FOR2783 pair-production experiment at CALA [2] will test the nonlinear Breit-Wheeler process [1] using an all-optical setup, expecting about 80 pairs per hour [2]. A key challenge is the generation of 10 pC electron beams at around 2.5 GeV with the necessary splitting of the ATLAS 3000 laser into LWFA and collider beams. Here, we present a preliminary analysis of laser-accelerated electron beam performance using different near-field laser configurations for the experiment.

At the FOR2783 nonlinear Breit-Wheeler experiment, the ATLAS-3000 laser will be split into two beams: a laser beam of approximately 9.5 J with a root mean square (RMS) diameter of about 12 cm, referred to as the collider laser, and the remaining laser beam, known as the LWFA beam, with energy above 25 J, which will be used to accelerate electron beams up to 2.5 GeV to generate bremsstrahlung γ-photons that will interact with the collider laser beam.

Two possibilities have been considered for splitting the full 28 cm RMS diameter of the ATLAS-3000 into the both laser beams: a D-shaped or a ring-shaped split. However, the performance of the electron accelerator using the structured NF of the LWFA beam after the split still needs to be assessed to help determine which of the two settings offer superior performance.

To this end, we conducted an experimental campaign at the JETi-200 laser system at the Helmholtz Institute Jena to determine the optimal laser beam splitting for the pair-production experiment at CALA. The JETi-200 beam, with a 12 cm RMS diameter and 25 fs pulse duration, was focused by an F/20 off-axis parabolic mirror into a 5 mm gas cell filled with 95% He and 5% N_2, creating an underdense plasma with electron density of $\approx 2\times10^{18}\mathrm{cm}^{-3}$. The laser energy of the full beam before splitting was (1.7 ± 0.1) J. The intensity on target, characterized by normalized vector potential a_0, was varied either by reducing the full, unsplit beam energy (Figure 1a) or by adjusting the splitting ratios of D-shaped and ring-shaped beams (Figures 1b and c).

The energy spectrum and charge of the accelerated electron beams were measured using scintillating LANEX screens. Figure 1d) presents a comparison of the measured beam charge across different beam-splitting configurations and a_0 values, with all other parameters held constant. Preliminary results indicate that the D-shaped near-field performs similarly to the full, unsplit beam at reduced energy, while the ring-shaped configuration yields roughly half the charge.

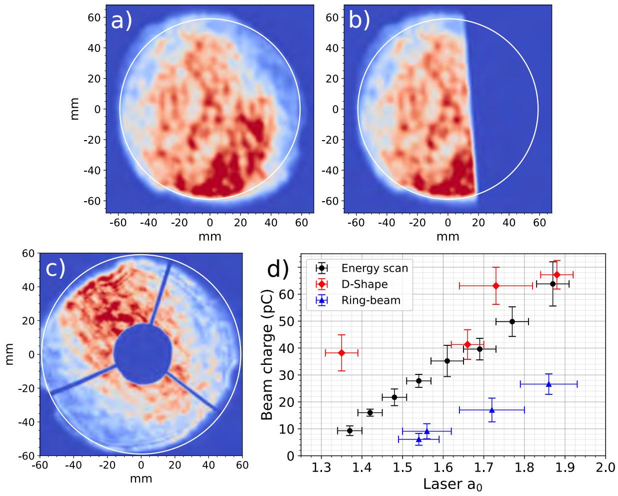

Figure 1: Examples of near-field laser beam configurations used in the JETi-200 experiment are shown in Figure 1: a) full beam without blocking, b) D-shaped with 31% blocked, and c) ring-shaped with 26% blocked. The electron beam charges compared in d) show the D-shaped performing similarly to the full beam, while the ring-shaped yields about half the charge.

Based on the results in Figure 1, the D-shaped split is as a promising option for generating stable electron beams, showing performance comparable to the full near-field laser beam without energy reduction in terms of beam charge. However, further investigation of the electron energy spectrum peak, along with tests at the ATLAS-3000 laser system, is still required to determine the most suitable splitting configuration for the final FOR2783 pair-production experiment at CALA. Simulations are also being conducted to support the experimental observations.

F.C.S. and M.Z. thank the funding by the Deutsche Forschungsgemeinschaft (DFG) under Project No. 416708866 within the Research Unit FOR2783.

References

[1] V. I. Ritus, J. Sov. Laser Res. **6**, 5 (1985).

[2] F. C. Salgado *et al.*, New J. Phys. **23**, 105002 (2021).

* felipe.salgado@uni-jena.de

Damage Threshold Tests for Project FOR2783

A. Kozan*[1,2], F. Salgado[1,2], A. Sävert[1,2], G. Schäfer[1,2], and M. Zepf[1,2]

[1]HI Jena, Fröbelstieg 3, 07743 Jena, Germany; [2]IOQ, FSU Jena

The Breit-Wheeler pair production experiment, under project FOR2783 [1], requires laser operation near the damage threshold of the turning mirror. Due to the experiment's inherently low cross section, a high number of laser shots is essential. Consequently, the selection of the mirrors and the geometry must be optimized to maximize shot count without exceeding damage limits. To support this, a laser-induced damage threshold (LIDT) test was performed using the JETi200 laser system on candidate mirrors intended for use in the final setup.

To test the candidate mirrors, a scaled-down version of the setup in Center for Advanced Laser Applications (CALA) was built in JETi200 laser lab. The candidate mirrors were installed after the laser was focused with an off-axis parabola (OAP), with an incidence angle of 8 degrees and s-polarization relative to the laser beam. The mirrors were located before the focal plane of the OAP, resulting with a laser spotsize of 5 mm on the mirror. The reflected laser from the mirror blocked with a ceramic screen which was imaged by a CCD camera resulting in Fig 1. Additionally, another camera was used to image the mirror undergoing the LIDT test, in order to capture scattered light resulting from damage.

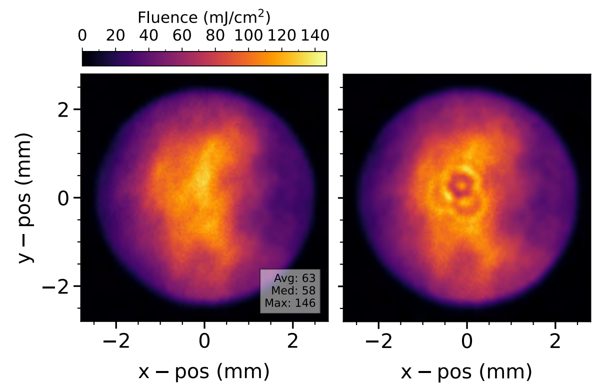

Figure 1: Left: Beam Near-Field profile on the ceramic screen with an average fluence of 63 mJ/cm². Right: Beam profile with an average fluence of 72 mJ/cm² which resulted with damages at the high fluence center. Both figures scaled to match the beam size on the mirror.

The ramp-up test procedure [2] was employed to determine the LIDT. The laser profile used in the experiment is shown on the left in Fig.1, where the average fluence is 63 mJ/cm²—below the LIDT—while the peak fluence reaches 146 mJ/cm², yielding a Max/Avg ratio of 2.3. The right side of Fig.1 shows visible damage formed in the high-fluence regions of the beam profile. In this configuration, an average fluence of 72 mJ/cm² was computed which corresponds to 166 mJ/cm² peak fluence, defined as LIDT level.

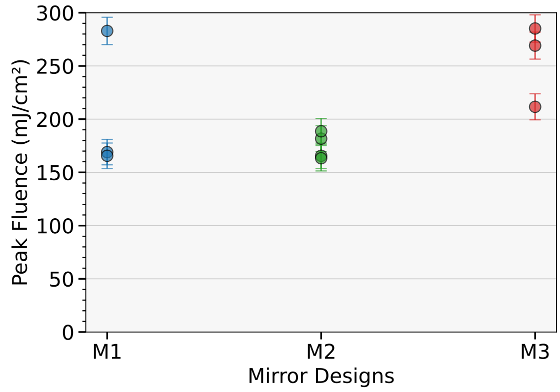

Figure 2: Ramp-up damage threshold test results for three different mirror designs (M1-M3). Peak fluence obtained multiplying average fluence with Max/Avg ratio. Mirrors M1 coated using magnetron sputtering, M2 coated using ion beam sputtering, and M3 coated using thermal evaporation. Each datapoint indicates a test run with different sample. Error bars are systematic error (ramp-up steps) and laser energy jitter.

The results of the ramp-up test for three different mirror designs (M1–M3) are shown in Fig.2. The averaged peak LIDT values of different test runs were measured to be 205 mJ/cm² for M1, 175 mJ/cm² for M2, and 255 mJ/cm² for M3. Despite these differences, overall performance range suggests that there is no significant variation between mirrors. Notably, all mirrors withstood high-repetition rate testing at fluence levels 15% below their respective LIDT limits, with no observed damage after 15 minutes of laser shots at 5 Hz.

To conclude, with slight differences of peak LIDT, all mirrors performed similarly. Each remained stable during high-repetition rate testing at 15% below their measured LIDT. For accurate LIDT assessment and further experimental considerations, the Max/Avg fluence ratio in CALA should be taken into account, as damage is primarily driven by peak fluence.

F.C.S. and M.Z. thank the funding by the Deutsche Forschungsgemeinschaft (DFG) under Project No. 416708866 within the Research Unit FOR2783.

References

[1] F. C. Salgado *et al.*, New J. Phys. **23**, 105002 (2021).

[2] D. Ristau, Laser-Induced Damage in Optical Materials, CRC Press (2014).

*a.kozan@hi-jena.gsi.de

Decoding the electron bunch duration via passive plasma lensing

A. Seidel*[1,2], C. Zepter[1,2], A. Sävert[1,2], S. Kuschel[3], and M. Zepf[1,2]

[1]IOQ, Max-Wien-Platz 1, 07743 Jena, Germany; [2]HI Jena, Fröbelstieg 3, 07743 Jena, Germany; [3]TU Darmstadt, Karolinenplatz 5, 64289 Darmstadt, Germany

We report on experimental results demonstrating the passive plasma lensing effect for a broadband electron bunch typical for laser wakefield acceleration (LWFA). Furthermore, by utilizing linear plasma wakefield theory, we demonstrate that the length of the electron bunch can be derived from the focused energy spectrum.

Laser wakefield acceleration (LWFA) has emerged as a promising technique for producing ultra-short ($\sigma_z \approx 1\,\mu\text{m}$), high-energy ($E >$ GeV), high-charge (nC) electron bunches with normalized emittances $\epsilon_n < 1\,\mu\text{m}$, making them ideal candidates for seeding free-electron lasers or synchrotrons. However, while advances have been made in the quality of electron bunches, small and accessible measuring techniques for ultra-short bunches($< 1\,\mu\text{m}$) have not yet been developed.

We present a technique for measuring the length of ultra-short and high-energy electron bunches.

When an electron bunch propagates through a plasma of similar density, it creates a co-moving density perturbation known as a wakefield. The wakefield, along with the electromagnetic fields acting on the electron bunch, will be weaker at the front than at the rear of the bunch. The transverse wakefields in this configuration will increase linearly with the distance from the axis and will therefore act on the electron bunch like a lens [1].

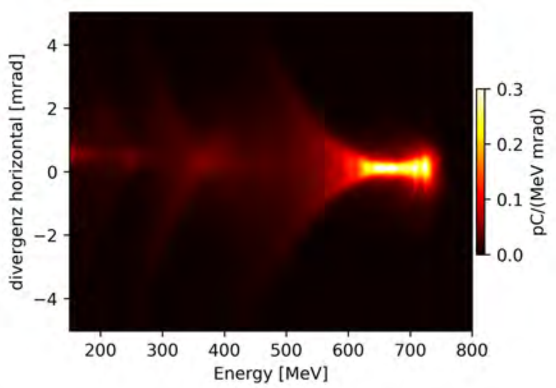

Figure 1: Electron energy spectrum after passing through a plasma lens.

With the smaller wakefields at the front of the bunch, it will experience a reduced focusing strength compared to the rear part. If the electron bunch is chirped, as it is the case for LWFA electron bunches, the varying focusing strength will be evident on a dispersing spectrometer, as

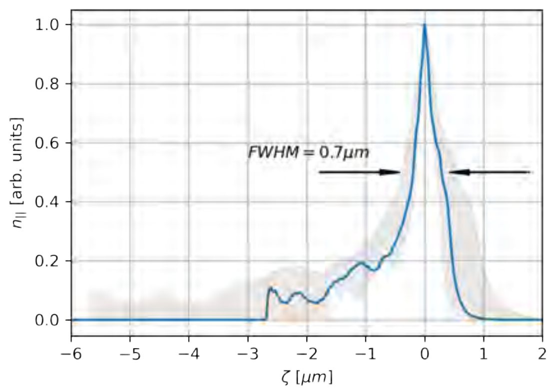

Figure 2: Longitudinal electron density profile (blue) with the corresponding uncertainty of the fitting algorithm shown in grey.

shown in Figure 1. Here, we present data on an electron bunch accelerated by focusing the JETi 200 laser ($E = 4$J,$\tau = 23$fs and $a_0 = 3$) onto a gas cell developed at the Helmholtz Institute in Jena. The cell was filled with a mixture of 92 % helium and 8 % nitrogen, which enabled the laser beam to be guided over an acceleration length of 7 mm while simultaneously providing maximum charge injection into the bunch through ionization injection. A 7 mm long gas jet filled with pure helium was utilized as the plasma lens. The electron bunch's initial rms divergence is 0.6 mrad across the entire energy range, and it is strongly modulated in the plasma lens as presented in Figure 1. With precise knowledge of the setup, the charge of the electron bunch, and the density of the gas jet, it is possible to deduce the length of the electron bunch from the number of modulations; a lower amount indicates a shorter bunch, while a higher amount implies a longer bunch.

To analyze the length of the electron bunch, we developed an algorithm combining linear wakefield theory [2] and electron beam optics. Our findings, illustrated in Figure 2, reveal a full bunch length of $\approx 4\,\mu\text{m}$, consistent with prior LWFA measurements [3]. Particle-in-cell (PIC) simulations further suggest that this method can measure electron bunch lengths down to sub-μm scales, underscoring its potential as a robust diagnostic tool for advanced accelerator research.

References

[1] S. Kuschel *et al.*, Phys. Rev. Accel. Beams **19**, 71301 (2016).

[2] R. Keinigs *et al.*, The Physics of Fluids **30**, 252 (1987).

[3] O. Zarini *et al.*, Phys. Rev. Accel. Beams **25**, 12801 (2022).

* seidel.andreas@uni-jena.de

Towards Stopping Power Experiments with LIGHT

H. Nazary*[1], M. Metternich[1], M. Fischer[2], K. Lerner[2], D. Schumacher[1], F. Neufeld[2], S. J. Grimm[2], C. Brabetz[1], F. Kroll[3,4], J. Schilz[3,4], M. Dehmer[5], A. Blažević[1,6], S. Kuschel[2], U. Schramm[3,4], V. Bagnoud[1,2,6], and M. Roth[2]

[1] *GSI, Darmstadt, Germany;* [2] *TU Darmstadt, Darmstadt, Germany;* [3] *HZDR, Dresden, Germany;* [4] *TUD Dresden, Dresden, Germany;* [5] *Goethe Universität Frankfurt, Frankfurt am Main, Germany ;* [6] *HI Jena, Jena, Germany*

Theoretical models for ion stopping in plasma disagree, especially when ion velocity approaches the plasma's thermal electron velocity. Experiments with the laser driven LIGHT beamline at GSI investigate this critical regime. Preparatory beam times with protons and carbon ions confirmed the setup's capability, delivering very intense and short ion bunches for study. Stopping power measurements in cold foils were successfully demonstrated, validating the approach.

The stopping power of ions in plasma is important in inertial confinement fusion, where alpha particle self-heating must overcome all loss processes. Many theories exist for the energy loss of ions in plasma, but there are discrepancies in the region where the projectile velocity is close to the thermal plasma electron velocity. This region is investigated in stopping power experiments with the Laser Ion Generation, Handling, and Transport (LIGHT) beamline. The setup is shown in Figure 1. Projectile ions are generated and accelerated via the TNSA mechanism using the PHELIX laser in the Z6 target chamber at GSI. The initial TNSA beam is divergent and has an exponentially decaying energy spectrum. A pulsed high-field solenoid magnet captures the ions, selects one energy, and collimates it. Afterwards, an RF cavity temporally compresses the ion bunch by decelerating the fast ions in the front and accelerating the slow ions in the back, such that the ions in the back catch up to the ions in the front generating ion bunches shorter than 1 ns. A second solenoid focuses the ion beam onto a plasma generated by the nhelix laser in the Z4 target chamber at GSI. After probing the plasma, a diamond detector measures the energy of the ions via time of flight.

*h.nazary@gsi.de

Table 1: Measured parameters of the temporally compressed proton and carbon ion bunch.

parameter	proton bunch	carbon ion bunch
mean energy	0.63(1) MeV	7.2(2) MeV
bunch width	0.76(4) ns	1.23(4) ns
focal spot radius	2.82(3) mm	4.11(2) mm
number of ions	$5.9(4) \times 10^8$	$2.0(6) \times 10^8$

Preparatory beam times have been conducted to demonstrate the capacity of the LIGHT beamline to generate the required ion beam, thereby confirming the experiment's feasibility. The beam times were conducted using carbon ions (C^{4+}) and protons. The resulting ion beam parameters are enumerated in Table 1. Furthermore, the measurement of the stopping power in cold foils during these preparatory beam times was demonstrated. The results of this study have been published in [1]. The stopping power measurements in plasma are planned for 2025 and 2026.

References

[1] H. Nazary *et al.*, J. Plasma Phys. **90**, 905900302 (2024).

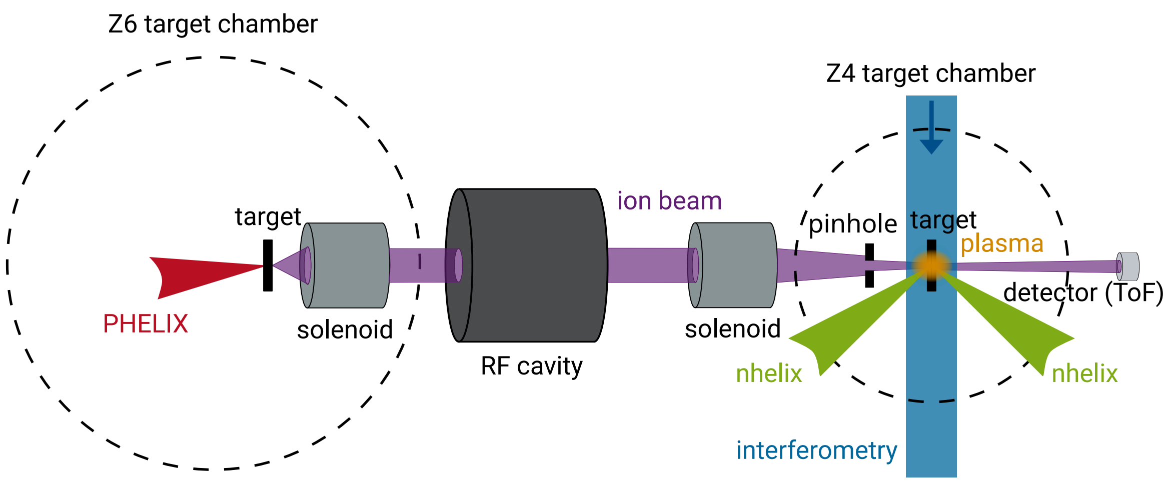

Figure 1: Schematic illustration of the planned stopping power experiment with the LIGHT beamline at the Z6 experimental area of GSI.

Simulations of plasma and magnetic field evolution under relativistic laser nanowire interactions

E. Eftekhari-Zadeh *[1,2], M. Gyrdymov[3,4], P. Tavana[1,3,4], R. Loetzsch[1,2], I. Uschmann[1,2], T. Siefke[5], T. Käsebier[5], U. Zeitner[5], A. Szeghalmi[5], D. Serebryakov[6], E. Nerush[6], I. Kostyukov[6], O. Rosmej[3,4], D. Kartashov[1], and C. Spielmann[1,2]

[1]*IOQ, Friedrich Schiller University Jena;* [2]*HI Jena, Fröbelstieg 3, 07743 Jena;* [3]*GSI, Planckstr. 1, Darmstadt, Germany;* [4]*IAP, Goethe University Frankfurt am Main;* [5]*IAP, Friedrich Schiller University Jena;* [6]*IAP RAS, Nizhny Novgorod, Russia*

Our recent experiments revealed nanosecond-long "jets" of hot, dense plasma formed by high-contrast, relativistically intense laser pulses interacting with nanowire arrays [1]. 3D Particle-in-Cell (PIC) simulations were conducted to study early plasma conditions and electromagnetic fields. Unlike flat targets, nanowire arrays generate kTesla-scale magnetic fields, which likely drive jet formation. Simulated X-ray emission from He-like Ti ions provided estimates of plasma density and temperature within these long-lived jets.

Jet-like plasma structures emitting He-like Ti ion radiation were observed on nanosecond timescales when nanowire arrays of 100 nm Ti core, 25 nm Si cladding, and 400 nm spacing on a 50 µm Si membrane were irradiated with ultra-high contrast, relativistically intense ($\geq 3 \times 10^{19}\,\mathrm{W/cm^2}$) femtosecond laser pulses [1].
The X-ray spectroscopy results measured in the experiments were modeled using the FLYCHK kinetic atomic code to simulate the X-ray emission spectra. We used the steady state model as well as time-dependent transient calculations, based on the plasma density and temperature history retrieved form our PIC simulations, to reproduce the He-like emission spectrum of Ti^{20+} ions. Both approaches suggest that during the interaction with the laser pulse the plasma reaches solid density ($n_e \sim 10^{24}\,\mathrm{cm^{-3}}$) and hot temperature ($>$ 1 keV), whereas in the "jet" at nanosecond time scale the density and the temperature remain on the level $> 10^{21}\,\mathrm{cm^{-3}}$ and $>$ 0.5 keV. The 3D PIC simulations were carried out by the QUILL 3D QED PIC code using $\delta x = \delta y = \delta z = 0.21\,\lambda$ spatial grid and $\delta t = 5 \times 10^{-3}\,\lambda/c$ temporal resolution. The target comprised 25 Ti-coated nanowires (each of diameter $0.375\,\lambda$ and spaced by $1\,\lambda$), on a substrate, with an electron density of $n_e = 30\,n_{\mathrm{cr}}$. Results (see Figure 1) revealed strong contrast between nanowire and flat targets. Nanowire arrays generated a global magnetic field permeating the plasma, in contrast to the surface-localized field in flat targets. The vertically aligned nanowires facilitated the generation of intense forward electron currents, which in turn induced return currents to maintain quasi-neutrality. This interplay produced strong azimuthal quasistatic magnetic fields and an inward-directed $\vec{J} \times \vec{B}$ pinch force, leading to the confinement and heating of the plasma. The simulations validated the emergence of kiloTesla-level magnetic fields,

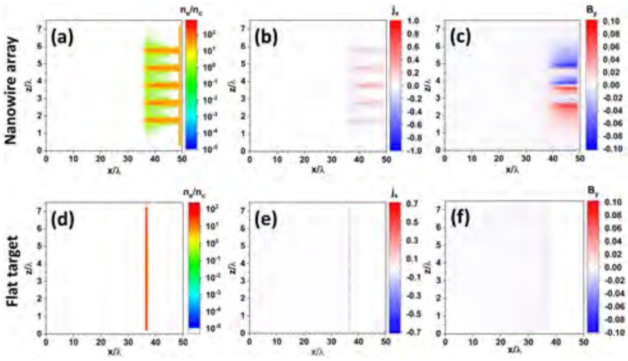

Figure 1: PIC simulations of electron density n_e (in n_{cr}), return current j_x (MA/µm^2), and magnetic feld B_y (GG) for nanowire (a–c) and flat targets (d–f) shortly after laser interaction. Laser propagates left to right.

consistent with analytical estimates and prior studies.
However, the connection between the short time scale plasma evolution after the interaction with the laser pulse and the long (nanoseconds) time scale evolution in the "jets" requires a hybrid PIC - fluid dynamic code that is not currently available. Therefore the question how the giant magnetic field generated in the plasma nanowires on the picosecond time scale influence the subsequent long time plasma evolution is the subject of further investigations.
We propose two possible mechanisms for the formation of plasma "jets" observed in experiments: (1) magnetic-field-driven evolution leading to strongly enhanced Weibel-like instabilities, potentially sustaining hundreds of Tesla magnetic fields over nanosecond time-scale [2], sufficient to confine hot and dense plasma with the parameters estimated from FLYCHK simulations, and (2) collisions of lateral shock waves between adjacent magnetized nanowires, producing longitudinal ejection of dense plasma plasmoids [3].

References

[1] E. Eftekhari-Zadeh *et al.*, Compact EUV & X-ray Light Sources, Optica Publishing Group, JTh6A.1 (2022).

[2] A. N. Stepanov *et al.*, 2020 International Conference Laser Optics (ICLO), IEEE (2020).

[3] S. Takeuchi, Physics of Plasmas **25**, 022111 (2018).

* e.eftekharizadeh@uni-jena.de

PHOTON AND PARTICLE SPECTROSCOPY

A new laser laboratory and progress towards quantum logic spectroscopy with highly-charged heavy ions

H. Hayakawa[1,3], N. Homburg[1,3], L. Kau[1,3], and P. Micke*[1,2,3]

[1] *Helmholtz Institute (HI) Jena, Fröbelstieg 3, 07743 Jena, Germany;* [2] *Institute of Optics and Quantum Electronics, FSU Jena, Max-Wien-Platz 1, 07743 Jena, Germany;* [3] *GSI Helmholtz Center for Heavy Ion Research, Planckstraße 1, 64291 Darmstadt, Germany*

Highly-charged heavy ions offer excellent properties for fundamental physics research. We are developing a new optical clock experiment for this purpose, based on quantum logic spectroscopy in a cryogenic Paul trap and being set up downstream of the HITRAP decelerator. The combination of this universal and highly accurate spectroscopy method with the ion production capabilities of a heavy-ion accelerator is unique and opens the door to frequency metrology of highly-charged heavy ions with all its opportunities.

The study of highly-charged heavy ions holds an immense potential for advancing our understanding of fundamental physics. The few or even single electrons that are bound to the nuclei of these ions, are subjected to extreme electromagnetic fields. This qualifies highly-charged heavy ions as ideal candidates for testing the limits of the Standard Model of particle physics. Furthermore, these ions feature forbidden optical hyperfine-structure transitions which can be measured with highest precision in an optical clock experiment and which can be used to search for unknown physics [1, 2].

Substantial progress has been made in 2024 for the develop of the required setup at the HITRAP facility of GSI in Darmstadt as well as in the preparation of the lab space. The work is primarily conducted by the Helmholtz Young Investigator Group (HYIG) of Peter Micke.

The construction of a new laser laboratory for the quantum logic clock experiment has been completed, including the installation and commissioning of a state-of-the-art laboratory air conditioning to guarantee a draught-free air intake and a constant lab temperature at an acceptable level of humidity (Figure 1), being essential for stable laser operation. Additional technical infrastructure has been installed as well.

The plannings of numerous laser systems for the production of single trapped Be^{+} as logic ions, for Doppler and resolved-sideband laser cooling, and for optical pumping and state preparation are well advanced. This includes in particular the procurement of fiber laser systems and components for the generation of optical sum frequencies and second harmonics to match the required transition frequencies of the ion species. Furthermore, an iodine spectroscopy setup is developed to provide an absolute atomic transition-based reference for laser stabilization.

Beyond that, the experimental setup relies on further key components: At the heart is a Paul trap that requires operation at a cryogenic temperature of 4 K. Major progress has been achieved towards a monolithic trap design which minimizes detrimental micromotion of the trapped ions and features a high quality factor step-up resonator to provide a clean radio frequency of up to several hundreds of volts. The design is driven by elaborate finite-element simulations, and the manufacturing will de done in collaboration with the Physikalisch-Technische Bundesanstalt Braunschweig, the Leibniz University Hannover, and the Max Planck Institute for Nuclear Physics in Heidelberg. The step-up resonator will be based on a planar coil made of a high-temperature superconductor, deposited on a sapphire wafer. First promising tests have been conducted at GSI in a cryogenic test stand at 4 K.

Figure 1: New quantum logic laser laboratory. a) From the outside with the new air conditioning unit. b) From the inside with the first optical table installed.

Also the plannings of the ion transfer beamline which will connect the Paul trap to the *Cooler Penning trap* of the HITRAP decelerator are well advanced. Highly-charged heavy ions will be provided from there at sufficiently low kinetic energy for recapture in the Paul trap where they will be co-trapped with the laser-cooled Be^{+} ions.

The authors acknowledge funding from the Initiative and Networking Fund (IVF) of the Helmholtz Association.

References

[1] M. G. Kozlov *et al.*, Rev. Mod. Phys. **90**, 045005 (2018).

[2] M. S. Safronova *et al.*, Rev. Mod. Phys. **90**, 025008 (2018).

*p.micke@gsi.de

Nuclear quantum memory for hard X-ray wave packets

S. Velten[1,2], L. Bocklage[1,2], X. Zhang[3], K. Schlage[1], A. Panchwanee[1], S. Sadashivaiah[4,5], I. Sergeev[1], O. Leupold[1], A. I. Chumakov[6], O. Kocharovskaya[3], and R. Röhlsberger[4,5,7,1,2]

[1]*DESY, Hamburg, Germany;* [2]*The Hamburg Centre for Ultrafast Imaging CUI, Hamburg, German;* [3]*Texas A&M University, College Station, USA;* [4]*Helmholtz Institute Jena, Jena, Germany;* [5]*GSI Helmholtzzentrum GmbH, Darmstadt, Germany;* [6]*ESRF - The European Synchrotron, Grenoble, France;* [7]*Friedrich-Schiller-Univ. Jena, Germany*

Light is an excellent carrier of information. It is used not only for classical communication technologies but increasingly also for quantum applications such as quantum computing. However, processing light signals is far more difficult compared to the more common electronic signals. Here we have demonstrated how X-ray pulses can be stored and released by a frequency comb in a novel way that could be applicable for future X-ray quantum technologies [1].

In quantum computing, synchronising computational processes requires memory devices that can store and release pieces of quantum information, referred to as qubits, at specific times without loss. In optical quantum computing, qubits are often encoded in properties of photon wave packets, such as polarisation or waveform. However, storing these photons while preserving their quantum state is a major challenge [2].

A common solution involves transferring the quantum state to a long-lived collective excitation in matter. Some protocols allow these systems to re-emit the photon wave packet on demand. One promising approach uses a 'frequency comb', a set of evenly spaced resonances in a material's absorption spectrum. When a photon is absorbed, all comb modes are excited together, forming a coherent collective state. Though these modes rapidly dephase due to their frequency differences, they rephase at specific intervals (echo times), leading to a re-emission of the original photon wave packet as a "photon echo" [3, 4].

This frequency comb protocol has been demonstrated with visible light using strong lasers to create the comb in atomic ensembles. However, creating such combs at X-ray energies is difficult due to the weaker X-ray sources. To address this, we developed a new method [5] using the nuclear transition of the isotope ^{57}Fe at 14.4 keV. Nuclear transitions are extremely narrow, in this case, with a linewidth of just 5 neV, corresponding to a natural lifetime of 141 ns, rendering them ideal for precise temporal control.

In experiments at PETRA III (beamline P01) and ESRF (beamline ID18), we used mechanical motion to shift the resonance frequencies of multiple single-line ^{57}Fe absorber foils, effectively forming a nuclear frequency comb. A short resonant X-ray pulse excites all foils simultaneously, creating a collective comb state that emits an X-ray photon echo at a controlled time. The timing can be adjusted via the velocity spacing of the foils: wider velocity spacing leads to shorter echo delays.

This nuclear frequency comb stored an X-ray wave packet with 33% efficiency and up to 97% fidelity, preserving its temporal shape, see Fig. 1. Importantly, the synchrotron pulses used here had on average less than one resonant photon, proving this system works at the single-photon level, qualifying it as a quantum memory [6] and marking the first such demonstration at X-ray energies [1].

Our work shows that nuclear frequency combs offer a pathway to compact, room-temperature quantum devices operating at short wavelengths. They enable precise manipulation of X-ray photons and can generate "time-bin" qubits, opening new opportunities in quantum optics and technologies involving ultra-narrow nuclear transitions.

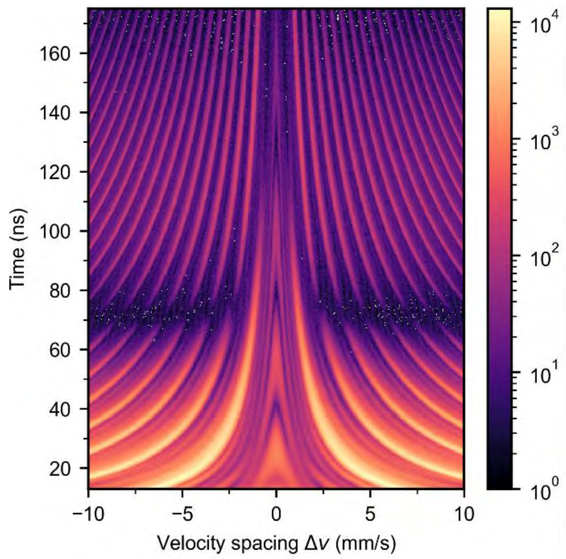

Figure 1: Photon emission after excitation of the nuclear frequency comb. Each emitted photon is counted as a function of its arrival time at the detector after X-ray excitation and the velocity spacing of the frequency comb. The colour scale is logarithmic, showcasing the time instants of high emission probability as sharp bright lines.

References

[1] S. Velten *et al.*, Science Advances **10**, eadn9825 (2024).

[2] A. I. Lvovsky *et al.*, Nat. Photonics **3**, 706 (2009).

[3] M. Afzelius *et al.*, Phys. Rev. A **79**, 052329 (2009).

[4] H. de Riedmatten *et al.*, Nature **456**, 773 (2008).

[5] X. Zhang *et al.*, Phys. Rev. Lett. **123**, 250504 (2019).

[6] Y. Lei *et al.*, Optica **10**, 1511 (2023).

Investigation of lens material for X-ray polarization microscopy

J. Görs*[1,2], B. Marx-Glowna[1,2], R. Lötzsch[1,2], W. Hippler[3], T. Wunderlich[3], S. Sadashivaiah[1,2], Y. Yoshida[1,2], M. Tolkiehn[4], R. Röhlsberger[1,2,3,4], and G. G. Paulus[1,2,3]

[1]*HI Jena, Fröbelstieg 3, 07743 Jena, Germany;* [2]*Helmholtz Centre for Heavy Ion Research (GSI), Planckstr. 1, 64291 Darmstadt, Germany;* [3]*Institute of Optics and Quantum Electronics, Friedrich Schiller University Jena, Max-Wien-Platz 1, 07743 Jena, Germany;* [4]*DESY Photon Science, Notkestr. 85, 22607 Hamburg, Germany*

For X-ray polarization microscopy, the choice of lens material is crucial; polycrystalline materials like beryllium compromise polarization [1]. This study investigates the relationship between crystallite size in polycrystalline materials and the degree of polarization purity, using α-Al_2O_3 powder samples with varying crystallite sizes. Our results demonstrate that even nanometer-sized crystallites significantly degrade polarization purity.

X-ray polarization microscopy combines high-purity X-ray polarimetry with X-ray compound refractive lenses. The highest degrees of polarization purity are achieved with polarimeters, based on reflections at the Brewster angle. For X-rays, the Brewster angle is $45°$. The degree of polarization purity δ_0 characterizes the polarimeter. δ_0 is defined as the ratio between the transmittance of the π- and σ-components. So far, degree of polarization purities of 10^{-11} were achieved [2]. The divergence of the beam limits the degree of polarization purity δ_0 [3]. This has direct implications for combining X-ray polarimetry with X-ray lenses, which must be placed inside the polarimeter, and the focused beam must be recollimated. The lens material must not influence the polarization to achieve the best degree of polarization purity. Materials for X-ray lenses can be grouped into three parts: single-crystalline, polycrystalline, and amorphous lenses. In polycrystalline materials, the crystallite orientation is random, meaning one or more crystallites may fulfill the Bragg condition. As crystals at or near the Bragg condition act as phase plates, a polarization change in the radiation is expected with polycrystalline X-ray lenses. Marx-Glowna et al. [2] have shown that polycrystalline lenses significantly change the measured degree of polarization purity.

This raises the question of how the measured change in polarization relates to the crystallite size of the polycrystalline lens material and how the polarization change depends on the thickness of the polycrystalline material. It's important to determine whether it is possible to simply create a polycrystalline X-ray lens with so small crystallites that there is no measured change in degree of polarization purity.

To investigate the relationship between crystallite size D and the degree of polarization purity δ_0, we performed a systematic investigation using α-Al_2O_3 powder samples. The used α-Al_2O_3 powder is a polishing powder. The measurements were performed at beamline P24 of synchrotron PETRA III (DESY) at an energy of $E = 14.412$ keV. The base of the setup was a four-reflection Si(840) polarimeter. This polarimeter achieved a degree of polarization purity of $\delta_0 = (4.7 \pm 0.2) \cdot 10^{-9}$. The beam onto the sample was limited by a slit of (0.9×1) mm.

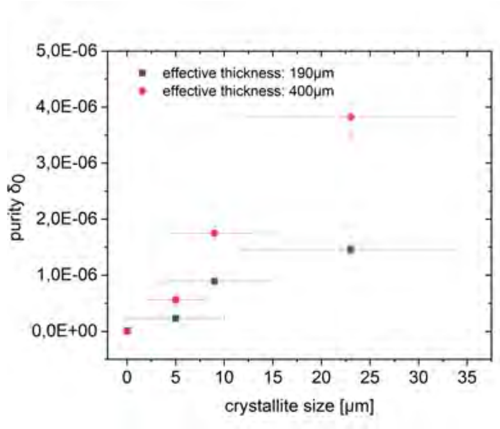

Figure 1: Comparison of the dependence of the degree of polarisation purity δ_0 and the crystallite size D for α-Al_2O_3 powder samples with different thickness; $D = 0\mu m$ corresponds to the measurement of the degree of polarization purity with no sample.

We investigated the change in the measured polarization purity for the α-Al_2O_3 powders with different crystal size distributions (see fig. 1). The larger the crystallite size D of the powdered samples, the worse is the measured degree of polarization purity δ_0. However, even nanometer-sized crystallites change the measured degree of polarization purity significantly. For a crystallite distribution of D$= (46 \pm 4)$ nm, the measured degree of polarization purity becomes $\delta_0 = (1.22 \pm 0.05) \cdot 10^{-8}$. Therefore, X-ray lenses with nanometer-sized crystallites cannot be used for high-purity X-ray polarimetry. We also showed that the more material is inserted into the beam path, the worse the measured degree of polarization purity. For X-ray lenses, the focal length is inversely proportional to the number of lenses and, therefore, to the amount of lens material. This indicates that the smaller the desired focal length, the poorer the degree of polarization purity.

References

[1] B. Grabiger *et al.*, Appl. Phys. Lett. **117**, 201102 (2020).

[2] B. Marx-Glowna *et al.*, New J. Phys. **24**, 053051 (2022).

[3] K. S. Schulze, APL Photonics **3**, 126106 (2018).

*j.goers@hi-jena.gsi.de

Soft X-Ray Transparent Flow Cell with Integrated Dielectrophoretic Control for Single Cell Water Window Microscopy

S. Kaleta*[1,2], J. Reinhard[1,2], S. de Carli[3,4], W. Eschen[1], C. Liu[1], C. Guernth-Marschner[3], E. Hahn[3], L. Licht[1], M. Wünsche[1,2], J. Limpert[1,2,5], S. Fuchs[1,2,6], N. Godino[3], J. Rothhardt[1,2,5], M. Kirschbaum[3], and G. G. Paulus[1,2]

[1] *HI Jena;* [2] *FSU Jena;* [3] *Fraunhofer IZI-BB;* [4] *Institute of Biotechnology, TU Berlin;* [5] *Fraunhofer IOF;* [6] *HS Mittweida*

We integrated a microfluidic flow cell (MFC) into a laboratory-based soft X-ray (SXR) microscope that enables high-resolution imaging of biological samples in aqueous environments under vacuum conditions. Additionally, the cell allows trapping and manipulation of samples using dielectrophoresis. Demonstration of the functionality was performed using nanoparticles and biological samples.

High-resolution imaging of biological samples is essential for a wide range of biological applications, such as gaining insights into cellular processes. The so-called water window (WW) spectral region, defined by the absorption edges of carbon and oxygen (280–530 eV / 2.3–4.4 nm), is particularly well suited for this purpose. It offers a natural structural contrast, as carbon-rich biological material strongly absorbs the radiation while water, dominated by oxygen, offers a penetration up to 25 µm (1% transmission at 430 eV). This allows whole-cell imaging with nanometer resolution. However, WW radiation is absorbed by air after a few centimeters, making vacuum conditions necessary and posing a challenge for imaging living cells.

To address this limitation, a microfluidic flow cell (MFC) was developed by Fraunhofer IZI-BB and IOF in collaboration with HIJ and IOQ [1]. A schematic of the MFC is shown in Fig. 1 (left). The device consists of two silicon wafers, encapsulated in a PEEK housing, each measuring $5 \times 5\,\mathrm{cm}^2$, which are sealed and separated by spacers to maintain a gap of approximately 10 µm. This narrow channel is filled with liquid and allows samples to be suspended directly in the flowing medium. Both wafers feature opposing silicon nitride membrane windows that permit SXR imaging, enabling the observation of biological specimens in a near-native aqueous environment while preserving compatibility with vacuum conditions. Unlike a closed chamber, the MFC includes fluidic connections that allow for the exchange of liquids and samples without the need to break vacuum. Furthermore, integrated electrodes enable the trapping, manipulation and rotation of samples, supporting long-duration exposures and potentially even tomographic imaging.

The MFC was integrated into an existing laboratory-based SXR microscope [2] at the IOQ Jena. The microscope is based on a laser-produced plasma source and uses a zone plate for high-resolution imaging. The plasma is generated by focusing a nanosecond laser into a nitrogen gas jet, producing strong line emission at 2.88 nm. A spatial resolution of 50 nm half-pitch was demonstrated using a Siemens star test target.

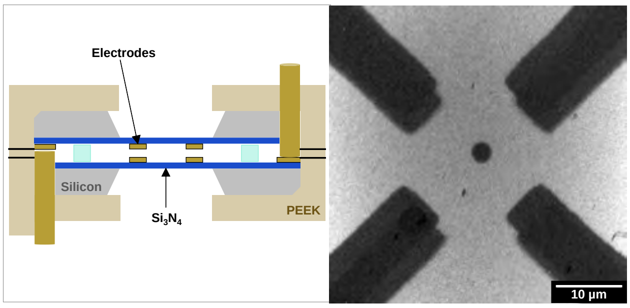

Figure 1: Left: Cross-section of the flow cell. Right: SXR image of a nanobead in the flow cell enclosed by 22 µm of water. Images taken from [1].

To demonstrate the capabilities of the flow cell, nanoparticles were used as initial test samples. A representative image is shown in Fig. 1 (right). A single nanoparticle was imaged through a 22 µm water layer, which exceeds the designed target thickness of 10 µm for optimal SXR imaging. This increased thickness results from bending of the silicon nitride membranes under vacuum and can be reduced in future designs by using smaller membrane windows. The nanoparticle remained stably positioned during a two-hour exposure, held in place by the eight integrated electrodes (four on each membrane), visible as dark rectangles in the figure. In subsequent experiments with biological samples, stable positioning was achieved even overnight, enabling imaging the next day.

In the future, this flow cell will support a wide range of scientific applications, such as studying cellular modifications in different culture media. The cell enables high-resolution SXR imaging of biological samples in liquid and supports tomographic acquisition for 3D structural analysis.

This work was supported by the Fraunhofer Cluster of Excellence "Advanced Photon Sources" CAPS.

References

[1] S. de Carli, J. Reinhard, S. Kaleta *et al.*, in preparation.

[2] J. Reinhard, S. Kaleta *et al.*, Microsc. Microanal. **10**, 84 (2023).

* sophia.kaleta@uni-jena.de

Soft X-Ray Coherence Tomography in the Water Window with a High-Flux High-Harmonic Source

J. Reinhard*[1,2], F. Wiesner[1,2], M. Hennecke[3], T. Sidiropoulos[3], S. Kaleta[1,2], J. Späthe[2], M. Wünsche[1,2], J. J. Abel[2], G. Schmidl[4], J. Plentz[4], U. Hübner[4], K. Freiberg[5], J. Apell[5], M. Schnürer[3], S. Eisebitt[3], S. Fuchs[1,2,6], and G. G. Paulus[1,2]

[1]HI Jena; [2]IOQ, FSU Jena; [3]Max Born Institute Berlin; [4]Leibniz IPHT Jena; [5]OSIM, FSU Jena; [6]HS Mittweida

We present broadband soft-X-ray imaging in the water window using a high-flux lab-scale high-harmonic source with $> 10^6$ photons/eV/s at 500 eV. Enabled by soft X-ray coherence tomography that exploits the full 284–532 eV bandwidth, we can retrieve non-destructively depth profiles of samples with 12-nm axial resolution. It has been demonstrated for Al_2O_3/Pt on ZnO. This broadband technique forms a foundation for element-specific attosecond experiments.

Soft-X-ray imaging within the water-window spectral range ($\sim$ 284–532 eV; 2.3–4.4 nm) is uniquely suited to three-dimensional, non-destructive inspection of nanostructures. Carbon-rich layers exhibit pronounced absorption, while oxygen-dominated oxides and water remain comparatively transparent. Despite this intrinsic chemical contrast, laboratory-scale investigations have long been constrained by the limited photon yield of HHG sources and by the absence of imaging techniques capable of exploiting their broadband emission.

Here, we combine short-wave coherence tomography [1] and a remarkable laser source, which consists of an optical parametric chirped-pulse amplification (OPCPA) system with few-cycle pulses, 28 W and 2.1 μm as an HHG driver. The source delivers more than 5×10^5 photons/eV/s within 295–525 eV, ensuring that soft-X-ray coherence tomography (SXCT) can be conducted. SXCT uses a common-path Fourier setup to extract depth profiles from reflected spectra. The utilized bandwidth of 230 eV yields an axial coherence length and resolution of 12 nm. The lateral resolution is limited to $150 \times 300\ \mu m^2$ as a result of the illumination spot size imposed by the focusing optics.

With this setup a sample consisting of a layered system comprising 70 nm Al_2O_3 and 17–22 nm Pt films on ZnO was investigated. A cross-section was generated performing SXCT at five lateral positions. These results resolve both the buried interfaces and the Pt layer with a thickness gradient. The extracted thicknesses are precisely 71 ± 2 nm (Al_2O_3) and 21 ± 2 nm (Pt), showing an excellent agreement with destructive SEM and TEM measurements.

This first implementation of laboratory water-window SXCT addresses new transmission windows and, thanks to its broad spectral bandwidth, delivers intrinsically high, material-specific resolution that complements EUV coherence tomography. Further improvements in HHG flux and focusing optics will allow single-digit-nanometer axial resolution and sub-micrometer lateral resolution. Using the inherent short pulse duration of HHG, time-resolved investigations of buried nano-interfaces in semiconductors, batteries, and thin films will be possible.

References

[1] F. Wiesner *et al.*, Optica **8**, 230 (2021).

[2] J. Reinhard *et al.*, arXiv preprint 2503.04276 (2025).

* julius.reinhard@uni-jena.de

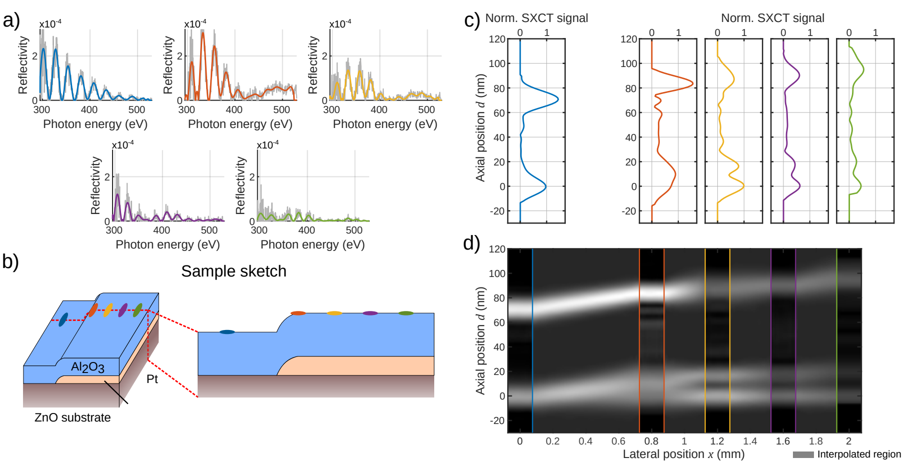

Figure 1: Five SXCT scans across an Al_2O_3/ZnO stack with an buried Pt layer show extra spectral fringes and lower reflectivity where Pt is present. The reconstruction demonstrates 71–75 nm Al_2O_3 and a Pt layer with increasing thickness from 17 nm to 20 nm. Images taken from [2].

Microscopic Ghost Imaging with a Tabletop XUV Source

Sukyoon Oh*[1,2], Monalisa Mallick[1], Thomas Siefke[3], Johannes Mühlenstädt[3], and Christian Spielmann[1,2]

[1]IOQ, FSU Jena; [2]HI Jena, Fröbelstieg 3, 07743 Jena, Germany; [3]IAP, FSU Jena

Ghost Imaging (GI) represents a transformative approach in lensless microscopy, particularly in the extreme ultraviolet (XUV) regime. This report demonstrates a tabletop XUV ghost imaging system utilizing high-harmonic generation (HHG) with 20–40 nm wavelength, low-dose imaging without conventional optics. By systematically evaluating random, Hadamard, and Fourier illumination patterns paired with traditional ghost imaging algorithm and compressive sensing algorithm, we achieved 396% Structural Similarity Index Measure (SSIM) improvement over baseline methods through advanced post-processing techniques.

Motivation—The Abbe criterion fundamentally limits traditional microscopy's resolution, motivating the use of shorter wavelengths such as XUV and soft X-ray radiation. Although XUV from HHG allows nanoscale coherent imaging, applying visible-spectrum techniques directly is difficult due to absorption in optical components. Furthermore, lens-based alternatives like Coherent Diffraction Imaging (CDI) and ptychography are hampered by expensive optics and low photon flux, and traditional XUV optical solutions also exhibit limitations in numerical aperture and aberrations [1]. GI, a lensless correlation-based method effective with broadband, low-flux sources, emerges as a promising approach for high-resolution XUV microscopy, especially where conventional optics are impractical, while also reducing radiation damage [2].

Experimental Setup—The tabletop system (Fig. 1) combines: Tabletop XUV source and ghost imaging setup. The process begins with a seed laser pulse that is first stretched to reduce its peak power before being amplified using a Ti:Sapphire amplifying medium. The amplified pulse is then recompressed by a compressor (800 nm, 35 fs, 1 kHz) and focused onto a nickel tube filled with argon gas, where HHG produces coherent XUV radiation. The generated XUV beam is directed towards the experimental setup, where it passes through an XUV mask. The transmitted light is recorded by an XUV detector, and computational algorithms reconstruct the image, enabling ghost imaging of microscopic features.

Experimental Result—This study systematically evaluated factors impacting XUV ghost imaging quality and implemented mitigation strategies. Hadamard patterns significantly outperformed random and Fourier patterns in image reconstruction. While experimental challenges like misalignment, beam fluctuations, noise, and mask imperfections degrade image quality, they can be effectively addressed. Specifically, position calibration, real pattern usage, histogram equalization, and noise reduction collectively enhance image fidelity, with a combination of position calibration and histogram equalization on real patterns yielding nearly a 400% improvement in SSIM. These results provide a strong framework for optimizing future XUV ghost imaging systems, suggesting that further refinements in alignment, beam stabilization, and noise filtering have the potential to result in even higher-quality reconstructions.

The authors acknowledge funding from Quantum Hub Thüringen.

* sukyoon.oh@hi-jena.gsi.de

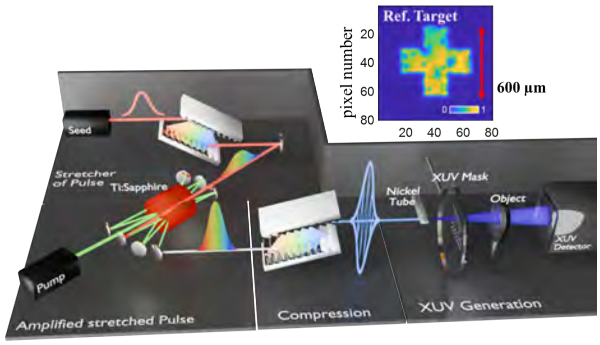

Figure 1: Experimental setup illustrating the generation of XUV radiation using amplified and compressed Ti:sapphire laser pulses focused onto a nickel tube. The generated XUV beam illuminates an object through an XUV mask, and the resulting shadowgraph is detected by an XUV detector. The inset shows a reference target image used for object, with a size indicating 600 µm.

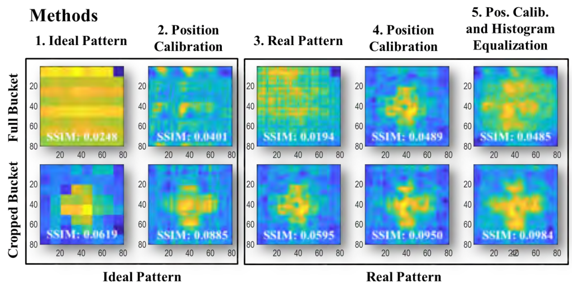

Figure 2: Comparison of XUV Ghost Imaging with ideal and real patterns with position calibration and histogram equalization, showing SSIM values for full and cropped buckets.

References

[1] M. Zürch *et al.*, Sci. Rep. **4**, 7356 (2014).

[2] J. H. Shapiro *et al.*, Phys. Rev. A **78**, 061802 (2008).

Adaptive Weights Match Pursuit (AWMP): Efficient Compressed Sensing Ghost Imaging Algorithm

T. Tian*[1,2], S. Oh[1,2], and C. Spielmann[1,2]

[1]*HI Jena, Fröbelstieg 3, 07743 Jena, Germany;* [2]*IOQ, FSU Jena*

This work presents an adaptive filtering method for Greedy Algorithm-based Ghost Imaging (GI) to suppress noise after domain transforms like DCT or DWT. By leveraging spatial-frequency characteristics, the method improves reconstruction quality while maintaining efficiency, illustrating a strong synergy between physical principles and algorithmic design in compressed sensing GI.

Ghost Imaging (GI), also known as Single-Pixel Imaging (SPI), utilizes detectors with only a single pixel—typically photodiodes. While this hardware setup may seem restrictive, it opens up a broad and fertile ground for software-based optimizations. Among imaging algorithms used in GI/SPI, three main categories stand out: Correspondence Algorithms (CA), Compressed Sensing (CS), and Deep Learning (DL) [1].

Correspondence Algorithms (CA) represent the earliest and most traditional approach. These methods typically require a large number of measurements and tend to yield relatively lower image quality. On the other end of the spectrum, Deep Learning (DL) introduces a novel paradigm that can deliver high-quality reconstructions. However, DL approaches are often computationally intensive and challenging to implement on local or resource-constrained systems. More importantly, despite their performance, DL methods generally lack a solid grounding in physical principles [2].

Compressed Sensing (CS) strikes a compelling balance. By leveraging sparsity in the image domain, CS methods can reconstruct high-quality images from a significantly reduced number of measurements, effectively bypassing the traditional Shannon-Nyquist sampling limit. Within CS-based GI (CSGI), there are two major algorithmic categories: convex optimization methods and greedy algorithms (GAs) [3].

Greedy algorithms are typically more efficient because they perform partial image reconstruction at every iteration. However, they are sensitive to noise, which can degrade image quality. To mitigate this, various optimizations have been proposed, proving effective particularly against additive noise. However, when greedy algorithms are applied to GI, transformations such as the Discrete Cosine Transform (DCT) or Discrete Wavelet Transform (DWT) are usually involved. These transformations alter the nature of the noise, making it non-additive and rendering traditional denoising techniques less effective. In our work, we investigated the mathematical properties of the transformed noise and proposed an adaptive filtering strategy:

*tong.tian@uni-jena.de

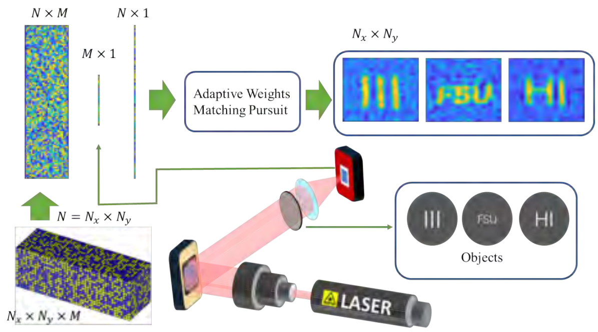

Figure 1: The experimental setup and the procedure of proposed algorithm. Collimated light are modulated by a digital micromirror device (DMD) and the modulation patterns are transferred and flattened. The modulated light then illuminates the object and the total trans-intensity will be collected and moved into the algorithm process.

$$W(\rho_x, \rho_y) = \exp\left(-\frac{\rho_x^2 + \rho_y^2}{2\sigma^2}\right) \times \exp\left(-\alpha\frac{\rho_x}{\eta_x}\right) \exp\left(-\beta\frac{\rho_y}{\eta_y}\right),$$

where (ρ_x, ρ_y) are the coordinators in the transformed domain; σ is employed to control the size of the filter; $\alpha, \beta, \eta_x, \eta_y$ are the parameters for vertical and horizontal directions, respectively. By allocating exponential weights to different elements in the transformed domain, the noises can be significantly reduced while the essential image features are well preserved. Therefore, the proposed algorithm can spend less computational resources in reconstruction and produce high contrasted images.

Our experimental results demonstrated that the proposed filtering method significantly improves reconstruction quality. Beyond its practical efficiency, this method exemplifies the powerful synergy between physical understanding and algorithmic design—highlighting how a deeper grasp of both domains can lead to robust and efficient imaging techniques.

References

[1] G. M. Gibson *et al.*, Opt. Exp. **28**, 19 (2020).

[2] F. Wang *et al.*, Light Sci. Appl. **11**, 1 (2022).

[3] O. Katz *et al.*, Appl. Phys. Lett. **95**, 13110 (2009).

Structured illumination ptychography at 13.5 nm wavelength

W. Eschen*[1,2], C. Liu[1, 2], M. Steinert[2], D. S. Penagos Molina[1, 2], T. Siefke[2, 3], T. Pertsch[2], U. Zeitner[2, 3], J. Limpert[1, 2, 3], and J. Rothhardt[1, 2, 3]

[1] *HI Jena, Fröbelstieg 3, 07743 Jena, Germany;* [2] *IAP, FSU Jena;* [3] *IOF, Fraunhofer Jena*

In recent years, ptychography, a modern computational imaging modality, has enabled high-resolution imaging in the XUV and X-ray regimes, where the fabrication of high-quality lenses remains a significant technological challenge. The advent of modern laser-driven coherent EUV light sources has further extended the capabilities of high-resolution lab-scale ptychographic imaging, which was previously limited to large scale facilities. However, the performance of these lab-based microscopes has so far been constrained by the use of unstructured XUV beams for illumination. In our work, we demonstrate a resolution enhancement by a factor of 4 through the use of a highly structured speckle EUV beam for ptychography.

Ptychography is a lensless imaging modality that enables the computational reconstruction of a coherently illuminated object from its measured diffraction patterns. In recent years, this method has become established particularly in the field of X-ray microscopy at synchrotron facilities where sufficient coherent photon flux (i.e. brightness) is available. Due to its lensless nature, ptychography offers higher resolution and better dose efficiency compared to conventional X-ray microscopy techniques.

In parallel, there has been significant progress in the development of coherent sources in the extreme ultraviolet (XUV) spectral range on a lab scale through high-order harmonic generation (HHG) driven by compact and powerful femtosecond lasers. The combination of these HHG-based XUV sources with ptychography opens up new possibilities for high-resolution microscopy that were previously only feasible at synchrotrons [1].

In our research, we investigated the impact of structured illumination on the image quality in XUV ptychography at 13.5 nm wavelength [2]. Previous XUV ptychography experiments predominantly employed unstructured beams for sample illumination. However, our results demonstrate that structured beams offer significant advantages. In particular, structured illumination enables higher spatial resolution and simultaneously improves the convergence of the numerical reconstruction algorithms used. This behavior can be explained by the fact that the measured diffraction patterns correspond to a convolution of the object spectrum with the illumination spectrum. Structured beams exhibit a broader spectrum, which leads to higher diffraction angles and thus provides access to additional information about the sample. To realize structured beams in XUV ptychography, we developed nanostructured masks [2], which were positioned directly in front of the sample at a distance of approximately 100 µm. In our experiments, two different types of masks were used. The first mask was a simple pinhole aperture, which produced a soft, unstructured beam (Fig. 1 a). Image reconstruction with this illumination resulted in a low spatial resolution of 125 nm, and the reconstructed images exhibited clearly visible artifacts. In the next step, we replaced the pinhole aperture with a highly structured, phase-shifting diffuser mask. This generated a diffuse speckle pattern with high structural diversity on the sample (Fig. 1 b). The reconstruction of the object using this structured illumination yielded a significantly higher resolution of 32 nm and a markedly improved image quality. In the future, the findings of our work will enable high-resolution imaging of weakly scattering specimens, such as bacteria, at lower radiation doses.

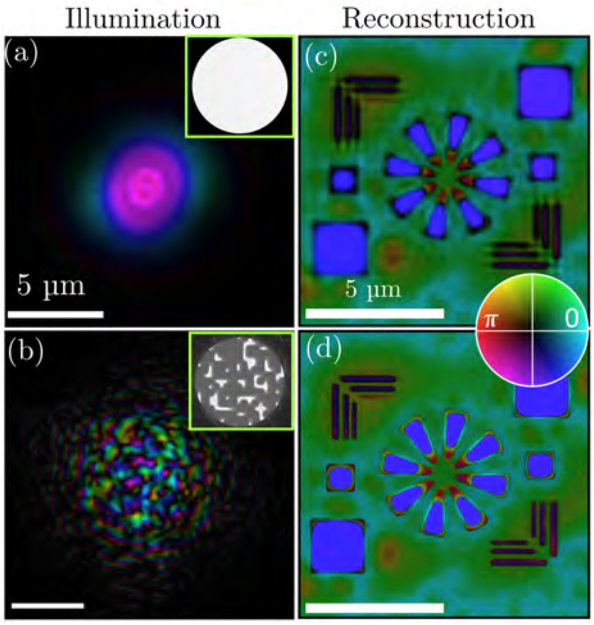

Figure 1: Figure illustrating that unstructured illumination (a) results in low resolution and visible reconstruction artifacts (c), whereas highly structured illumination (b) yields higher image quality with no observable artifacts [2].

The authors acknowledge funding from the Thüringer Aufbaubank (2019 FGI 0013), the Helmholtz Association (FISCOV, Ptychography 4.0, ZT-I-PF-4-018 AsoftXm), and the Fraunhofer-Gesellschaft (CAPS).

References

[1] M. Seaberg *et al.*, Optica **1**, 39-44 (2014).

[2] W. Eschen *et al.*, Opt. Express **32**, 3480-3491 (2024).

* wilhelm.eschen@uni-jena.de

Dielectronic Recombination of Ne^{3+} Measured at CRYRING@ESR

E.-O. Hanu*[1,2,3], M. Lestinsky[2], C. Brandau[2], M. Fogle[7], P.-M. Hillenbrand[2], M. Looshorn[4,5], E. B. Menz[2,6], S. Schippers[4,5], S. Wang[4,5], and Th. Stöhlker[1,2]

[1] *HI Jena, Fröbelstieg 3, 07743 Jena;* [2] *GSI Helmholtzzentrum für Schwerionenforschung, 64291, Darmstadt;* [3] *Institut für Kernphysik, Goethe Universität, 60438, Frankfurt am Main;* [4] *I. Physikalisches Institut, Justus-Liebig-Universitat Giessen, 35392 Giessen;* [5] *Helmholtz Forschungsakedemie Hessen for FAIR (HFHF), 35392 Campus Giessen;* [6] *Institut für Kernphysik, Universität zu Köln, 50937 Köln;* [7] *Department of Physics, Auburn University, 36832 Auburn, USA*

This study investigates the dielectronic recombination of low-charged neon ions, specifically nitrogen-like Ne^{3+}, using the ultra-cold electron beam at CRYRING@ESR. The experiment aims to improve the accuracy of modeling charge state distributions in cold photoionized plasma by investigating low-energy dielectronic recombination rate coefficients, with a particular emphasis on resonances below 0.5 eV.

Neon, among the most abundant elements in the present day universe, is widely observed in various charge states in spectra of astrophysical objects. Dielectronic recombination (DR) — the resonant capture of a free electron with simultaneous excitation of a bound electron — is the dominant electron - ion recombination process and modifies the charge state distributions in astrophysical plasmas. This process occurs when the kinetic energy of the free electron matches the energy difference between two bound states of the ion, creating a doubly excited intermediate state. While theoretical prediction of DR rates are quite reliable for higher energies but has been shown to be unreliable for lower energies in the region of a few eV and below [1]. Accurate recombination rates for a light ion species in low charge states can provide valuable data for modeling cold plasma environments such as planetary nebulae.

The experiment was conducted at the CRYRING@ESR, storage ring at GSI in Darmstadt, where beams of specific elements and charge states are stored, cooled, and merged with a monoenergetic electron beam for DR measurements [2]. The ultra-cold electron beam enables high-resolution DR rate measurements at low collision energies — crucial for understanding recombination in cold photoionized plasmas [3]. Recombined ions were detected by a scintillation particle detector placed in the section following the electron cooler, where the product beam is well separated from the stored beam.

The ions were injected from an ECRIS at the local injector, accelerated to an energy of 2.23 MeV/u, stored and electron cooled with an average of 5.5×10^{6} ions per cycle. The merged beams DR spectrum was measured across several overlapping energy ranges, covering a total range of -0.5 to 24 eV in the center-of-mass framework, where the dominant resonances arise from $\Delta n=0$ transitions — meaning the electron is excited within the same principal quantum shell — through $2s\rightarrow 2p$ core excitation into $2s2p^4\ ^4P$ electronic configuration.

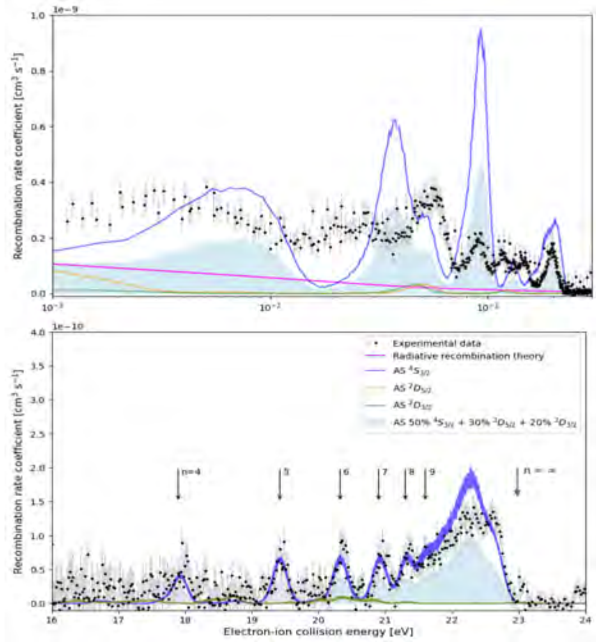

Figure 1: Recombination rate coefficient for the selected collision energy ranges are shown. The lightblue area represents a thermal distribution of parent ions in their ground state and relevant metastable states. Here, the autostructure theory is shifted by -0.1 eV.

In particular, we observed strong DR resonances at energies below 0.5 eV, with the associated merged beam recombination rate coefficient nearly as strong as at the series limit ($2s2p^4\ ^4P_{1/2}$: 22.91 eV). Additionally, the level population fractions as a function of storage time were modeled to compare the theoretical DR of a mixed-ion beam with the experimental data.

Detailed analysis of the data is currently ongoing and we have since been able to complete another measurement – on O^{2+} – which also falls within our programme of astrophysically motivated DR experiments.

References

[1] N. R. Badnell *et al.*, Astrophys. J. **804**, 100 (2015).

[2] M. Lestinsky *et al.*, Phys. Rev. Let. **100**, 033001 (2008).

[3] M. Lestinsky *et al.*, Eur. Phys. J Special Topics **225**, 797–882 (2016).

* e.hanu@gsi.de

Precise determination of K_α transition energies in U^{90+} using novel microcalorimeter detectors

G. Weber*[1,2], Ph. Pfäfflein[1,2,3], S. Allgeier[4], S. Bernitt[1,2,3], A. Borovik[6], L. Duval[7], A. Fleischmann[4], M. Friedrich[4], O. Forstner[1,2,3], J. Glorius[2], A. Gumberidze[2], Ch. Hahn[1,2], D. Hengstler[4], M. O. Herdrich[1,2,3], P.-M. Hillenbrand[2], A. Kalinin[2], M. Kiffer[1,2,3], F. M. Kröger[1,2,3], M. Kubullek[3], P. Kuntz[4], M. Lestinsky[2], B. Löher[2], E. B. Menz[1,2,3], T. Over[1,2,3], N. Petridis[2], S. Ringleb[1,2,3], R. S. Sidhu[4], U. Spillmann[2], S. Trotsenko[1,2], A. Warczak[5], B. Zhu[1,2,3], C. Enss[4], and Th. Stöhlker[1,2,3]

[1]HI Jena; [2]GSI, Darmstadt; [3]IOQ, FSU Jena; [4]KIP, Heidelberg University; [5]Jagiellonian University, Krakow; [6]I. PI, Gießen University; [7]Sorbonne Université, Paris

Precision spectroscopy of x-ray transitions in few-electron, high-Z systems is an indispensable tool for the study of bound-state quantum electrodynamics (QED) in the presence of strongest electromagnetic fields. Such measurements significantly profit from the development of low-temperature calorimetric detectors, such as metallic magnetic microcalorimeters (MMC), which combine a high spectral resolution, similar to crystal spectrometers, with a broad bandwith acceptance that is comparable to semiconductor detectors. We report on the first precise determination of K_α transition energies in U^{90+}.

The spectral data was obtained during the 2021 beam time block at the electron cooler of CRYRING@ESR, using two novel MMC detectors tailored for a photon energy of $100\,\mathrm{keV}$. An U^{91+} beam was provided by the ESR with a kinetic energy of $10.255\,\mathrm{MeV\,u^{-1}}$. After injection into into CRYRING@ESR the beam was continuously electron-cooled at a voltage of $5634.5\,\mathrm{V}$ and an electron current of $30.5\,\mathrm{mA}$. Recombination of cooler electron with the stored U^{91+} ions resulted in the formation of excited U^{90+} ions which subsequently decayed to the ground state via radiative cascades.

In this experiment, the MMC detectors were fully integrated in the experimental environment of the storage ring facility for the first time, following an extensive benchmarking and preparation phase at GSI. Using two detectors and exploiting the favourable observation geometry of $0°$ and $180°$ allowed for a measurement in which the remaining systematic uncertainty stems from the quality of the energy calibration instead of hard-to-control-for uncertainties of the experimental geometry. Moreover, a coincidence measurement, which is well established for semiconductor detectors, has been demonstrated with the new type of detectors for the first time, yielding virtually background free spectra. The experiment succeeded in achieving a spectral resolution of better than 100 eV FWHM. As a consequence, it was possible to disentangle the individual components of the K_α radiation in helium-like uranium, see Fig. 1.

Applying a spectral model of four lines with Voigt-

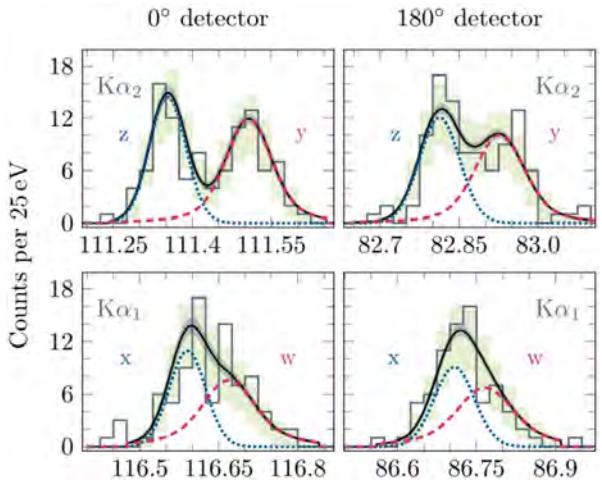

Figure 1: Graph of the measured K_α spectra (histogram in gray) together with the corresponding fit results. The model function is drawn as solid black lines. The gray bands surrounding them represent a one standard deviation wide confidence range resulting from the uncertainty of the fit result. The effects of counting statistics (Poisson distribution, 68 % interval) are represented by the light green area. For visual guidance the Voigt-shaped profiles of the individual components of the K_α transitions are shown as colored dashed lines.

shaped profiles to the experimental data resulted in the first high-accuracy determination of their transition energies in a heavy system. The results, which are in good agreement with state-of-the-art QED calculations, were recently published in [1].

This work was conducted in the framework of the SPARC collaboration, experiment E138 of FAIR Phase-0 supported by GSI. We acknowledge support by the ERC under the European Union's Horizon 2020 research, by the innovation program (grants 824109 "EMP") as well as by ErUM FSP T05 - "Aufbau von APPA bei FAIR" (BMBF grants 05P19SJFAA and 05P19VHFA1).

References

[1] Ph. Pfäfflein *et al.*, Phys. Rev. Lett. **134**, 153001 (2025).

* g.weber@hi-jena.gsi.de

First Results of Machine Learning Techniques for Microcalorimeters

M.O. Herdrich*[1,2,3], T. Mattis[4], C. Enss[5], and Th. Stöhlker[1,2,3]

[1] *HI Jena, Germany;* [2] *IOQ, FSU Jena, Germany;* [3] *GSI, Darmstadt, Germany;* [4] *Hasso Plattner Institute, Potsdam, Germany;* [5] *Kirchhoff-Institute for Physics, RKU Heidelberg, Germany*

Several manual steps are required to optimize the operation of individual MMC detector channels as well as the analysis of their recorded signals. To improve the scalability of the data analysis, multiple machine learning techniques have been investigated to automate the pulse shape classification and feature extraction. We report on first results of their application.

During the last decades, *metallic magnetic calorimeters* (MMCs) – like the maXs-series detectors developed within the SPARC collaboration – have evolved to become promising tools for high-resolution x-ray spectrometry. Their unique working principle of measuring the temperature increase upon absorption of the incident photon's energy combine the advantages of traditional energy- and wavelength-dispersive photon detectors, making them well suited for precison spectroscopy measurments in fundamental atomic physics research.

Their operation, however, requires the utilization of specialized hardware like SQUID-arrays for the amplification of magnetic flux changes in the sensor at fractions of the magnetic flux quantum. These systems must be tuned carefully to exploit the full capabilities of the MMC detectors. Furthermore, the high sensitivity of the sensor leads to a strong susceptibility to external disturbances, which can lead to artifacts like gain-drift of the sensors over time [1]. To achieve highest detector performances, these artifacts need to be corrected for in software, which was developed and tested extensively in the past years [2]. Typically MMCs consist of arrays of individual sensors to cover a larger active detection area on a single chip, while keeping the thermal capacity of each sensor as low as possible. So far, algorithmic parameters for each detector channels have been tuned and optimized separately, which is a time-consuming and error-prone process. Future development of MMCs aims to increase the number of pixels by orders of magnitude, making this approach not feasible anymore. Therefore, tools from *machine learning* (ML) research have been explored to automate the procedure for scalability and to improve the robustness of the data analysis.

The investigated methods range from classical machine learning techniques, like *principle component analysis* (PCA) in combination with cluster searching for a reliable classification of the pulse shape, to more advanced *neural network* (NN) architectures like *convolutional variational auto-encoders* (CVAEs) for the extraction of features from raw pulses. The latter approach is capable of embedding MMC pulses into a lower dimensional latent space, which can then easily be mapped back to the original pulse parameters - like amplitude, timing, triggering, etc. - using a multi-layer perceptron (MLP). To cover a wide range of input parameters, simulated pulses were used during the training process. Measured filter performances of the NN surpassed the results of traditional finite response filter base approaches in every simulated scenario. More importantly, though, it was demonstrated (see fig. 1) that a NN trained on purely synthetic data was already capable of successfully reconstructing the real world calibration spectrum recorded during a dedicated high precision spectroscopy experiment [3]. This could be enhanced by including real world data into the training process by adding fine-tuning steps of the auto-encoder or by using adversarial training methods to refine the training pulse synthesis. More advanced artifact simulation methods could be implemented to include temperature drift correction into the NN-bases extraction process itself. In the future, optimization of high-dimensional hardware parameters could be performed as well using reinforcement learning (RL) methods, which would allow for a fully automated tuning process of the MMCs.

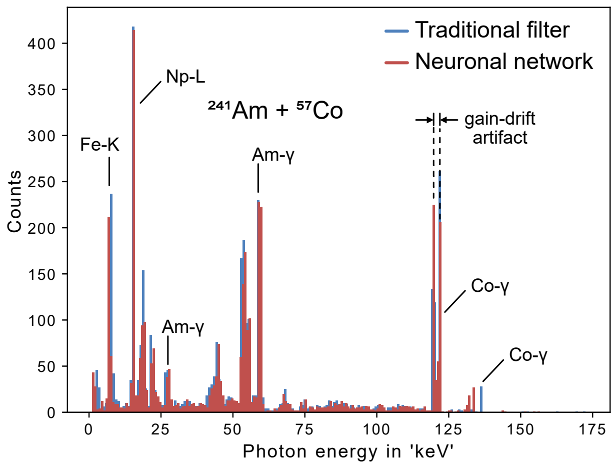

Figure 1: The presented calibration spectrum contains several transitions of ^{241}Am and ^{57}Co and was recorded with a maXs-100 detector. The comparison between the reconstruction using a NN trained on synthetic data and a traditional finite response filter shows the feasibility of utilizing ML techniques in our MMC pulse shape analysis.

References

[1] M. O. Herdrich *et al.*, Atoms **11**, 13 (2023).

[2] M. O. Herdrich, Ph.D. Thesis, FSU Jena, Germany (2023).

[3] Ph. Pfäfflein *et al.*, Phys. Rev. Lett. **134**, 153001 (2025).

*m.o.herdrich@hi-jena.gsi.de

Preparation of a Test Experiment for a Novel Compton Telescope

T. Over*[1,2,3], A. Kononov[2], T. Krings[4], W. Middents[1,2,3], U. Spillmann[2], G. Weber[1,2], and Th. Stöhlker[1,2,3]

[1] *HI Jena, Germany;* [2] *GSI, Darmstadt, Germany;* [3] *IOQ, FSU Jena, Germany;* [4] *FZ Jülich, Germany*

Compton polarimetry is an essential tool to obtain a detailed understanding of fundamental radiative processes in the hard x-ray regime, i.e. for photon energies from above 50 keV up to the MeV range. A novel polarimeter with two double-sided segmented planar crystals, a Si(Li) and a HPGe detector, which is optimized for the energy range between 60 keV and 1 MeV was developed within the SPARC collaboration. A first detector test experiment at the experimental storage ring ESR at GSI is scheduled in 2026.

Compton polarimetry is an established technique to determine the (linear) polarization of a photon beam in the hard x-ray regime (above 20 keV). It depends on the anisotropy of the Compton scattering with respect to the electric field vector of the photon beam. For this purpose, multiple 2D sensitive semiconductor detectors have been constructed within the SPARC collaboration as dedicated Compton polarimeters. The most recent development is a novel Compton telescope, equipped with two detector crystals, a Si(Li) crystal followed by a HPGe crystal, both segmented on front and back side. In contrast to the previous Compton polarimeters designed within SPARC, the new telescope structure enables an extended feasable energy range up to the MeV regime. A detailed description of the Compton telescope, which is being commissioned, can be found in [1].

The expected detection efficiency of fully registered Compton scattering events by the Compton telescope was estimated for multiple photon energies between 100 keV and 1 MeV via a simulation of the detection response [2]. For comparison, also the estimated detection efficiency for a previous stage of the Compton polarimeter, only consisting of one segmented Si(Li) detector was simulated. The result is presented in Figure 1. The additional HPGe detector in the Compton telescope leads to a strongly increased detection efficiency of full Compton scattering events due to the higher photon absorption probability of germanium in comparison to the simple Compton polarimeter based on a Si(Li) crystal only. Additionally, next to full Compton events being registered in either the Si(Li) crystal or the HPGe crystal, the telescope structure now enables scattering events, where the first detector (Si(Li)) can now act as scatterer, measuring the recoil electron, and the second crystal (HPGe) acts as the absorber of the scattered photon. This is of greater importance at higher energies, as scattering to forward angles is more pronounced with rising energies.

To verify the simulated efficiency and to test the performance of the new Compton telescope, a first detector test experiment is planned. The polarization of photons, emitted in the radiative electron capture (REC) process, will be measured at the GSI facility in Darmstadt, Germany. This process and its photon polarization features has been studied in detail in prior experiments [3, 4] and therefore provides an ideal test case for the novel Compton telescope. In the planned experiment a bare uranium beam will be used as the projectile at an injection energy of 400 MeV/u interacting with a molecular hydrogen gas jet target. The Compton telescope will be placed at an observation angle of 35°, detecting the emitted photons at an energy of 593 keV, as depicted in Figure 2. For redundancy an additional polarimeter, with only a Si(Li) crystal, will be positioned at an observation angle of 145°.

*t.over@hi-jena.gsi.de

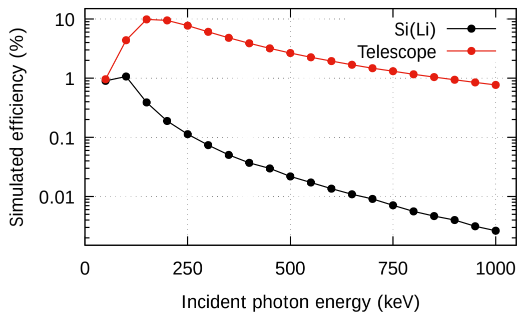

Figure 1: Simulated efficiency of detecting a Compton event of the previous polarimeter with one Si(Li) crystal (black) and the novel Compton telescope with two crystals (red).

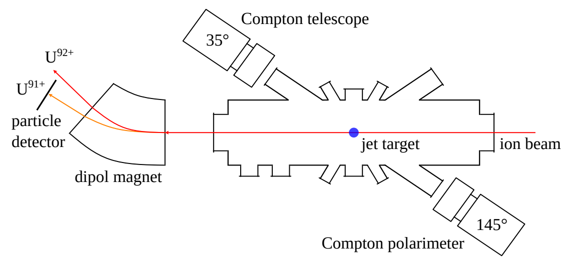

Figure 2: Scheme of the experimental setup at the gas jet target of the ESR at GSI.

References

[1] W. Middents *et al.*, HIJAR, 44 (2023).

[2] G. Weber *et al.*, Phys. Scr. **2011**, 014034 (2011).

[3] S. Tashenov *et al.*, Phys. Rev. Lett. **97**, 223202 (2006).

[4] M. Vockert *et al.*, Phys. Rev. A **99**, 052702 (2019).

Simulation of the Polarization Transfer in Compton Scattering from Atoms

W. Middents*[1,2,3], T. Over[1,2,3], G. Weber[1,2], and Th. Stöhlker[1,2,3]

[1]*HI Jena, 07743 Jena, Germany;* [2]*GSI, 64291 Darmstadt, Germany;* [3]*IOQ, FSU Jena, 07743 Jena, Germany*

Regarding the Compton scattering off atomically bound electrons, the scattering process is influenced by the momentum distribution of the bound electrons, resulting in a broadening of the scattered photon energy, the so-called Compton profile, which is well understood and described in the impulse approximation. However, the influence of the electron momentum distribution on the polarization transfer from incident to scattered photon beam has not yet been investigated and is the subject of a simulation developed by us.

Compton scattering is the inelastic scattering process of an incident photon off an electron. In the most basic picture of Compton scattering, the electron is assumed to be free and at rest. In this framework, the energy $\hbar\omega'$ of a scattered photon beam is well defined by the incident photon energy $\hbar\omega$ and the polar scattering angle θ. The interaction cross section and the polarization transfer from incident to scattered photon beam can be calculated by the transfer matrix formalism [1, 2]. In the Compton scattering off bound electrons, the scattering process is influenced by the electron momentum. This is considered in the (relativistic) impulse approximation (IA) [3, 4], which treats the scattering process as the inelastic scattering off an ensemble of free electrons with a momentum distribution according to the electron momentum density. The double differential cross section (DDCS) of Compton scattering can be calculated by an integration over the electron momenta. This results in a Doppler broadening of the otherwise sharp energy of the scattered photon, the Compton profile.

While the Compton profile is well described in the IA, a thorough investigation of the polarization transfer from incident to scattered photon beam was so far pending. In a recent experiment on elastic and inelastic hard x-ray scattering processes, we were able to perform a first test on the polarization transfer in the Compton scattering off bound electrons. The results show a change of the polarization of the scattered photon beam across the Compton profile [5]. This lead us to develop a simulation based on the concept of the IA, which describes the Compton scattering off atomic targets and provides results for both the DDCS as well as the linear polarization characteristics of the scattered photons. In the simulation, N scattering events are simulated and for each individual simulated scattering event, a 3D electron momentum is sampled from the electron momentum distribution of the target atom. The event is Lorentz transformed to the electron rest frame, where the Compton scattering can be calculated according to the transfer matrix formalism, providing results for the scattered photon energy, scattering cross section and linear polarization of the scattered photon beam. In the laboratory frame, the results of the individual scattering events are superimposed, resulting in the DDCS, which follows the Compton profile and the polarization of the scattered photon beam across the Compton profile. Figure 1 shows example results of the simulation for scattering a 175 keV photon beam with a linear polarization of $P_{1,i} = 0.99$ off a gold atom at $\theta = 63.4°$ compared to experimental results. The simulated DDCS fits well to the experimental data and is also in good agreement with other calculations in the IA. The simulation predicts a variation of the linear polarization across the Compton profile, which fits well to experimental data. The change in polarization can be linked to the influence of the electron momentum on the scattering process.

The results of this simulation are submitted to New Journal of Physics and are currently under review. The simulation is available for open use [6].

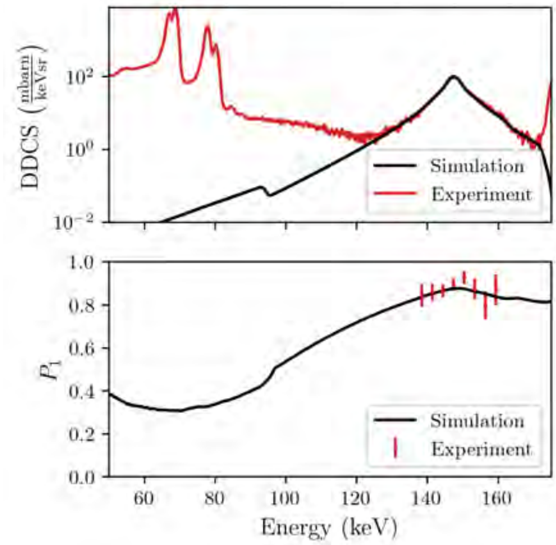

Figure 1: Top: DDCS of a 175 keV photon beam with an incident linear polarization of $P_{1,i} = 0.99$ Compton scattering off a gold target. Bottom: Linear polarization of the scattered photon beam.

The authors acknowledge funding from ErUM-FSP APPA (BMBF ° 05P19SJFAA).

References

[1] W. H. McMaster, Rev. Mod. Phys. **33**, 8 (1961).

[2] U. Fano, J. Opt. Soc. Am. **39**, 859 (1949).

[3] R. Ribberfors, Phys. Rev. B **12**, 2067 (1975).

[4] R. H. Pratt *et al.*, Rad. Phys. Chem. **79**, 124 (2010).

[5] T. Over *et al.*, HIJ Annual Report 2023, 52 (2024).

[6] `https://doi.org/10.5281/zenodo.15386615`

*w.middents@hi-jena.gsi.de

Commissioning DCCC-GRP Beamline Cryostat

V. Tympel*[1,2] and L. Crescimbeni[3]

[1]HI Jena, Fröbelstieg 3, 07743 Jena, Germany; [2]GSI, Planckstraße 1, Darmstadt; [3]University of Jena

For the routine operation of Cryogenic Current Comparator (CCC) systems in the accelerator environment, it is important to understand the pathways of external disturbances. For this purpose, a non-metallic GRP beamline cryostat with a dual-core CCC was developed as part of the BMBF project AoCCC (05P21SJRB1, 2021-24). This cryostat can accommodate beamlines up to a diameter of 50 cm and allows dry operation for a few days.

At the beginning of 2024, the GRP cryostat developed by Supracon AG was handed over [1]. The first cooling with liquid helium took place together and without any problems. The required service life was exceeded. Unfortunately, none of the three SQUIDs worked. Only after a temporary shielding with aluminium foil and its grounding does one of the SQUIDs work, namely the insensitive one. This means that the existing external superconducting shielding of the CCC sensor is not sufficient. The entire close-up range has to be electrically shielded and grounded (Fig. 1). It must also be prevented that RF interference can reach the immediate vicinity of the CCC sensor via electrical supply cables.

One of the main topics was to clarify the question of whether dry operation is advantageous in terms of avoiding acoustic interference, as there are contradictory statements from the users CERN and GSI in this regard. With this cryostat it is possible to operate the CCC sensor for about four days without direct contact with the helium bath, i.e. in a dry mode. The sensor was designed as a dual-core CCC (DCCC), i.e. with two identical pickup coils. Acoustic disturbances were created with a subwoofer at a distance of 3 m. The laboratory experiment at the DCCC showed that in dry operation it is possible that the sensitivity to acoustic interference can be increased as well as decreased. The only difference between the two coils is their position in the arrangement. Nevertheless, they showed different amplitude and phase behavior with regard to the acoustic signals in dry or wet operation. Thus both are possible. The dry operation can be advantageous, but it does not have to be (Fig 2.).

Another important question regarding the improvement of system stability is: What disturbance frequency on supply lines or the beamline passage can lead to jumps in the SQUID electronics. The measurements showed that particular attention should be paid to frequencies in the range of resonance of meander shielding capacitors/core inductance. For the Pb-DCCC-Sm-300, the range around 670 kHz. Filters in the cables have to be designed accordingly.

*v.tympel@hi-jena.gsi.de

Figure 1: Copper shielded DCCC-GRP beamline cryostat.

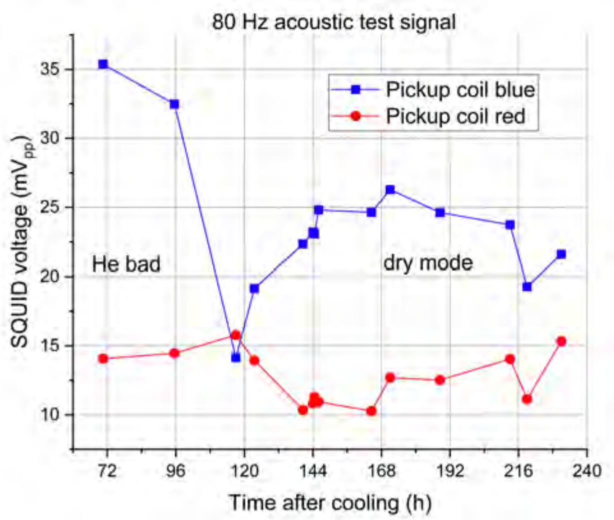

Figure 2: Comparison of helium bath operation and dry mode.

References

[1] H. Nowak *et al.*, GFK-Cryostat for a Cryogenic Current Comparator, ICEC29-ICMC 2024, Geneva, Switzerland.

Brilliant ion sources for strong-field laser and future EBIT or accelerator applications

F. Machalett*[1,2,3], B. Ying[1,2], M. Kübel[1,2], A. Sommerfeld[2], J. Hacker[2], Th. Stöhlker[1,2,3], and G. G. Paulus[1,2]

[1]*Helmholtz Institute Jena, 07743 Jena, Germany;* [2]*Institute of Optics and Quantum Electronics, Friedrich Schiller University Jena, 07743 Jena, Germany;* [3]*GSI Helmholtz-Zentrum für Schwerionenforschung, 64291 Darmstadt, Germany*

Liquid metal ion sources (LMIS) have small emission points and a high emission current density. Therefore, the ion beams already have a very small phase space volume already at emission. These properties make LMIS suitable ion sources for various future applications. We have developed and commissioned a special preparation and vacuum test chamber for the controlled and high-precision preparation of ion emitters. This allows the properties of the emitter substances to be tested on a microscopic scale and the ion emission to be observed under high voltage.

The development of new liquid metal ion sources (LMIS) moves this type of ion source from former special applications in nano-structuring and satellite technology to the center of new research directions. These research topics include strong-field laser physics as well as highly charged ion generation in EBIT (Electron Beam Ion Trap) for basic research.

We improved the quality of the ion emitters and preparation processes on the microscopic scale at emitter cleaning, wetting with source feed material and test in vacuum under high voltage [1]. This gives us the possibilty to understand and optimize the material properties, such as melting, wetting, flowing and evaporation for a much better controlling of the source behavior.

Important quality factors of LMIS are [1]: high brilliance of 10^6 A cm^{-2} sr^{-1}, long service life (approx. 1000 h per emitter), low melting metals / alloys, ion currents of 5 µA – max. 1 mA, continuous and triggered beams are possible.

Fig. 1 (a) shows the new developed UHV test chamber for the preparation, testing and optimization of ion emitters down to the microscopic scale and (b) the emitter, already wetted with source feed material, e.g. gallium.

In Fig. 2 (a) we can see a needle during ion emission and wetted with a molten Au-Si alloy. Fig. 2 (b) shows an operating Ga emitter also with light emission, caused by the interaction of ions with gas particles.

We continued strong-field laser experiments and used the high-brightness LMIS to the ion laser system for 3D coincidence momentum spectroscopy.[2]. We carried out studies on the ultrafast laser-induced fragmentation and ionization.

The authors acknowledge support from GSI Innovation Fund as an internal funding instrument for technology transfer of GSI. The collaboration with JEVATEC GmbH Jena is acknowledged.

*f.machalett@gsi.de

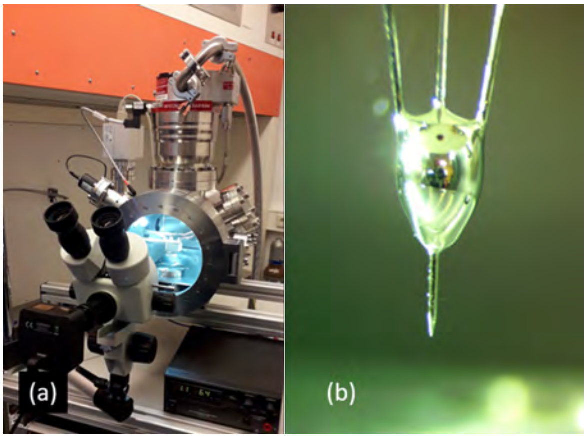

Figure 1: (a) UHV test chamber for the preparation, testing and optimization of ion emitters on a microscopic scale, (b) emitter wetted with a low-melting-point metal as source feed material, e.g. gallium.

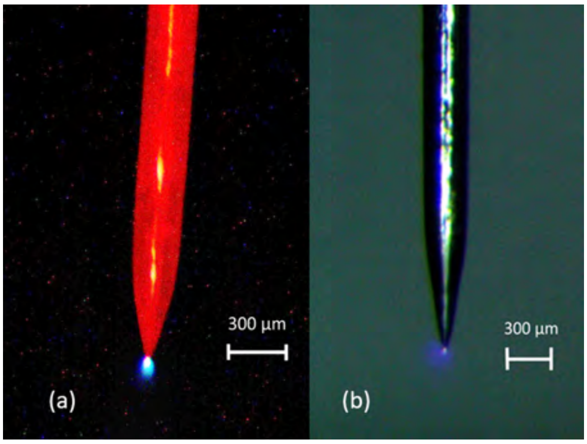

Figure 2: (a) Ion emitter needle of Au-Si with light emission, indicating the ion emission, caused by interactions of ions with gas particles. (b) Ion emitter needle, wetted with gallium, showing the ion interaction with gas. The ion generation occurs in a region, which is about 1000 times smaller than the light emitting region.

References

[1] F. Machalett, P. Seidel, Focused Ion Beams and Some Selected Applications, EAP, Wiley (2019).

[2] B. Ying *et al.*, J. Phys. B **54**, 174002 (2021).

Compact ion-cloud targets in a well-defined quantum state

S. Ringleb*[1], M. Kiffer[1], M. Vogel[2], and Th. Stöhlker[1,2,3]

[1] *Friedrich-Schiller-Universität Jena, 07743 Jena, Germany;* [2] *GSI Helmholtzzentrum für Schwerionenforschung GmbH, 64291 Darmstadt, Germany;* [3] *Helmholtz-Institut Jena, 07743 Jena, Germany*

In the HILITE experiment we intend to further ionise highly charged ions in the centre of a Penning trap. In this environment, we are able to produce dense clouds of ions in a well-define quantum state. To this end, we have elaborated a method to cool ions in radial and axial direction and measure the ion cloud characteristics.

For the investigation of the interaction of ultra-intense laser pulses beyond intensities of $10^{19}\,\mathrm{W/cm^2}$, highly charged ions are ideal interaction partners as the electric field of the laser is of the same order of magnitude as the electric field between electron and the nucleus.

To prepare well-defined targets of highly charged ions, we use the HILITE setup which is a Penning trap setup capable of capturing ions from an external source and prepare them for laser experiments within about 100 ms [1]. As ion source we use an Electron-Beam Ion Trap (EBIT) which delivers highly charged ions in the low-Z regime in bunches of 10.000 to 30.000 ions. By use of the dynamic-ion-capture technique, the ions are decelerated in flight with a pulsed drift tube and are then captured in the Penning trap by appropriate tuning of the timing.

The trap voltage is chosen in the way that the ions are immediately trapped in a harmonic potential, brought into resonance with a resonator, and cooled in axial direction within tens of milliseconds [2]. In consequence, the ions are confined axially close to the trap centre. During this cooling process, the ion signal is acquired (see Figure 1) and the number of ions as well as the final axial energy and hence the ion distribution width can be determined.

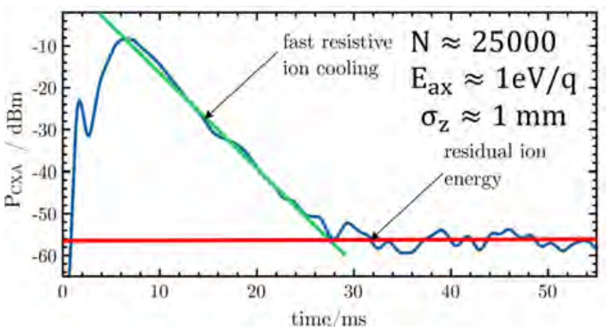

Figure 1: Evolution of the ion signal of stored ions. The slope is directly proportional to the ion number and the residual energy is a measure for the final ion energy.

In contrast, the radial direction cannot be cooled using resistive cooling. Before careful adjustment, the ions typically are stored on a large magnetron radius and a smaller but significant modified cyclotron radius. The radial confinement is tuned by proper alignment of the ion-beam trajectory with the axis of the magnetic field of the setup. Here, the non-zero magnetron radius is due to an offset of the beam direction to the magnetic field axis and the cyclotron radius is caused by a non-zero angle between ion trajectory and the magnet's axis. For ion beam tuning we use three sets of so-called Sikler lense which allow beside ion focussing also ion beam steering.

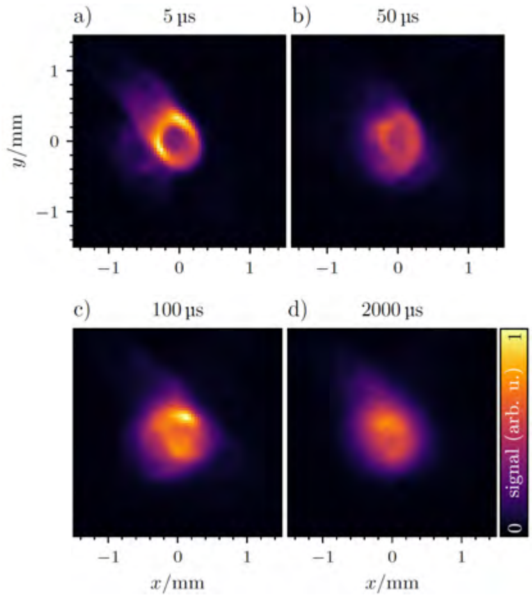

Figure 2: Ion density distributions in the radial plane after four different storage times, showing the transition from a narrow distribution of perturbed cyclotron radii (frame a) to a Gaussian distribution (frame d).

Due to careful adjustment of the ion optics' voltages, the ions are capture with a magnetron radius close to zero but non-zero reduced cyclotron radius ($\rho_+ \approx 200\,\mu\mathrm{m}$) as depicted in 2a. The ion distribution in the trap evolves from an initially ring-shaped distribution to a Gaussian distribution within about 2 ms (Figure 2d) [3]. Combining all information, one can calculate an ion density in the cloud's centre of about $1 \times 10^5\,\mathrm{mm^{-3}}$ which is sufficiently dense for high ion yield in the upcoming laser experiments at Jeti200 in Jena.

References

[1] M. Kiffer *et al.*, Phys. Rev. A **109**, 033102 (2024).

[2] M. Kiffer *et al.*, J. Appl. Phys. **136**, 184901 (2024).

[3] S. Ringleb *et al.*, J. Phys. B: At. Mol. Opt. Phys. **58**, 095202 (2025).

* stefan.ringleb@uni-jena.de

Studies of Highly Charged Ions with Electron Beam Ion Traps

S. Bernitt*[1,2] and R. Simon[1,2]

[1]*HI Jena, Fröbelstieg 3, 07743 Jena, Germany;* [2]*GSI Helmholtzzentrum für Schwerionenforschung GmbH, Planckstraße 1, 64291 Darmstadt, Germany*

An electron beam ion trap (EBIT) is a device that uses a quasi-monoenergetic electron beam to produce highly charged ions (HCI) be means of electron impact ionization and traps them in the beam's negative space-charge potential. Such devices offer opportunities to study HCI on a small-laboratory scale.

S-EBIT II is installed at the HITRAP slow-ion facility at GSI [1]. It will be used there as a local ion source, and also as a stand-alone experimental setup for spectroscopy on highly charged ions (HCI). As an ion source, it will serve multiple experiments connected to HITRAP. Its superconducting magnet facilitates the production of mid-Z HCI. During the first successful x-ray spectroscopy measurements with trapped highly charged argon ions, it became apparent that the original electron gun was not able to provide electron beam currents larger than 1 mA, which is insufficient for normal operation. Therefore, it was concluded that it is necessary to replace it with a new model. This will also resolve potential future problems due to non-availability of replacement parts. After investigating different options, guided by numerical beam simulations, it was decided to adapt an electron gun design which was developed for compact electron beam ion traps at the MPIK in Heidelberg. Using an existing design, which was shown to work well, reduces uncertainties. By now, most parts have been manufactured and were delivered. Partial test assemblies have taken place, and installation is planned in the first half of 2025. New control software has been developed to overcome limitations of the old system and facilitate rapid implementation of ion breeding cycles and complex ion extraction schemes. It will be deployed during re-commissioning of S-EBIT II after installation of the new electron gun. Furthermore, a series of dielectronic recombination experiments was planned and is currently being prepared. These aim at finding best operational parameters for as high as possible ion yields.

We also participated in two experimental campaigns with compact EBITs based on permanent magnets. One of them, PolarX-EBIT, has already been operational for a number of years and was originally developed in a cooperation of IOQ, MPIK, PTB, and HIJ. It was used for a high-precision spectroscopy experiment at beamline P04 of PETRA III, during which a unique combination of EBIT, synchrotron light source, and electron spectroscopy setup (see figure 1) was used to achieve unprecedented accuracy in the determination of transition energies in various high charge states of iron [2, 3]. This is part of efforts to provide high-quality atomic data for astrophysical plasma models, which are crucial for the interpretation of spectra observed with the newest generation of satellite x-ray observatories [4].

Another campaign took place at the European XFEL free-electron laser facility. The new SQS-EBIT, which is based on the PolarX-EBIT design, was used to perform a first-of-its-kind two-color x-ray pump-probe experiment. By varying the delay between a resonantly exciting first and a resonantly ionizing second pulse, and observing changes in ion charge state populations, it was possible to directly measure the lifetimes of excited states in various HCI, which decay via allowed electric dipole transitions in the x-ray regime, resulting in lifetimes on the order of 100 fs and below. Data analysis is still ongoing.

* s.bernitt@hi-jena.gsi.de

References

[1] H. J. Kluge *et al.*, Adv. Quantum Chem. **53**, 83 (2007).

[2] C. Shah *et al.*, ApJ **969**, 52 (2024).

[3] M. Togawa *et al.*, Phys. Rev. A **110**, L030802 (2024).

[4] S. Bernitt *et al.*, JINST **20**, C03030 (2025).

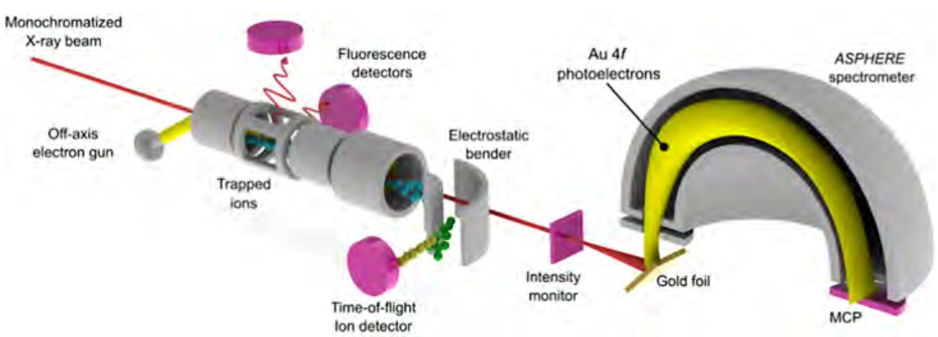

Figure 1: Experimental setup for high-precision x-ray spectroscopy experiments with PolarX-EBIT and the ASPHERE electron spectrometer [2]. Kinetic energies of photoelectrons are monitored to track changes in photon energy.

THEORY

Dark-field setup for the measurement of light-by-light scattering with high-intensity lasers

Fabian Schütze[1,2], Leonhard Doyle[3], Jörg Schreiber[3], Matt Zepf[1,4], and Felix Karbstein[*1,2]

[1] *Helmholtz Institute Jena, Germany;* [2] *Theoretisch-Physikalisches Institut, FSU Jena, Germany;* [3] *Ludwig-Maximilians-Universität München, Germany;* [4] *Institut für Optik und Quantenelektronik, FSU Jena, Germany*

We put forward a concrete experimental setup allowing to measure light-by-light scattering in the collision of two optical high-intensity laser beams at state-of-the-art high-field facilities operating petawatt class laser systems. Our setup uses the same focusing optics for both laser beams to be collided and employs a dark-field approach for the detection of the single-photon-level nonlinear quantum vacuum response in the presence of a large background. Based on an advanced modeling of the colliding laser fields, we in particular provide reliable estimates for the prospective numbers of signal photons scattered into the dark field for various laser polarizations.

Quantum fluctuations mediate effective couplings of macroscopic electromagnetic fields in vacuum [1]. These generically give rise to a signal component that may differ in characteristic properties such as propagation direction and polarization from the originally applied fields. Because these signals are very small, they could not yet be verified in a controlled laboratory experiment. However, recent advances in high-intensity laser technology have substantiated the perspectives of a first measurement of this effect with state-of-the-art technology in the near future. One of the key challenges is to achieve a sufficiently large signal-to-noise ratio allowing to measure the small quantum vacuum signal in the presence of the huge number of photons constituting the driving laser fields.

In Ref. [2] we put forward a specific setup allowing for its detection in an experiment based on the collision of two focused high-intensity laser pulses in a counter-propagating geometry. The basic idea of our setup is to use the same focusing optics for both pulses to be collided and to employ a dark-field approach for the detection of the induced single-photon-level signal. To this end two subsequent pulses generated by the same laser system and appropriately separated in time by means of a delay line are collided in their common focus after the propagation direction of the first pulse has been reversed at a spherical retro-reflector. Moreover, a central shadow is imprinted in the transverse profile of the initial beam by reflecting the initial beam off a mirror with hole. By construction this shadow is then present both in the converging beam prior to its focus and the diverging beam after its focus, while a peaked on-axis focus profile is retained [3]. The shadow in the diverging beam is effectively imaged onto a single-photon sensitive detector via a hole in the retro-reflector such as to spatially filter out a sizable fraction of the quantum vacuum signal induced in the collision of the two laser pulses. See Fig. 1 for an illustration. By appropriately preparing the polarization state of the incident beams prior to being fed into the focusing optics also polarization sensitive observables can be studied with our setup.

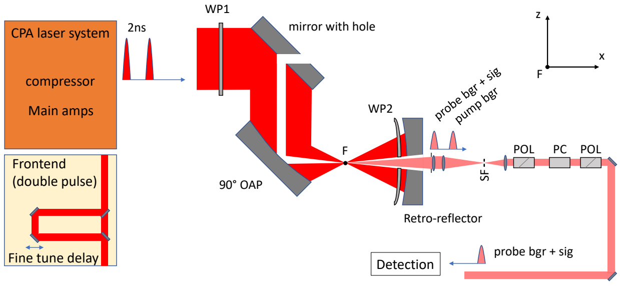

Figure 1: Schematic layout of the experimental setup. Two pulses generated by the same frontend are separated in time and fed into the same focusing optics such that they are collided in their common focus after the propagation direction of the first pulse has been reversed at a retro-reflector. A central shadow is imprinted in the transverse profile of the initial beam by reflecting it off a mirror with hole. The shadow is effectively imaged onto a single-photon sensitive detector via another hole in the retro-reflector such as to spatially filter out a sizable fraction of the quantum vacuum signal while minimizing the background.

Resorting to a set of well-justified assumptions and theoretical idealizations, in Ref. [2] we have explicitly demonstrated that the setup envisioned by us should indeed provide a prospective new route towards a first measurement of nonlinear quantum vacuum signals in an all-optical experiment at present and forthcoming petawatt-class high-intensity laser laboratories, such as CALA in Garching, Germany. As a critical next step, it needs to be shown that the scattering and diffraction background that is inevitable in any real-world experimental implementation of the setup can indeed be appropriately controlled and sufficiently suppressed in experiment.

This work has been funded by the DFG under Grant Nos. 416607684, 416702141 and 41670886 within the Research Unit FOR2783/2.

References

[1] W. Heisenberg and H. Euler, Z. Phys. **98**, 714 (1936).

[2] F. Schütze *et al.*, Phys. Rev. D **109**, 096009 (2024).

[3] F. Karbstein *et al.*, Phys. Rev. Lett. **129**, 061802 (2022).

* f.karbstein@hi-jena.gsi.de

Phase transition analogues in laser collisions with a dark-field setup

H. Gies*[1,2], F. Karbstein[1,2], and L. Maiwald[1,2]

[1] HI Jena, Fröbelstieg 3, 07743 Jena, Germany; [2] TPI, FSU Jena

Laser pulse collisions are a promising tool for the investigation of light-by-light scattering phenomena induced by quantum vacuum fluctuations. Using a numerical code based on the vacuum emission picture, we study laser pulse collisions observing a strong dependence of the signal features on the transverse pulse profiles. For an annular probe beam colliding with a counterpropagating pump beam, the signal's main emission direction can undergo the analogue of a phase transition with the beam waist ratio of the pulses serving as a control parameter. Depending on the pump's beam profile, this phase transition can be first or second order. Improving the code performance, we determine the critical point and extract the corresponding critical exponent for the second order transition.

Nonlinear interactions of electromagnetic fields in vacuum are a long-standing prediction of quantum electrodynamics (QED). For a precise and quantitative verification of these interactions, the collision of macroscopically controllable, ultra-intense laser pulses is a promising experimental pathway in many laboratories worldwide.

For the description of general beams and collision geometries, powerful numerical methods are needed. Our work relies on the VacEm code [1] based on the vacuum emission picture. We highlight and analyze a phenomenon reminiscent to a phase transition in statistical physics. In [2], we demonstrate that both its qualitative and quantitative properties depend sensitively on the beam properties such that the use of an accurate computational method is mandatory. More specifically, we use a probe beam with an annular far-field profile but a pronounced on-axis peak in the focus colliding head on with a strong pump pulse and study the angular distribution of quantum-induced signal photons. We confirm that the asymptotic signal can be peaked either in the direction of the beam axis or at a finite angular offset [3] depending on the relative beam waists of the colliding pulses and the transverse beam profiles.

Interestingly, our results can be phrased in the language of critical phenomena with the main emission direction of the signal serving as an order parameter that can undergo an apparent symmetry transition from on axis to off axis depending on the pump properties serving as control parameters. The analogy is quantified further by fitting the data to a power law as suggested by conventional critical phenomena. Using the fit model

$$\varphi_{\text{peak}}\big|_{\text{transition}} = C\left(\frac{w_{0,2}-w_{0,2,\text{c}}}{w_{0,1}}\right)^{\beta} + \frac{\pi}{2}, \qquad (1)$$

with parameters C, β, and $w_{0,2,\text{c}}$, we find for the critical exponent of the order parameter $\beta = 0.372 \pm 0.014$.

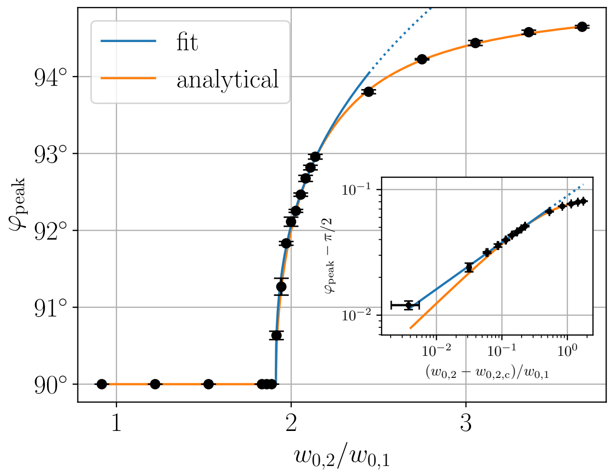

Figure 1: Peak direction of the signal photon distribution for an annular flat-top probe colliding with a Gaussian pump vs. the pump-to-probe waist ratio $w_{0,2}/w_{0,1}$. Interpreting φ_{peak} as an order parameter, we observe a continuous second-order phase transition. The blue curve represents the power-law fit (1), the orange curve depicts an analytical estimate. The double-log plot in the inset confirms the critical behavior described by (1) with a critical exponent β.

For our PW-class laser parameters, cf. [2], we obtain a critical pump-to-probe beam waist ratio $(w_{0,2,\text{c}}/w_{0,1})\big|_{\text{g}} = 1.9121 \pm 0.0017$ which plays the role of the critical point.

As the computation of observables in the critical region requires a substantial numerical accuracy, we use the present investigation also as a motive to improve the VacEm code as well as study its convergence with critical discretization parameters. We observe that the accurate modeling of generic flat-top beam profiles poses a numerical challenge that is addressed by our code improvements [2]. More specifically, the improvements significantly reduce the computation time, memory, and storage demand. The extensive simulations of flat-top beams is thus made feasible in practice.

In summary, our work sets an example that the language of critical phenomena can be useful to describe and quantify quantum vacuum signatures in laser pulse collisions.

References

[1] A. Blinne *et al.*, Phys. Rev. D **99**, 016006 (2019).

[2] H. Gies, F. Karbstein and L. Maiwald, Phys. Rev. D **111**, 016027 (2025).

[3] F. Karbstein *et al.*, Phys. Rev. D **101**, 113002 (2020).

*holger.gies@uni-jena.de

quvac: exploring the virtual swamp of quantum vacuum

M. Valialshchikov*[1], F. Karbstein[1], and D. Seipt[1]

[1] HI Jena, Fröbelstieg 3, 07743 Jena, Germany

First experiments to observe photon-photon scattering with real on-shell photons are being planned and performed at the moment. To provide quantitative estimates for expected quantum vacuum signals, we wrote a new code "quvac" with special emphasis on clarity and sustainability. We plan to make it open source in the near future and hope that it will be useful to the light-by-light scattering community.

Strong-field QED predicts that in the presence of strong electromagnetic fields the quantum vacuum starts to behave like a medium and affect light propagation. For currently available technology the expected signals are typically weak (only a few photons) making it challenging to observe against huge laser background. Theoretical studies provided a lot of insights into promising configurations and qualitative estimates but they are limited to simplified beam profiles. Employing numerical Maxwell solver allows to model more realistic beam profiles and obtain quantitative estimates [1].

In the vacuum emission picture [2], the zero-to-single photon (with wavevector $\mathbf{k}$, energy $\omega = |\mathbf{k}|$ and polarization vector $\epsilon^{\mu}_{(p)}$) transition amplitude is given by

$$S_{(p)}(\mathbf{k}) = \frac{\epsilon^{*\mu}_{(p)}(k)}{\sqrt{2k^0}} \int d^4x \, e^{ik_\nu x^\nu} j_\mu(x) \Big|_{k^0=\omega}, \qquad (1)$$

where

$$j_\mu(x) = 2\partial^\nu \frac{\partial \mathcal{L}_{\text{HE}}}{\partial F^{\nu\mu}} \qquad (2)$$

is the signal-photon current generated by the external macroscopic electromagnetic fields $F^{\mu\nu}$ and $\mathcal{L}_{\text{HE}}$ is the Heisenberg-Euler Lagrangian.

We follow the same basic algorithm to calculate quantum vacuum signals [1]: 1) a linear Maxwell solver is used to describe the evolution of external electromagnetic fields, 2) the vacuum emission picture is used for the calculation of the quantum vacuum signals (Eq. 1).

Compared to the previous implementation, we improved the following aspects:

- To *extend physics case and remove some limitations*, we added the possibility to calculate channel-separated signals (linearized in the probe) and to use any combination of analytic and Maxwell-propagated fields. We also implemented several new field profiles.

- To *make the package more user-friendly and sustainable*, we have a git project page (including tutorials), a separate documentation webpage and also use modern packaging tools (testing, continuous integration).

*maksim.valialshchikov@uni-jena.de

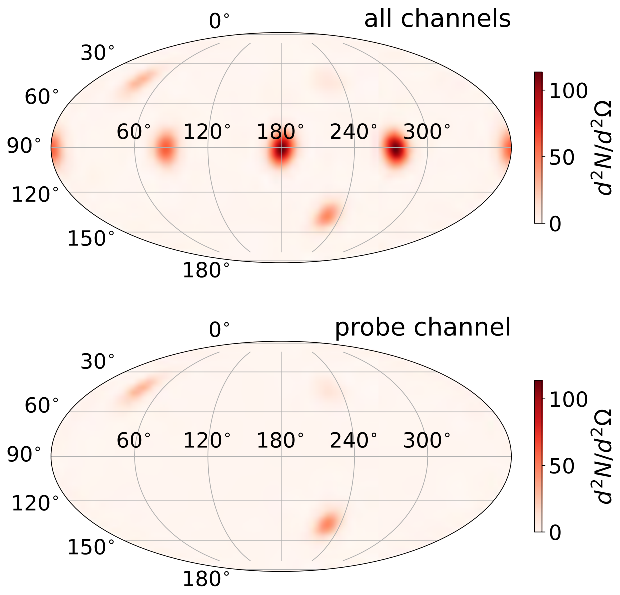

Figure 1: Angular signal photon spectrum from the collision of a focused probe ($W = 20$ J, $\lambda = 800$ nm, $\tau = 25$ fs FWHM, $w_0 = 1.6$ µm, $\theta_c = 45°$) with a belt pump [5], consisting of four focused beams ($W = 10$ J, $\theta_c = 90°, \phi = \{0°, 90°, 180°, 270°\}, \beta = \{0°, 90°, 90°, 0°\}$, other parameters are similar). (Top) Calculation including all channels; (Bottom) calculation with the amplitude linearized in probe field.

- *Better modularity and more utilities* allows for almost seamless implementation of grid scans and Bayesian optimization methods [3].

- For *faster computations* we added the possibility of lower precision calculations (float32) [4] and parallelization.

We benchmarked the code against analytical results and the previous implementation with satisfactory agreement.

Figure 1 shows the angular signal spectrum for the full vacuum emission amplitude and the one linearized in the probe field. When interference terms are negligible, such channel separation could give additional insights.

References

[1] A. Blinne *et al.*, Phys. Rev. D **99**, 016006 (2019).

[2] F. Karbstein *et al.*, Phys. Rev. D **91**, 113002 (2015).

[3] M. Valialshchikov *et al.*, Phys. Rev. D **110**, 076009 (2024).

[4] H. Gies *et al.*, Phys. Rev. D **111** 016027 (2025).

[5] S. S. Bulanov *et al.*, Phys. Rev. Lett. **104**, 220404 (2010).

Towards the full Heisenberg-Euler effective action at large N

Felix Karbstein*[1,2]

[1] Helmholtz Institute Jena, Germany; [2] Theoretisch-Physikalisches Institut, FSU Jena, Germany

We study the Heisenberg-Euler effective action in constant electromagnetic fields F for QED with N charged particle flavors of the same mass and charge e in the large N limit characterized by sending $N \to \infty$ while keeping $Ne^2 \sim eF \sim N^0$ fixed. This immediately implies that contributions that scale with inverse powers of N can be neglected and the resulting effective action scales linearly with N. Interestingly, due to the presence of one-particle reducible diagrams, even in this limit the Heisenberg-Euler effective action receives contributions of arbitrary loop order. In particular for electric- and magnetic-like field configurations we construct an explicit expression for the associated effective Lagrangian that, upon extremization for two constant scalar coefficients, allows to evaluate its full, all-order result at arbitrarily large field strengths.

In Ref. [1] we advocated the study of external-field quantum electrodynamics (QED) with N charged particle flavors of the same mass m and charge e in the large N limit. We emphasized that this deformation of standard QED constitutes a very interesting theoretical laboratory allowing to assess the impact of high-order loop corrections on the physics predictions of a quantum field theory under extreme conditions, and detailed the structure of the associated Heisenberg-Euler effective action $\Gamma_{\rm HE} = \int {\rm d}^4x\, \mathcal{L}_{\rm HE}$ governing the dynamics of prescribed macroscopic electromagnetic fields in the quantum vacuum [2]. The explicit results of that work mainly assumed the possibility of a perturbative expansion of $\Gamma_{\rm HE}$ in powers of the fine-structure constant $\alpha = e^2/(4\pi)$, or equivalently, the numbers of loops of its constituting Feynman diagrams.

In Ref. [3], we provide an explicit expression for the full constant-field Heisenberg-Euler effective Lagrangian $\mathcal{L}_{\rm HE}$ in the 't Hooft limit receiving contributions from arbitrary loop orders. Our starting point is the formal mean-field expression of $\Gamma_{\rm HE}$ for N-flavor QED,

$$\Gamma_{\rm HE}[A] = -\frac{1}{4}\int F_{\mu\nu}F^{\mu\nu} + S_\psi[A+j] - \frac{1}{2}\iint j_\mu (D^{-1})^{\mu\nu} j_\nu\,, \quad (1)$$

where $S_\psi[A] = -{\rm i}N \ln\det(-{\rm i}\not{D}[A]+m)$, $(D^{-1})^{\mu\nu}$ is the free inverse photon propagator and the auxiliary field j^μ is implicitly defined in terms of A^μ by the condition

$$\frac{\delta}{\delta j_\mu}\Gamma_{\rm HE}[A] = 0\,. \quad (2)$$

Presuming that both $N\alpha$ and eA^μ scale as $\sim N^0$, Eq. (1) neglects corrections of $\mathcal{O}(1/N)$. In the limit of $N \to \infty$ it thus becomes exact.

* f.karbstein@hi-jena.gsi.de

The formal expression for the effective action in Eq. (1) is a functional of the external field A^μ and an auxiliary, infrared divergent vector field j^μ. The latter is supposed to extremize this effective action and thus is implicitly also defined in terms of A^μ. In a first step, we analyzed the momentum structure of the vector field j^μ and showed that in generic constant fields it can be parameterized by four constant scalar coefficients π_p. Making use of this fact, the extremization of the effective action for j^μ can be traded for the much simpler extremization for these four scalars. We then demonstrated that upon introducing the field strength tensor of the auxiliary field $J^{\mu\nu} = \partial^\mu j^\nu - \partial^\nu j^\mu$, in constant fields the effective action (1) can be cast into a specifc form that is fully determined by the one-loop Lagrangian $\mathcal{L}_{\rm HE}^{\text{1-loop}}$ [2]. Using that in constant fields $\mathcal{L}_{\rm HE}^{\text{1-loop}}$ depends on $F^{\mu\nu}$ only via the scalar invariants of the field $\mathcal{F}$ and $\mathcal{G}$, further simplifications are possible and the associated full effective Lagrangian is given by $\mathcal{L}_{\rm HE}(\mathcal{F},\mathcal{G})$. By extremizing this Lagrangian for the four scalar coefficients π_p, its superficial dependence on these unknowns can be completely eliminated. Subsequently, we focused on the special case where $\mathcal{G} = 0$ and arrived at a rather compact expression for $\mathcal{L}_{\rm HE}(\mathcal{F})$. This effective Lagrangian is characterized by just two scalar unknowns ξ and χ to be eliminated by an extremization. As consistency checks, we explicitly demonstrated that our expression for $\mathcal{L}_{\rm HE}(\mathcal{F})$ correctly reproduces the all-order strong field limit studied in Ref. [1], and the perturbative result for $\mathcal{L}_{\rm HE}(\mathcal{F})$ up to $\mathcal{O}(\alpha^3)$.

As a natural continuation of Ref. [3], in the future we in particular plan to numerically extremize the effective Lagrangian $\mathcal{L}_{\rm HE}(\mathcal{F})$ for both scalars ξ and χ. This will allow us to study the fate of the full Heisenberg-Euler Lagrangian at large N as a function of $\mathcal{F}$ up to arbitrarily large values of this parameter. Because the Feynman diagrams that dominate the all-loop strong field limit [4] of standard $N = 1$ flavor QED are precisely those surviving in the large N limit of the theory, this study will also be relevant for the understanding of the strong-field behavior of standard external-field QED.

This work has been funded by the DFG under Grant No. 416607684 within the Research Unit FOR2783/2.

References

[1] F. Karbstein, JHEP **2022**, 57 (2022).

[2] W. Heisenberg and H. Euler, Z. Phys. **98**, 714 (1936).

[3] F. Karbstein, JHEP **2024**, 180 (2024).

[4] F. Karbstein, Phys. Rev. Lett. **122**, 211602 (2019).

Renormalization Flow of Nonlinear Electrodynamics

H. Gies*[1,2] and J. Schirrmeister[2]

[1]HI Jena, Fröbelstieg 3, 07743 Jena, Germany; [2]TPI, FSU Jena

We study the renormalization flow of generic actions of nonlinear electrodynamics. We search for RG fixed points or rather fixed functions, i.e., globally existing nonlinear Lagrangians. For proper initial conditions parametrized by the photon anomalous dimension, we construct a global fixed function for homogeneous magnetic fields of arbitrary strength. For the strong-field limit of the 1PI QED effective action, where the anomalous dimension is determined by electronic fluctuations, our result suggests the existence of a singularity free strong-field limit, circumventing the standard conclusions based on naive RG improvement arguments connected to the perturbative Landau pole.

Relativistic models of nonlinear electrodynamics have an extensive history in field theory, beginning with Born- or Born-Infeld theory motivated by the removal of the divergence the electron's self-energy in a classical setting. From QED and a suitable average over quantum fluctuations, Heisenberg-Euler theory arises as the presumably correct theory of the nonlinear response of the electrodynamic quantum vacuum, representing also a hallmark of the concept of effective field theory. Higher-order resummations together with RG-improvement arguments seem to suggest that the Landau-pole divergence at high momenta translates into an analogous divergence in field amplitudes [1].

In our work [2], we address the strong-field limit of Heisenberg-Euler-type theories using methods of functional renormalization. More specifically, we derive the general nonperturbative RG flow equation for action functionals depending on the gauge- and Lorentz-invariant combinations of the field strength. We find that the criterion of *global existence* of functions satisfying the fixed-point equation for the action is most relevant. Carefully imposing *proper* initial conditions makes it possible to construct globally existing fixed-point actions which are parametrized in terms of the anomalous dimension of the photonic field. The corresponding global action in the direction of one of the invariants is obtained by a nontrivial matching of the small- and large-field expansions, see Fig. 1. The approximations involved can be applied to the case of a purely magnetic field and thus provide evidence for the absence of Landau-pole-type singularities in the strong-field limit of this type.

The large-field asymptotics of our solution for the effective Lagrangian is characterized by [2]

$$\mathcal{L}(\mathscr{F}\to\infty)) \sim -\mathscr{F}^{\Delta(\eta)}, \quad \Delta(\eta) = \frac{4}{4+\eta}. \qquad (1)$$

Using the QED perturbative value $\eta = \frac{2}{3\pi}\alpha$ and expand-

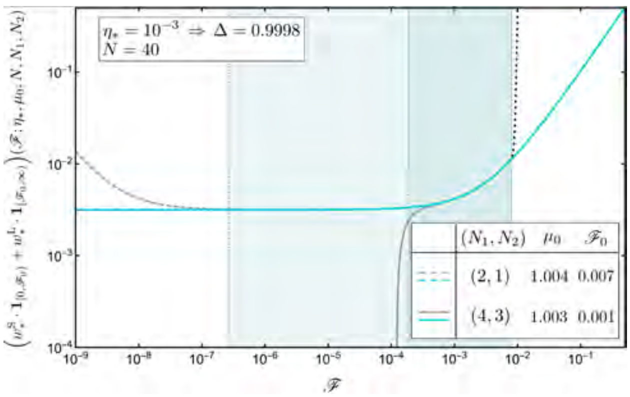

Figure 1: Global continuous fixed function and residuals of small- and large-field expansions as a function of the (dimensionless version of the) field strength invariant $\mathscr{F} = \frac{1}{4}F_{\mu\nu}F^{\mu\nu}$ for the photon anomalous dimension $\eta_* = 10^{-3}$. The large-field asymptotics is given by a power law with exponent $\Delta = \frac{4}{4+\eta_*}$. The small-field expansion in powers of $\mathscr{F}$ is truncated beyond the polynomial order $N = 40$, whereas the large-field truncation parameters (N_1, N_2) are taken to be either $(2, 1)$ (dashed) or $(4, 3)$ (solid) and specify a suitable Hahn series [2]. The parameters μ_0 and $\mathscr{F}_0$ control a smooth interpolation in the overlap region. Gray lines represent pure large-field solutions, black dotted lines the small-field solution. The existence of a smooth overlap indicated by the colored regions is a strong indication for the existence of a global solution.

ing in α, this result corresponds precisely to the strong magnetic field limit of the one-loop Heisenberg-Euler Lagrangian. Whereas conventional perturbative resummation techniques [1] of that result induce a Landau-pole singularity in the effective action at exponentially large field strength $\sqrt{\mathscr{F}} \sim m_e^2 e^{3\pi/\alpha}$, the asymptotic form suggested by Eq. (1) as well as our full global solutions are free of any singularity.

In summary, our nonperturbative construction suggests the existence of a regular effective action of nonlinear QED to arbitrarily high (magnetic) field strength amplitudes with the asymptotic limit being controlled by the photon anomalous dimension. We emphasize that our observation does not resolve the triviality problem of QED which – in our setting – would be linked to a high-energy divergence in η driven by charged-particle fluctuations.

References

[1] V. I. Ritus, Zh. Eksp. Teor. Fiz. **73**, 807 (1977).

[2] H. Gies and J. Schirrmeister, Phys. Rev. D **110**, 076010 (2024).

*holger.gies@uni-jena.de

Diagnostics of Spin-Polarized Ions at Storage Rings

Anna Maiorova*[1,2], Stephan Fritzsche[1,2,3], Andrey Surzhykov[4,5], and Thomas Stöhlker[1,2,6]

[1] *HI Jena, Fröbelstieg 3, 07743 Jena, Germany;* [2] *GSI,Darmstadt;* [3] *TPI, FSU Jena;* [4] *PTB, Braunschweig;* [5] *TU Braunschweig;* [6] *IOQ, FSU Jena*

Polarized heavy ions are a valuable research tool with a wide range of applications. Not only the production and preservation of ion polarization in storage rings, but also its measurement is an extremely important task. For this reason, we proposed the method of diagnostics of spin-polarized ions that can provide information about both the direction and the degree of their polarization.

We employ the radiative recombination (RR) of polarized electrons into the ground state of initially hydrogen-like, finally helium-like, ions as a probe for ion polarization. Radiative recombination is one of the dominant processes that occurs in ion-electron collisions. RR radiation is known to be very sensitive to the spin states of colliding particles [1]. This sensitivity can naturally be studied within the framework of density matrix theory [2]. Within this framework it is convenient to express the elements of density matrices of the incident free electron $\hat{\rho}_i^{(\mathrm{el})}$, characterized by an asymptotic linear momentum $\mathbf{p}$, and helicity m_s, and of the hydrogen–like ion $\hat{\rho}_i^{(\mathrm{ion})}$, being in a magnetic substate $|1s_{1/2}\,\mu_0\rangle$, in terms of the corresponding statistical tensors [2, 3]:

$$\left\langle \mathbf{p}m_s \left| \hat{\rho}_i^{(\mathrm{el})} \right| \mathbf{p}m_s' \right\rangle = \sum_{k=0,1} \sum_{q=-k}^{k} (-1)^{1/2-m_s'}\, C^{k\,q}_{1/2\,m_s,\,1/2\,-m_s'}\, \rho^{(\mathrm{el})}_{kq}\,,$$

$$\left\langle 1s_{1/2}\,\mu_0 \left| \hat{\rho}_i^{(\mathrm{ion})} \right| 1s_{1/2}\,\mu_0' \right\rangle = \sum_{K=0,1} \sum_{Q=-K}^{K} (-1)^{1/2-\mu_0'}\, C^{K\,Q}_{1/2\,\mu_0,\,1/2\,-\mu_0'}\, \rho^{(\mathrm{ion})}_{KQ}\,.$$

In addition to well-defined symmetry properties, a great advantage of the statistical tensors is their direct relation to the components $\left(P_x^{(\mathrm{el,ion})}, P_y^{(\mathrm{el,ion})}, P_z^{(\mathrm{el,ion})}\right)$ of electron and ion polarization vectors:

$$\begin{aligned} \rho_{00}^{(\mathrm{el,ion})} &= \frac{1}{\sqrt{2}}\,, \\ \rho_{10}^{(\mathrm{el,ion})} &= \frac{P_z^{(\mathrm{el,ion})}}{\sqrt{2}} \\ \rho_{1\pm1}^{(\mathrm{el,ion})} &= \mp\frac{1}{2}\left(P_x^{(\mathrm{el,ion})} \mp \mathrm{i}\, P_y^{(\mathrm{el,ion})}\right). \end{aligned}$$

Both polarization vectors $\mathbf{P}^{(\mathrm{ion})}$ and $\mathbf{P}^{(\mathrm{el})}$ are defined in the ion rest frame, where the z–axis is chosen along the momentum of the incident electron $\mathbf{p}$, and together with the x–axis defines the reaction plane. Moreover, the degree of polarization

$$P^{(\mathrm{el,ion})} = \sqrt{\left(P_x^{(\mathrm{el,ion})}\right)^2 + \left(P_y^{(\mathrm{el,ion})}\right)^2 + \left(P_z^{(\mathrm{el,ion})}\right)^2} \le 1$$

is equal to unity for a completely polarized beam, and $P^{(\mathrm{el,ion})} < 1$ if electrons or ions are partially polarized.

We considered the cross section of the radiative recombination, integrated over the photon emission angles and summed over its polarization. It was found that this integrated cross section depends on the polarization of both the initial ion and the incident electron:

$$\sigma_{\mathrm{RR}} = \sigma_{\mathrm{RR}}^{(\mathrm{unp})} + \sum_{i=x,y,z} P_i^{(\mathrm{el})} P_i^{(\mathrm{ion})} \Delta\sigma_{\mathrm{RR}}^{(\mathrm{i})}\,. \qquad (1)$$

Here, $\sigma_{\mathrm{RR}}^{(\mathrm{unp})}$ is the total cross section for the radiative recombination of unpolarized electrons and ions, and cross section corrections $\Delta\sigma^{(\mathrm{x,y,z})}$ depend on the incident electron energy and the nuclear charge of the ion.

As seen from Eq. (1), the integrated RR cross section contains the term $\sigma_{\mathrm{RR}}^{(\mathrm{unp})}$ that is completely independent of the ion and electron polarization, and a sum of terms proportional to the product of the polarization components $P_i^{(\mathrm{el})} P_i^{(\mathrm{ion})}$. Our theoretical study clearly demonstrates that this cross section is highly sensitive to the mutual orientation of the electron and the ion polarization vectors. We argue, therefore, that cross section measurements can provide information about both the direction and the degree of ion polarization. Such "spin tomography" of stored hydrogen–like ions is of paramount importance for planned experimental activities at GSI and FAIR facilities, aimed at searching for new physics beyond the Standard Model.

References

[1] A. Surzhykov *et al.*, Phys. Rev. Lett. **94**, 203202 (2005).

[2] V. V. Balashov *et al.*, Polarization and Correlation Phenomena in Atomic Collisions, (Kluwer Academic/Plenum, New York, 2000).

[3] K. Blum, Density matrix theory and applications; 3rd ed. (Springer: Berlin, 2012)

* a.maiorova@gsi.de

Nonlinear Breit-Wheeler pair production using polarized photons from inverse Compton scattering

D. Seipt*[1], M. Samuelsson[2], and T. Blackburn[2]

[1]HI Jena, Fröbelstieg 3, 07743 Jena, Germany; [2]Department of Physics, University of Gothenburg, Sweden

Observing multiphoton electron-positron pair production via the nonlinear Breit-Wheeler (NBW) process requires high-energy γ rays to interact with strong electromagnetic fields. The polarization dependence of NBW was predicted already in the seminal papers in the 1960, but hitherto remains unobserved. Here we report on detailed Monte Carlo simulations of an experimental configuration that accomplishes this by employing a two-stage set-up. First, a multi-GeV electron beam interacts with a moderately intense laser pulse to produce a bright, highly polarized beam of γ rays via inverse Compton scattering. Second, after removing the primary electrons, these γ rays collide with another, more intense, laser pulse in order to produce the e^+e^--pairs.

The schematic of this two-stage set-up is depicted in Fig. 1. A laser pulse with polarization E_1 collides with an electron beam to create γ rays via inverse Compton scattering, which are predominantly polarised along E_1. After travelling along the baseline of several meters, the γ rays collide with the second laser pulse, which is polarized along E_2 (at a pitch angle θ relative to E_1), and electron-positron pairs are created via the NBW process. By varying θ we can go from $\parallel$ ($\theta = 0$) to $\perp$ ($\theta = \pi/2$) polarized pair production channels.

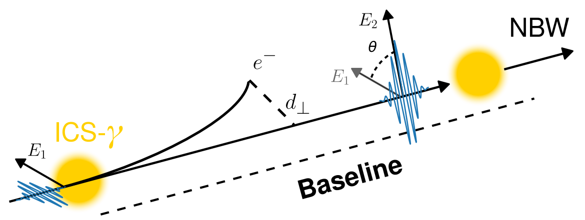

Figure 1: Schematic of the two-stage NBW set-up.

To study the feasibility of such two-stage experiments we have performed detailed Monte Carlo simulations of both the production of polarized γ rays via linear ICS [2] and NBW pair production from polarized photons [3]. We have investigated in detail 3 different scenarios with primary electron energies between 16.5 GeV and 200 GeV. For detailed simulation parameters we refer to Ref. [1]. Here we report in some detail the results for 16.5 GeV which could be realized at LUXE [4].

Our simulations for stage 1 predict a mean photon energy of about 8 GeV at the center of the strong-field IP, with a root-mean-square (rms) bandwidth of approximately 0.5 GeV, see Fig. 2(a). The central part of the γ-ray beam has a photon fluence of 40 photons/µm^2 per bunch crossing (BX). Fig. 2(b) depicts the orientation and magnitude of the polarization. The photons are highly linearly polarized approximately along the x-axis with a polarization degree $S \approx 77$ %. This value was calculated by averaging over all macro-photons in a circular spot of radius 4 µm at the IP.

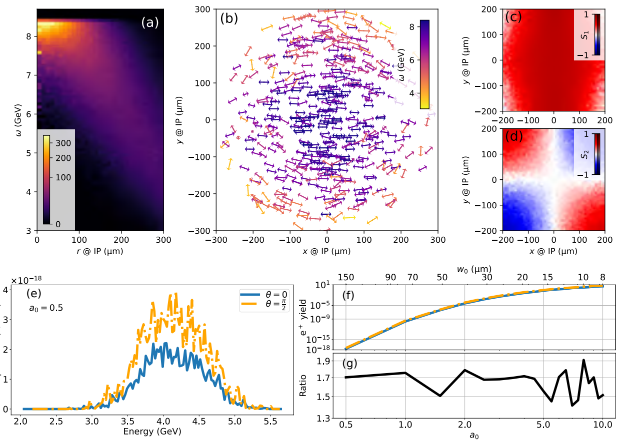

Figure 2: Simulation results for the γ-ray beam at the strong-field IP (a-d) and of the produced positrons (e-g).

The energy spectrum of the positrons produced when ICS-γ rays collide with a laser of $a_0 = 0.5$ is shown in Fig. 2(e). Changing the pitch angle θ from 0 to $\pi/2$ increases the positron yield without changing the shape of the spectrum, which is mostly symmetric in both cases. In Fig. 2(f), the total number of positrons is shown as a function of a_0, while keeping the total laser energy constant. Positron yields of up to 3.8–5.8 per BX are achieved for $a_0 = 10$. In Fig. 2(g) we show the ratio between the yields at $\theta = 0$ and $\pi/2$. It is mostly constant over the entire range of a_0, with an average value of 1.7. This difference would be observable at LUXE, given the expected precision, statistics, and sustained operation that are planned [4].

In summary, the high degree of linear polarization provided by ICS enables the polarization dependence of NBW to be studied in detail in a SFQED experiment located at a linear collider.

The data are available at `10.5281/zenodo.14139805`.

References

[1] D. Seipt *et al.*, PPCF **67**, 035002 (2025).

[2] PICA v1.2.9, DOI: `10.5281/zenodo.14044702`.

[3] Ptarmigan v1.4.1, DOI: `10.5281/zenodo.14040144`.

[4] H. Abramowicz *et al.*, EPJ-ST **230**, 2445 (2021).

*`d.seipt@hi-jena.gsi.de`

Extended locally monochromatic approximations of SFQED processes

N. Larin*[1] and D. Seipt[1]

[1] HI Jena, Fröbelstieg 3, 07743 Jena, Germany

We address the locally monochromatic approximation (LMA), which is a fundamental tool in the simulations of laser-particle collisions. We revisit the derivation of the LMA and propose a new, consistent method for obtaining LMA probability rates for arbitrary polarizations of a plane wave background. Also, we include bandwidth effects that are absent in the LMA. We refer to the bandwidth-restored LMA as LMA$^+$, and compare it with exact strong-field QED calculations and the locally constant field approximation.

Under the extreme conditions that take place in the collisions of high-intensity laser pulses with ultrarelativistic electron beams, processes of strong-field QED (SFQED), such as nonlinear Compton scattering (NCS) and nonlinear Breit-Wheeler pair production, play a significant role [1]. For the upcoming experiments [2], one requires reliable simulation routines that account for the SFQED effects. In the transition regime of laser intensities ($a_0 \sim 1$), these simulations are based on the probability rate in the locally monochromatic approximation (LMA) [3].

In contrast to the only previously known locally constant field approximation (LCFA) [1], which works for $a_0 \gg 1$, the LMA is applicable for arbitrary intensities. However, it is not so versatile as LCFA and requires the electromagnetic background to be close to a plane wave and to possess two time scales: slow envelope and fast carrier.

The key idea behind the LMA derivation is the splitting of the particle's trajectory into the slow ponderomotive drift of the guiding center and the fast quiver motion around it. But the mere separation of time scales is insufficient, since it leaves us with the altering in sign quantity, which we refer to as proto-rate $\mathcal{R}(\varphi)$ [4]. The second essential step is to perform cycle-averaging of the proto-rate over the fast varying carrier component, to turn it into the positive-definite probability rate [4]

$$\mathbb{R}_{\mathrm{LMA}}(\varphi) \equiv \frac{1}{2\pi} \int\limits_{\varphi-\pi}^{\varphi+\pi} \mathcal{R}(\varphi')\, d\varphi'. \tag{1}$$

Notably, the cycle-averaging procedure was always implied, but has never been implemented explicitly until recently [4].

We emphasize that our approach to the derivation of LMA allows us to obtain the probability rates consistently for arbitrary polarizations of a background plane wave. Whereas, the probability rates take forms of the corresponding rates in the infinite plane wave limit [4], with the substitution $a_0 \to a(\varphi/\Delta) \equiv a_0 g(\varphi/\Delta)$, where $g(\varphi/\Delta)$ is a pulse envelope and $\Delta \gg 1$ is its duration.

*nikita.larin@uni-jena.de

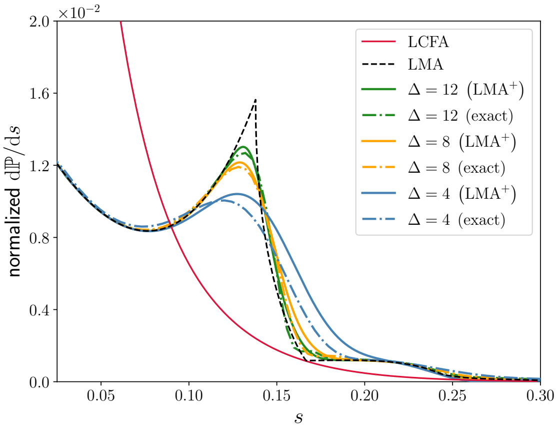

Figure 1: Energy spectra of NCS for circular polarization, plotted for $a_0 = 0.5$ and various pulse durations. Each curve is normalized by the total pulse duration Δ.

In the regime of moderate intensities ($a_0 \sim 1$), the emitted spectrum exhibits harmonic structure and LMA is able to reproduce it. However, the LMA predictions lack the features associated with the finite duration of a plane wave background. To account for the finite bandwidth, we have to include interference effects on the entire pulse scale. We achieve it by introducing the window function in the definition of proto-rate. Such bandwidth-restored LMA we call LMA$^+$. Since the window function and its width may be arbitrary, we specify them by matching LMA$^+$ and full SFQED results in the weak field limit ($a_0 \ll 1$).

In Fig. 1 we compare the emission spectra of NCS in a circularly polarized background [1], obtained by means of the standard LMA, LMA$^+$ and exact SFQED calculations. The envelope is chosen as $\exp\left(-\varphi^2/2\Delta^2\right)$. The LMA lacks the finite bandwidth features, like broadening of the harmonics and damping of the maximum harmonic's magnitude. In turn, the LMA$^+$ reproduces these features and provides reasonable results even for the regime $\Delta \sim 1$, where a separation of time scales is not valid anymore. We also added the LCFA result, to demonstrate that for the moderate intensity regime $a_0 \sim 1$ its predictions are much worse than both LMA and LMA$^+$, as expected.

References

[1] A. Fedotov *et al.*, Phys. Rep. **1010**, 1 (2023).

[2] H. Abramowicz *et al.*, Eur. Phys. J. Spec. Top. **230**, 2445 (2021)

[3] T. Heinzl *et al.*, Phys. Rev. A **102**, 063110 (2020).

[4] N. Larin and D. Seipt, arXiv:2506.04889 (2025).

Interaction of a Poincaré beam with optically polarized atoms immersed in constant magnetic field

S. Ramakrishna*[1,2] and S. Fritzsche[1,2]

[1] *HI Jena, Fröbelstieg 3, 07743 Jena, Germany;* [2] *TPI, FSU Jena*

We present a theoretical investigation of a Poincaré beam interacting with optically polarized atoms in the presence of magnetic field. In particular, we consider a linearly polarized plane wave as the pump and a Poincaré beam as the probe field interacting with rubidium atoms. The study of this interaction reveals that the absorption profile of the Poincaré beam is *axially-asymmetric* and this asymmetry depends on: (a) mutual orientation of the pump and probe light propagation directions relative to the quantization axis, and (b) on the strength of the constant magnetic field. To illustrate our results, we assume the incoming radiation drives an electric dipole transition, $5s\,^2S_{1/2}\,(F=1) \rightarrow 5p\,^2P_{3/2}\,(F=0)$, in rubidium atoms. These results, we believe will be beneficial for planning future experiments on atomic magnetometers based on structured light-atom interaction.

Recent works [1, 2] have established the advantages of vector-light-based atomic magnetometers in retrieving magnetic field information by observing the *symmetrical* absorption profile of vector light. In this work [3], we consider a dual beam set-up, where linearly polarized Gaussian beam is pump and Poincaré beam is probe light field that interacts with rubidium atoms driving an electric dipole transition $5s\,^2S_{1/2}\,(F=1) \rightarrow 5p\,^2P_{3/2}\,(F=0)$. To analyze this interaction process, we describe the atomic system by density matrix and obtain the population of the excited atomic state by solving Liouville-von Neumann equation in steady-state regime. This population of the excited state across the Poincaré beam's cross-section then directly translates into the absorption profile.

In the beginning, the Poincaré beam is assumed to propagate along the quantization axis and solely interacts with the unpolarized atoms, meaning the pump light field is turned off. In this simplified scenario, the three magnetic sublevels in the ground state of the rubidium atomic target will be equally populated. For this case, we find that the atoms located in the upper part of the beam cross-section interacts strongly with the Poincaré beam, and those in the bottom half are less interactive. This asymmetry in the interaction process stems from the fact that the Poincaré beam has an inhomogeneous polarization profile, see Fig. 1 (a). Specifically, the Poincaré beam's local polarization is purely circular at the beam center. As one moves away from the center, the light field's polarization changes to elliptical with varying ellipticity parameter. For example, atoms located at $b = 200\,\mu m$ experiences an elliptically polarized light and this field couples all the three magnetic sublevels in the ground state with the excited state. Among these, we observe the local transition amplitude for the transition $M_g = 0 \rightarrow M_e = 0$ ($\Delta M = 0$) is not symmetric across the beam cross-section. Particularly, the transition amplitude for this transition has lower values in the bottom part of the beam cross-section, as shown in the polar plot of the absolute value of transition amplitude Fig. 1 (b). Thus, for this case the absorption profile of Poincaré beam is *axially-asymmetric*, unlike in the case of vector light, see Fig. 1 (c). Whereas, when we consider the polarized case, the absorption profile is symmetric, see Fig. 1 (d). Because here the pump light propagates perpendicular to the quantization axis and thus drives the transition $M_g = 0 \rightarrow M_e = 0$ and pumping all the ground state population to sublevels $M_g = \pm 1$. Thus, the incoming probe light field cannot drive $\Delta M = 0$ transition, which is the fundamental reason for the observed asymmetry in the absorption profile.

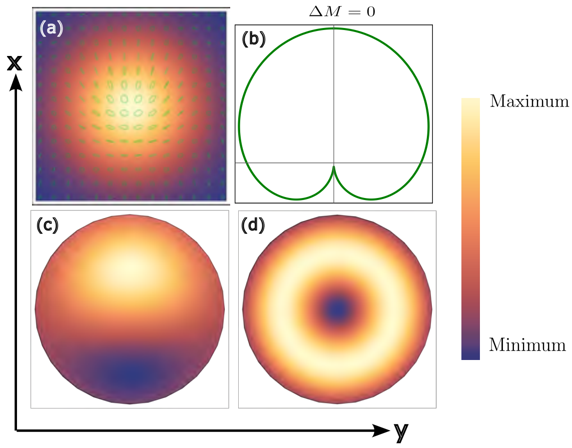

Figure 1: (a) Intensity and polarization profile of Poincaré beam. (b) Polar plot of the absolute value of transition amplitude for $M_g = 0 \rightarrow M_e = 0$. Absorption profile for Poincaré beam interacting with (c) unpolarized, and (d) polarized Rb atoms. The strength of the magnetic field is 1 G.

We believe our results can be useful in guiding the future experiments of optically pumped atomic magnetometers utilizing structured light modes.

The authors acknowledge funding from research School of Advanced Photon Science of the HI Jena.

References

[1] F. Castellucci *et al.*, Phys. Rev. Lett. **127**, 233202 (2021).

[2] S. Ramakrishna *et al.*, Phys. Rev. A. **10**, 84 (2024).

[3] S. Ramakrishna and S. Fritzsche, arxiv 2503.18927 (2025).

* shreyas.ramakrishna@uni-jena.de

Photoionization dynamics in intense few-cycle twisted laser pulses

D. F. Dar*[1,2,3], A. Weber[4], S. Ramarishna[1,2,3], and S. Fritzsche[1,2,3]

[1] *HI Jena, Germany;* [2] *TPI, FSU Jena;* [3] *GSI, Darmstadt;* [4] *King's College London*

Photoelectrons from photoionization reveal key details about light-atom interactions. While conventional lasers are well-studied, structured light fields like twisted Bessel beams, carrying orbital angular momentum, remain less understood. Prior work shows spectral shifts in above-threshold ionization with changes in the beam's opening angle and orbital angular momentum, but their precise impact on photoelectron momentum distributions (PMDs) is unclear. Using the strong field approximation and saddle point method, we analytically derive the ionization amplitude, modeling the atom with a hydrogenic 1s orbital (adjusted for krypton) for computational efficiency. This allows us to resolve how both parameters shape the PMD.

Previous studies, such as Böning et al. [1], have shown that photoelectrons can be emitted along the propagation direction of a Bessel pulse, with the above-threshold ionization (ATI) peak intensities governed by the beam's opening angle and total angular momentum (including its projection). While this finding advanced the understanding of structured light-matter interactions, the fine-scale variations in ATI peaks—such as their sensitivity to changes in the opening angle or orbital angular momentum (OAM)—were not explored. Moreover, earlier analyses relied heavily on computationally expensive numerical simulations, which, despite their accuracy, hinder intuitive insights into parameter dependencies. To overcome this limitation, we employ the saddle point method (SPM), a semi-analytical approach that efficiently identifies dominant contributions to the ionization dynamics. This allows us to systematically dissect how the Bessel pulse's opening angle and OAM shape the photoelectron momentum distribution (PMD) while balancing rigor with computational tractability.

We investigate [2] the impact of intense few-cycle Bessel pulses on photoelectron momentum distributions using the strong-field approximation combined with the saddle point method (Fig. 1). Our analytical approach accounts for the Coulomb singularity in hydrogenic $1s$ states by modifying the SPM near saddle points, where the dipole matrix elements diverge. While this method is tailored for hydrogen-like systems, extending it to more complex targets would require additional modifications to handle both the singularity and wavefunction structure.

This work has been funded by the Research School of Advanced Photon Science of HI Jena, Germany.

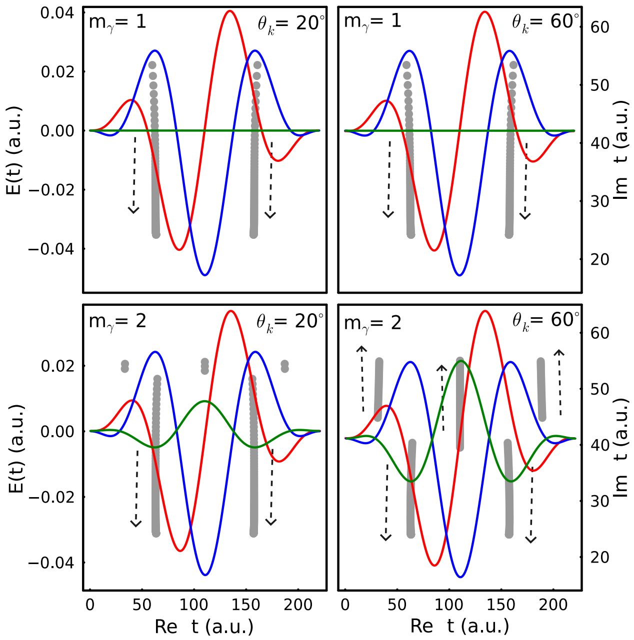

Figure 1: Electric field components of a two-cycle Bessel pulse with saddle-point solutions (gray circles) for a laser intensity of 5×10^{13} W/cm^2 and ϵ_p ranging from $0 \le \epsilon_p \le 20\omega$. The colored lines represent the electric field components: red for E_x, blue for E_y, and green for E_z. The TAM values $m_\gamma = 1, 2$ are shown from left to right, with a fixed opening angle $\theta_k = 20°$ and $60°$. θ_p and φ_p are kept constant at $90°$ and $0°$ respectively. Black dashed arrow-headed lines indicate the direction of the saddle point with increasing kinetic energy of the photoelectrons.

References

[1] B. Böning, W. Paufler, and S. Fritzsche, *"Above-threshold ionization by few-cycle Bessel pulses carrying orbital angular momentum"*, Phys. Rev. A **98**, 023407 (2018). doi:10.1103/PhysRevA.98.023407

[2] D. F. Dar, A. Weber, S. Ramakrishna, and S. Fritzsche, *"Photoionization dynamics in intense few-cycle twisted laser pulses"*, Phys. Rev. A **111**, 053113 (2025). doi:10.1103/PhysRevA.111.053113

* danish.dar@uni-jena.de

High-dimensional maximally entangled photon pairs in orbital angular momentum from parametric down-conversion

R. Bernecker*[1,2], B. Baghdasaryan[3], and S. Fritzsche[1,2]

[1] *HI Jena;* [2] *TPI, FSU Jena;* [3] *IAP, FSU Jena*

Photon pairs generated via spontaneous parametric down-conversion (SPDC) intrinsically possess high-dimensional entanglement in orbital angular momentum (OAM), offering promising features for future applications such as enhanced capacity and security in quantum communication protocols. However, the experimental generation of high-dimensional maximally entangled states (MESs) within a desired OAM subspace remains challenging. We calculate the joint conditions for the pump beam and the nonlinear crystal profile required for the direct generation of MESs, without the need for subsequent post-selection.

Maximally entangled states (MESs) are an important class of bipartite states exhibiting perfect quantum correlations. Well-known examples for two entangled qubits (with dimensionality $d = 2$) are the four Bell states. High-dimensional entanglement can be quantified by the Schmidt number K, where MESs of two d-dimensional entagled systems are characterized by $K_{d\times d} = d$.

Unlike polarization modes (limited to $d = 2$), orbital angular momentum (OAM) modes span an unbounded Hilbert space, where a photon carries OAM of $\ell\hbar$ with $\ell \in \mathbb{Z}$. In the paraxial and narrowband approximation, the spatial two-photon state from SPDC is given by

$$|\psi\rangle = \sum_{\ell_\mathrm{s},\ell_\mathrm{i}=-\infty}^{\infty} C^{\ell_\mathrm{s},\ell_\mathrm{i}}\, |\ell_\mathrm{s}\rangle \otimes |\ell_\mathrm{i}\rangle\,, \tag{1}$$

*richard.bernecker@uni-jena.de

where $C^{\ell_\mathrm{s},\ell_\mathrm{i}}$ is the OAM expansion amplitude of the photon pair, consisting of signal and idler, carrying ℓ_s and ℓ_i OAM, respectively. Desirable MESs from Eq. (1) can be realized by post-selection, i.e. filter out unwanted OAM modes from the subspace, but this reduces the photon yield and requires much experimental effort [3].

The amplitudes $C^{\ell_\mathrm{s},\ell_\mathrm{i}}$ depend on the pump beam's spatial profile [1], especially its OAM ℓ_p, and how the phase-matching condition in the nonlinear crystal is realized. By employing a non-trivial poling configuration $\chi^{(2)}(z)$ [2], we can modify a customized phase-matching function

$$\Phi_\mathrm{PM}(\Delta k_z) = \int_{-L/2}^{L/2} \chi^{(2)}(z)\, e^{i\Delta k_z z} dz, \tag{2}$$

where L is the crystal length aligned along the z-axis and Δk_z the phase mismatch. Combined with optimal chosen superposition of OAM modes for the pump, this enables direct generation of MESs in desired OAM subspaces. In [4], we show how to obtain suitable configuration for the pump beam and the crystal and demonstrate our method with maximally entangled qutrits ($d = 3$) and ququints ($d = 5$), see Fig. 1.

References

[1] E. V. Kovlakov *et al.*, Phys. Rev. A **128**, 060301(R) (2018).

[2] A. Dosseva *et al.*, Phys. Rev. A **93**, 013801 (2016).

[3] A. C. Dada *et al.*, Nature Physics **7** (9), 677-680 (2011).

[4] R. Bernecker *et al.*, Phys. Rev. A **110**, 033718 (2024).

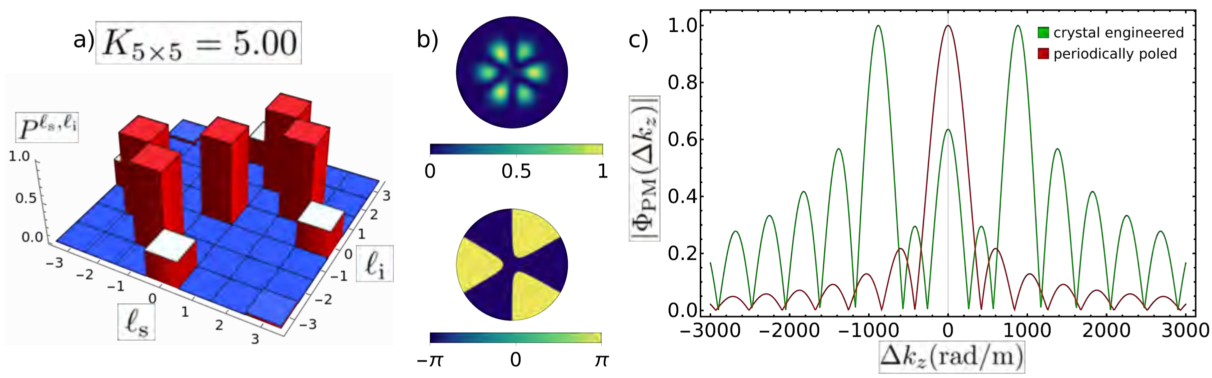

Figure 1: Example of a maximally entangled two-ququint state (d = 5). (a) The normalized OAM spectrum for the target state $|\psi\rangle = \frac{1}{\sqrt{5}}\big(|-2,-1\rangle + |-1,-2\rangle + |0,0\rangle + |1,2\rangle + |2,1\rangle\big)$ within the range $\ell_s, \ell_i = -3, ..., 3$. The state is maximally entangled in the subspace $\ell_s, \ell_i = -2, ..., 2$. (b) The required spatial profile of the pump beam consists of an unequal weighted superposition of modes carrying OAM of $\ell_\mathrm{p} = -3, 0$ and 3. (c) The required PMF Φ_PM (green line) and, for comparison, a typical sinc-like PMF of a periodically poled crystal (red line) of a lenght $L = 10$ mm.

Calculations of energies and g factors in highly charged Ca^{14+} ion

Andrey I. Bondarev*[1,2], Charles Cheung[3], Sergey G. Porsev[3], and Marianna S. Safronova[3]

[1] *Helmholtz Institute Jena, Germany;* [2] *GSI Helmholtzzentrum für Schwerionenforschung, Darmstadt, Germany;* [3] *University of Delaware, Newark, USA*

We calculated the energy levels and g factors of the excited states in Ca^{14+} ion to support the corresponding measurements [1]. The calculations are performed using a large-scale configuration interaction method to correlate all six electrons. We found an unexpectedly large contribution of the frequency-dependent Breit interaction corrections to the energy levels and good agreement with the experimental results. Comparison of the calculated g factor of the excited $^3P_1$ state with the measured value demonstrates the significance of the negative-energy states contribution and QED effects on magnetic moments.

Highly charged ions (HCI) have extreme electronic properties as a result of strong internal electric fields, allowing precise tests of fundamental physics [2]. Measurements of atomic parameters of these few-electron HCI are of interest, because theory predictions can reach accuracies far beyond what is possible in many-electron systems. In addition, quantum electrodynamics (QED) effects are greatly enhanced due to the high charge state, allowing stringent tests of QED in the strong-field regime. Furthermore, the response of the atomic structure to a magnetic field can be both calculated and measured with high accuracy.

Comparisons to the measured atomic parameters require the calculation of transition energies as an essential quality test of the wave functions used to compute, for instance, g factors. The calculations are performed using a large-scale configuration interaction (CI) method to correlate all six electrons in Ca^{14+} [3]. We converge the CI computation, including excitations up to $24spdfghi$ and extrapolating contributions of higher partial waves. The results of the computations are listed in Table 1. We find an unexpectedly large contribution of the frequency-dependent Breit interaction corrections, which is listed separately in the table. The resulting theoretical energy values are in excellent agreement with the experimental values, as shown in Table 1.

Table 1: Theoretical energies (in cm^{-1}) of $2s^22p^2$ states in Ca^{14+} are given relative to the $^3P_0$ ground state energy. Contributions of frequency-dependent Breit and QED are given in columns 'freq.' and 'QED', and the differences between the final energies with the NIST and Ref. [4] data are given in columns Δ^a and Δ^b, respectively.

Level	CI	freq.	QED	Final	Δ^a	Δ^b
$^3P_1$	17507	-10	60	17557	-2	1
$^3P_2$	35839	-17	99	35921	-2	9
$^1D_2$	108555	-18	111	108648	48	
$^1S_0$	197726	-21	52	197757	87	

We isolated the contribution of the Breit interaction to the energies in Table 2, where we list contributions from the frequency-independent Breit interaction ('Breit') and the frequency-dependent correction ('freq.') to the Coulomb energies ('Coulomb'). We find that the Breit corrections are very large, a few percent of the total excitation energies. This is due to large cancellations in the total energies of the ground and excited states, leading to optical transitions between them. We note that such a large Breit interaction is common for the HCI of interest in the development of high-precision atomic clocks. Our calculations show that frequency-dependent Breit contributes at the level of 1% of the Breit interaction, enabling us to estimate in which cases frequency-dependent Breit should be computed to achieve the expected accuracy in future HCI computations.

Table 2: Contributions (in cm^{-1}) to the energies of $2s^22p^2$ states in Ca^{14+} relative to the $^3P_0$ ground state energies (see text for notations). Last column shows the 'freq.' to 'Breit' ratio.

Level	Coulomb	Breit	freq.	ratio %
$^3P_1$	18323	-823	-10	1.2%
$^3P_2$	38187	-2347	-17	0.7%
$^1D_2$	110971	-2249	-18	0.8%
$^1S_0$	199236	-1337	-21	1.6%

The theoretical result for the g factor of the $^3P_1$ state, $g^{(\mathrm{theo})} = 1.49902$, is in good agreement with the experimental value $g = 1.499032(6)$. We emphasize that the contributions from negative-energy eigenstates (-0.00009) and QED corrections to the atomic magnetic moment (0.00116) are critical to achieve agreement (see [1] for details). Further g-factor calculations should include the rigorous QED treatment and nuclear recoil corrections.

References

[1] L. J. Spieß *et al.*, Phys. Rev. Lett. *accepted* (2025) arXiv:2502.18926.

[2] M. G. Kozlov, M. S. Safronova, J. R. Crespo López-Urrutia, and P. O. Schmidt, Rev. Mod. Phys. **90**, 045005 (2018).

[3] C. Cheung, M. G. Kozlov, S. G. Porsev, M. S. Safronova, I. I. Tupitsyn, and A. I. Bondarev, Comput. Phys. Commun. **308**, 109463 (2025).

[4] N.-H. Rehbehn *et al.*, Phys. Rev. A, **103**, L040801 (2021).

* a.bondarev@hi-jena.gsi.de

PUBLICATIONS

L. I. Stoyanov, Y. Zhang, A. Dreischuh, and G. G. Paulus
Controllable beam break-up, spectral broadening, and coherent beam recombination using arrays of singular beams
Optics Express **32**, 48758 (2024)
10.1364/OE.539538

B. K. Russell, S. S. Bulanov, Q. Qian, C. Arran, T. G. Blackburn, S. V. Bulanov, G. M. Grittani, S. P. D. Mangles, C. P. Ridgers, D. Seipt, and A. G. R. Thomas
Measuring signatures in photon angular spectra to distinguish nonlinear Compton scattering models
Physical Review A **110**, 062822 (2024)
10.1103/PhysRevA.110.062822

R. Chakma, S. Fritzsche, K. Hauschild, and A. Lopez-Martens
GEANT4 atomic relaxation data for transfermium nuclei (Z=101–104)
Nuclear Instruments & Methods In Physics Research Section A-accelerators Spectrometers Detectors And Associated Equipment **1072**, 170144 (2024)
10.1016/j.nima.2024.170144

C. Cheung, M. G. Kozlov, S. G. Porsev, M. S. Safronova, I. I. Tupitsyn, and A. I. Bondarev
pCI: A parallel configuration interaction software package for high-precision atomic structure calculations
Computer Physics Communications **308**, 109463 (2024)
10.1016/j.cpc.2024.109463

V. Krasnov, I. Makhotkin, J. E. Scheerder, L. Loetgering, V. Soltwisch, P. A. W. van der Heide, and C. Fleischmann
Soft X-ray chemically sensitive ptychographic imaging of 3D nano-objects
Optics Express **32**, 43788 (2024)
10.1364/OE.535314

E. Escoto, F. Pressacco, Y. Jiang, S. Rajhans, N. Khodakovskiy, I. Hartl, M. Seidel, C. M. Heyl, and H. Tuennermann
Improved temporal characteristics for post-compressed pulses via application-tailored nonlinear polarization ellipse rotation
Optics Letters **49**, 6841 (2024)
10.1364/OL.539646

W. Wang, F. Zou, S. Fritzsche, and Y. Li
Isomeric Population Transfer of the ^{229}Th Nucleus via Hyperfine Electronic Bridge
Physical Review Letters **133**, 223001 (2024)
10.1103/PhysRevLett.133.223001

T. Mazza, T. Baumann, R. Boll, A. De Fanis, S. Dold, M. Ilchen, T. Mullins, Y. Ovcharenko, D. Rivas, B. Senfftleben, S. Usenko, I. Ismail, J. Bozek, M. Simon, S. Fritzsche, and M. Meyer
Resonant Raman Auger spectroscopy on transient core-excited Ne ions
Journal Of Physics B-Atomic Molecular And Optical Physics **57**, 225001 (2024)
`10.1088/1361-6455/ad6369`

J. Gilles, S. Fritzsche, L. J. Spiess, P. O. Schmidt, and A. Surzhykov
Quadratic Zeeman and electric quadrupole shifts in highly charged ions
Physical Review A **110**, 052812 (2024)
`10.1103/PhysRevA.110.052812`

M. Kiffer, S. Ringleb, Th. Stöhlker, and M. Vogel
Non-destructive characterization of individual particle bunches by a resistive-cooling measurement in a Penning trap
Journal Of Applied Physics **136**, 184901 (2024)
`10.1063/5.0228725`

R. Lötzsch, H. F. Beyer, L. Duval, U. Spillmann, D. Banas, P. Dergham, F. M. Kröger, J. Glorius, R. E. Grisenti, M. Guerra, A. Gumberidze, R. Hess, P.-M. Hillenbrand, P. Indelicato, P. Jagodzinski, E. Lamour, B. Lorentz, S. Litvinov, Y. A. Litvinov, J. Machado, N. Paul, G. G. Paulus, N. Petridis, J. P. Santos, M. Scheidel, R. S. Sidhu, M. Steck, S. Steydli, K. Szary, S. Trotsenko, I. Uschmann, G. Weber, Th. Stöhlker, and M. Trassinelli
Testing quantum electrodynamics in extreme fields using helium-like uranium
Nature **625**, 673 (2024)
`10.1038/s41586-023-06910-y`

A. K. Sahoo, S. Fritzsche, and L. Sharma
Computation of effective collision strengths for plasma applications using JAC
European Physical Journal Plus **139**, 986 (2024)
`10.1140/epjp/s13360-024-05747-2`

R. Wagner, M. Ilchen, N. Douguet, P. Schmidt, N. Wieland, C. Callegari, Z. Delk, A. Demidovich, G. De Ninno, M. Di Fraia, J. Hofbrucker, M. Manfredda, V. Music, O. Plekan, K. C. Prince, D. E. Rivas, M. Zangrando, A. N. Grum-Grzhimailo, K. Bartschat, and M. Meyer
Circular dichroism in multiphoton ionization of resonantly excited helium ions near channel closing
Scientific Reports **14**, 27232 (2024)
`10.1038/s41598-024-75459-1`

Y. Gao, P. Wang, B. Liu, S. Xu, S. Chen, Y. Shou, J. Liu, Z. Mei, Z. Cao, T. Xu, Z. Liu, Z. Pan, D. Kong, Z. Peng, Y. Liang, T. Song, X. Chen, Q. Wu, Y. Zhang, J. Zhao, W. Qi, Z. Deng, Y. Zhao, F. Wu, M. Zepf, R. Ramis, P. R. Bolton, X. Yan, W. Ma, and J. Schreiber
All-optical method for generating transient microstructured targets in laser ion acceleration
Physical Review Research **6**, L042031 (2024)
`10.1103/PhysRevResearch.6.L042031`

A. Eckey, A. Golub, F. C. Salgado, S. Villalba-Chavez, A. B. Voitkiv, M. Zepf, and C. Müller
Impact of laser focusing and radiation reaction on particle spectra from nonlinear Breit-Wheeler pair production in the nonperturbative regime
Physical Review A **110**, 043113 (2024)
`10.1103/PhysRevA.110.043113`

S. Malekmohamadi, M. Pergament, G. Kulcsar, M. Seidel, Y. Liu, M. Edelmann, M. Kellert, J. Thesinga, C. M. Heyl, and F. X. Kaertner
44-fs, 1-MHz, 70-μJ Yb-doped fiber laser system for high harmonic generation
Optics Express **32**, 39460 (2024)
`10.1364/OE.538748`

M. Togawa, J. Richter, C. Shah, M. Botz, J. Nenninger, J. Danisch, J. Goes, S. Kuehn, P. Amaro, A. Mohamed, Y. Amano, S. Orlando, R. Totani, M. de Simone, S. Fritzsche, T. Pfeifer, M. Coreno, A. Surzhykov, and J. R. C. Lopez-Urrutia
Hanle Effect for Lifetime Determinations in the Soft X-Ray Regime
Physical Review Letters **133**, 163202 (2024)
`10.1103/PhysRevLett.133.163202`

H. Gies and J. Schirrmeister
Renormalization flow of nonlinear electrodynamics
Physical Review D **110**, 076010 (2024)
`10.1103/PhysRevD.110.076010`

M. Valialshchikov, F. Karbstein, D. Seipt, and M. Zepf
Numerical optimization of quantum vacuum signals
Physical Review D **110**, 076009 (2024)
`10.1103/PhysRevD.110.076009`

H. Abramowicz, M. A. Soto, M. Altarelli, R. Assmann, A. Athanassiadis, G. Avoni et. al.
Technical Design Report for the LUXE experiment
European Physical Journal-Special Topics **233**, 1709 (2024)
`10.1140/epjs/s11734-024-01164-9`

S. Ramakrishna, R. P. Schmidt, A. A. Peshkov, S. Franke-Arnold, A. Surzhykov, and S. Fritzsche
Interaction of vector light beams with atoms exposed to a time-dependent magnetic field
Physical Review A **110**, 043101 (2024)
`10.1103/PhysRevA.110.043101`

S.-X. Wang, C. Brandau, S. Fritzsche, S. Fuchs, Z. Harman, C. Kozhuharov, A. Müller, M. Steck, and S. Schippers
Breit interaction in dielectronic recombination of hydrogenlike xenon ions: storage-ring experiment and theory
European Physical Journal D **78**, 122 (2024)
`10.1140/epjd/s10053-024-00914-7`

R. Bernecker, B. Baghdasaryan, and S. Fritzsche
High-dimensional maximally entangled photon pairs in parametric down-conversion
Physical Review A **110**, 033718 (2024)
`10.1103/PhysRevA.110.033718`

J. P. Kennedy, M. Coughlan, C. R. J. Fitzpatrick, H. M. Huddleston, J. Smyth, N. Breslin, H. Donnelly, B. Villagomez-Bernabe, O. N. Rosmej, F. Currell, L. Stella, D. Riley, M. Zepf, M. Yeung, C. L. S. Lewis, and B. Dromey
Real-Time Observation of Frustrated Ultrafast Recovery from Ionization in Nanostructured SiO_2 Using Laser-Driven Accelerators
Physical Review Letters **133**, 135001 (2024)
`10.1103/PhysRevLett.133.135001`

S. Roeder, Y. Zobus, Z. Major, and V. Bagnoud
Improving the rising edge of the temporal contrast of PHELIX by spatial conditioning in an unfolded stretcher
Optics Express **32**, 35713 (2024)
`10.1364/OE.519252`

M. Togawa, S. Kuehn, C. Shah, V. A. Zaytsev, N. S. Oreshkina, J. Buck, S. Bernitt, R. Steinbruegge, J. Seltmann, M. Hoesch, C. H. Keitel, T. Pfeifer, M. A. Leutenegger, and J. R. C. Lopez-Urrutia
High-accuracy measurements of core-excited transitions in light Li-like ions
Physical Review A **110**, L030802 (2024)
`10.1103/PhysRevA.110.L030802`

H. Gies, P. Heinzel, J. Laufkoetter, and M. Picciau
Quantum field theories of relativistic Luttinger fermions
Physical Review D **110**, 065001 (2024)
`10.1103/PhysRevD.110.065001`

J. Correa, A. Ignatenko, D. Pennicard, S. Lange, S. Fridman, S. Karl, L. Lohse, B. Senfftleben, I. Sergeev, S. Velten, D. Prajapat, L. Bocklage, H. Bromberger, A. Samartsev, A. Chumakov, R. Ruffer, J. von Zanthier, R. Röhlsberger, and H. Graafsma
TEMPUS, a Timepix4-based system for the event-based detection of X-rays
Journal Of Synchrotron Radiation **31**, 1209 (2024)
`10.1107/S1600577524005319`

A. V. Maiorova, D. Karlovets, S. Fritzsche, A. Surzhykov, and Th. Stöhlker
Coulomb excitation of hydrogen atoms by vortex ion beams
New Journal Of Physics **26**, 093010 (2024)
`10.1088/1367-2630/ad73fd`

R. Mincigrucci, E. Paltanin, J.-S. Pelli-cresi, F. Gala, E. Pontecorvo, L. Foglia, D. DE Angelis, D. Fainozzi, A. Gessini, D. S. P. Molina, O. Stranik, F. Wechsler, R. Heintzmann, J. Rothhardt, L. Loetgering, G. Ruocco, F. Bencivenga, and C. Masciovecchio
Structured illumination microscopy with extreme ultraviolet pulses
Optics Express **32**, 30813 (2024)
`10.1364/OE.531302`

G. Visentin, A. Borschevsky, L. A. Viehland, S. Fritzsche, and M. Laatiaoui
Laser resonance chromatography of $^{229}Th^{3+}$ in He: An *ab-initio* investigation
Physical Review A **110**, 023105 (2024)
`10.1103/PhysRevA.110.023105`

T. Dong, Y. Z. Zhang, A. Liu, Y. K. Ho, and L. G. Jiao
The singlet S-wave resonances of He atom in dense quantum plasmas
Physics Of Plasmas **31**, 082118 (2024)
10.1063/5.0217126

A. Mukherjee and D. Seipt
Laser polarization control of ionization-injected electron beams and x-ray radiation in laser wakefield accelerators
Plasma Physics And Controlled Fusion **66**, 085001 (2024)
10.1088/1361-6587/ad5379

S. Kodgirwar, L. Loetgering, C. Liu, A. Joseph, L. Licht, D. S. P. Molina, W. Eschen, J. Rothhardt, and M. Habeck
Bayesian multi-exposure image fusion for robust high dynamic range ptychography
Optics Express **32**, 28090 (2024)
10.1364/OE.524284

F. Liu, S. Skruszewicz, J. Spaethe, Y. Zhang, S. Hell, B. Ying, G. G. Paulus, K. Murari, M. Khalil, E. Cormier, L. G. Jiao, S. Fritzsche, and M. Kubel
Exploring valence-electron dynamics of Xenon through laser-induced electron diffraction
Physical Review A **110**, 013118 (2024)
10.1103/PhysRevA.110.013118

L. Stoyanov, N. Dimitrov, F. Wiesner, M. Fedoruk, G. G. Paulus, and A. Dreischuh
Wavelength-tolerant generation of Bessel-Gaussian beams using vortex phase plates
Applied Optics **63**, 5699 (2024)
10.1364/AO.524178

M. Lenski, T. Heuermann, Z. Wang, C. Aleshire, C. Gaida, C. Jauregui, and J. Limpert
In-band pumped, Q-switched thulium-doped fiber laser system delivering 140 W and 7 mJ pulse energy
Optics Letters **49**, 4042 (2024)
10.1364/OL.528330

D. Freire-Fernandez, W. Korten, R. J. Chen, S. Litvinov, Y. A. Litvinov, M. S. Sanjari, H. Weick, F. C. Akinci, H. M. Albers, M. Armstrong, A. Banerjee, K. Blaum, C. Brandau, B. A. Brown, C. G. Bruno, J. J. Carroll, X. Chen, C. J. Chiara, M. L. Cortes, S. F. Dellmann, I. Dillmann, D. Dmytriiev, O. Forstner, H. Geissel, J. Glorius, A. Goergen, M. Gorska, C. J. Griffin, A. Gumberidze, S. Harayama, R. Hess, N. Hubbard, K. E. Ide, R. John, R. Joseph, B. Jurado, D. Kalaydjieva, Kanika, F. G. Kondev, P. Koseoglou, G. Kosir, C. Kozhuharov, I. Kulikov, G. Leckenby, B. Lorenz, J. Marsh, A. Mistry, A. Ozawa, N. Pietralla, Z. Podolyak, M. Polettini, M. Sguazzin, R. S. Sidhu, M. Steck, Th. Stöhlker, J. A. Swartz, J. Vesic, P. M. Walker, T. Yamaguchi, and R. Zidaro
Measurement of the Isolated Nuclear Two-Photon Decay in ^{72}Ge
Physical Review Letters **133**, 022502 (2024)
10.1103/PhysRevLett.133.022502

S. Ramakrishna, Z. W. Wu, A. V. Maiorova, and S. Fritzsche
Interaction of Hermite-Gaussian Beams with a Macroscopic Atomic Target
Annalen Der Physik **536**, 2400048 (2024)
`10.1002/andp.202400048`

G. Visentin, H. Ramanantoanina, A. Borschevsky, L. Viehland, B. Jana, A. Arya, S. Fritzsche, and M. Laatiaoui
Transport-property predictions for laser resonance chromatography on Rf^{+} $(Z = 104)$
Physical Review A **110**, 012805 (2024)
`10.1103/PhysRevA.110.012805`

L. Eisenbach, Z. Wang, J. Schulte, T. Heuermann, P. Russbueldt, R. Meyer, P. Gierschke, M. Lenski, M. Sugiura, K. Tamura, J. Limpert, and C. Haefner
Highly efficient nonlinear compression of mJ pulses at 2 µm wavelength to 20 fs in a gas-filled multi-pass cell
Journal Of Physics-photonics **6**, 035015 (2024)
`10.1088/2515-7647/ad4cc4`

V. Hariton, Y. Jiang, A. Schoenberg, M. Seidel, M. Wieland, M. J. Prandolini, I. Hartl, M. Drescher, and C. M. Heyl
UV 30 fs laser pulse generation using a multi-pass cell
Optics Letters **49**, 3769 (2024)
`10.1364/OL.527988`

J. Luetgert, P. Hesselbach, M. Schoerner, V. Bagnoud, R. Belikov, P. Drechsel, B. Heuser, O. S. Humphries, P. Katrik, B. Lindqvist, C. Qu, R. Redmer, D. Riley, G. Schaumann, S. Schumacher, A. Tauschwitz, D. Varentsov, K. Weyrich, X. Yu, B. Zielbauer, Z. Major, P. Neumayer, and D. Kraus
Temperature and structure measurements of heavy-ion-heated diamond using *in situ* X-ray diagnostics
Matter And Radiation At Extremes **9**, 047802 (2024)
`10.1063/5.0203005`

C. Shah, M. Togawa, M. Botz, J. Danisch, J. J. Goes, S. Bernitt, M. Maxton, K. Koebnick, J. Buck, J. Seltmann, M. Hoesch, M. F. Gu, F. S. Porter, T. Pfeifer, M. A. Leutenegger, C. Cheung, M. S. Safronova, and J. R. Crespo Lopez-Urrutia
High-precision Transition Energy Measurements of Neon-like Fe xvii Ions
Astrophysical Journal **969**, 52 (2024)
`10.3847/1538-4357/ad454b`

Y.-C. Wang, L. G. Jiao, A. Liu, Y. K. Ho, and S. Fritzsche
<i>p</i>-wave resonances in the exponential cosine screened Coulomb potential
Communications In Theoretical Physics **76**, 075501 (2024)
`10.1088/1572-9494/ad432d`

S. Velten, L. Bocklage, X. Zhang, K. Schlage, A. Panchwanee, S. Sadashivaiah, I. Sergeev, O. Leupold, A. I. Chumakov, O. Kocharovskaya, and R. Röhlsberger
Nuclear quantum memory for hard x-ray photon wave packets
Science Advances **10**, eadn9825 (2024)
`10.1126/sciadv.adn9825`

C. Shah, S. Kuehn, S. Bernitt, R. Steinbruegge, M. Togawa, L. Berger, J. Buck, M. Hoesch, J. Seltmann, M. G. Kozlov, S. G. Porsev, M. F. Gu, S. Porter, T. Pfeifer, M. A. Leutenegger, C. Cheung, M. S. Safronova, and J. R. C. Lopez-Urrutia
Natural-linewidth measurements of the 3C and 3D soft-x-ray transitions in Ni xix
Physical Review A **109**, 063108 (2024)
10.1103/PhysRevA.109.063108

S. Fritzsche, A. K. Sahoo, L. Sharma, Z. W. Wu, and S. Schippers
Merits of atomic cascade computations
European Physical Journal D **78**, 75 (2024)
10.1140/epjd/s10053-024-00865-z

P. Sikorski, A. G. R. Thomas, S. S. Bulanov, M. Zepf, and D. Seipt
Novel signatures of radiation reaction in electron-laser sidescattering
New Journal Of Physics **26**, 063011 (2024)
10.1088/1367-2630/ad4f06

Y.-C. Wang, J. Ma, L.-G. Jiao, and S. Fritzsche
Inner-shell ionization cross sections of atoms by positron impact
Communications In Theoretical Physics **76**, 065502 (2024)
10.1088/1572-9494/ad3907

Z. W. Wu, W. Liu, and S. Fritzsche
Angle-resolved linear polarization of characteristic lines following innershell $2p_{3/2}$ photoionization of atoms
European Physical Journal D **78**, 69 (2024)
10.1140/epjd/s10053-024-00859-x

L. Xu, F. M. Fernandez, L. G. Jiao, H. E. Montgomery Jr, Y. K. Ho, and S. Fritzsche
Revisiting the energy spectrum of the radial screened Coulomb potential
Physica Scripta **99**, 065404 (2024)
10.1088/1402-4896/ad42e5

Y. Ma, J. A. Cardarelli, P. T. Campbell, S. Fourmaux, R. Fitzgarrald, M. D. Balcazar, A. F. Antoine, N. F. Beier, Q. Qian, A. E. Hussein, B. Kettle, S. R. Klein, K. Krushelnick, Y. F. Li, S. P. D. Mangles, G. Sarri, D. Seipt, V. Senthilkumaran, M. J. V. Streeter, L. Willingale, and A. G. R. Thomas
Single-Shot Diagnosis of Electron Energy Evolution via Streaked Betatron X Rays in a Curved Laser Wakefield Accelerator
Physical Review Letters **132**, 225001 (2024)
10.1103/PhysRevLett.132.225001

F. C. Salgado, A. Kozan, D. Seipt, D. Hollatz, P. Hilz, M. Kaluza, A. Saevert, A. Seidel, D. Ullmann, Y. Zhao, and M. Zepf
All-optical source size and emittance measurements of laser-accelerated electron beams
Physical Review Accelerators And Beams **27**, 052803 (2024)
10.1103/PhysRevAccelBeams.27.052803

H. Nazary, M. Metternich, D. Schumacher, F. Neufeld, S. J. Grimm, C. Brabetz, F. Kroll, F.-E. Brack, A. Blazevic, U. Schramm, V. Bagnoud, and M. Roth
Towards ion stopping power experiments with the laser-driven LIGHT beamline
Journal Of Plasma Physics **90**, 905900302 (2024)
10.1017/S0022377824000576

S. Ringleb, M. Kiffer, M. Vogel, and Th. Stöhlker
Off-resonance electronic detection and cooling of ions in a Penning trap
European Physical Journal Plus **139**, 401 (2024)
10.1140/epjp/s13360-024-05183-2

F. Schuetze, L. Doyle, J. Schreiber, M. Zepf, and F. Karbstein
Dark-field setup for the measurement of light-by-light scattering with high-intensity lasers
Physical Review D **109**, 096009 (2024)
10.1103/PhysRevD.109.096009

Y. Azamoum, G. A. Becker, S. Keppler, G. Duchateau, S. Skupin, M. Grech, F. Catoire, S. Hell, I. Tamer, M. Hornung, M. Hellwing, A. Kessler, F. Schorcht, and M. C. Kaluza
Optical probing of ultrafast laser-induced solid-to-overdense-plasma transitions
Light-science & Applications **13**, 109 (2024)
10.1038/s41377-024-01444-y

H. Gies and K. K. K. Tam
Fermionic fixed-point structure of asymptotically safe QED with a Pauli term
European Physical Journal C **84**, 477 (2024)
10.1140/epjc/s10052-024-12766-x

V. Tympel, F. Machalett, Th. Stöhlker, L. Crescimbeni, T. Schoenau, D. Haider, T. Sieber, M. Schwickert, F. Schmidl, P. Seidel, M. Schmelz, R. Stolz, and V. Zakosarenko
High Inductance Cryogenic Current Comparators for Beamlines
Ieee Transactions On Applied Superconductivity **34**, 9500705 (2024)
10.1109/TASC.2024.3350610

J. J. Marsh, C. G. Bruno, T. Davinson, P. J. Woods, Z. Andelkovic, A. Braeuning-Demian, R.-J. Chen, S. F. Dellmann, P. Erbacher, S. Fedotova, O. Forstner, D. Freire-Fernandez, J. Glorius, A. Gumberidze, O. Hall, P.-M. Hillenbrand, F. Herfurth, G. Hudson-Chang, A. Kalinin, M. Lestinsky, Y. A. Litvinov, E. B. Menz, C. Nociforo, N. Petridis, A. Psaltis, S. Sanjari, M. Selina, U. Spillman, R. S. Sidhu, Th. Stöhlker, L. Varga, and G. Vorobjev
The first in-beam reaction measurement at CRYRING@ESR using the CARME array
European Physical Journal A **60**, 95 (2024)
10.1140/epja/s10050-024-01318-2

M. O. Herdrich, D. Hengstler, S. Allgeier, M. Friedrich, A. Fleischmann, C. Enss, S. Bernitt, T. Morgenroth, S. Trotsenko, R. Schuch, and Th. Stöhlker
Application of a metallic-magnetic calorimeter for high-resolution x-ray spectroscopy of Fe at an EBIT
Journal Of Physics B-Atomic Molecular And Optical Physics **57**, 085001 (2024)
10.1088/1361-6455/ad34a2

J. J. Abel, J. Apell, F. Wiesner, J. Reinhard, M. Wünsche, N. Felde, G. Schmidl, J. Plentz, G. G. Paulus, S. Lippmann, and S. Fuchs
Non-destructive depth reconstruction of Al–Al_2Cu layer structure with nanometer resolution using extreme ultraviolet coherence tomography
Materials Characterization **211**, 113894 (2024)
10.1016/j.matchar.2024.113894

Z. Geng, Z. Sun, Y. Chen, X. Lu, T. Tian, G. Cheng, and X. Li
Multi-input mutual supervision network for single-pixel computational imaging
Optics Express **32**, 13224 (2024)
10.1364/OE.510683

D. F. Dar and S. Fritzsche
Nonlinear interference and electron dynamics: Probing photoelectron momentum distributions in strong-field ionization
Physical Review A **109**, L041101 (2024)
10.1103/PhysRevA.109.L041101

S. Ebrahimzadeh, S. Adnan, Y. Li, V. F. Pecile, J. Fellinger, S. Salman, C. M. Heyl, I. Hartl, O. H. Heckl, and G. Porat
Spectrally tunable phase-biased NALM mode-locked Yb:fiber laser with nJ-level pulse energy
Journal Of Physics-photonics **6**, 02LT01 (2024)
10.1088/2515-7647/ad3d1b

Z. Major, U. Eisenbarth, B. Zielbauer, C. Brabetz, J. B. Ohland, Y. Zobus, S. Roeder, D. Reemts, S. Kunzer, S. Goette, D. Neidherr, J. Hornung, P. Kewes, D. Schumacher, D. Beck, P. Hesselbach, M. Malki, P. Neumayer, K. Weyrich, A. Tauschwitz, and V. Bagnoud
High-energy laser facility PHELIX at GSI: latest advances and extended capabilities
High Power Laser Science And Engineering **12**, e39 (2024)
10.1017/hpl.2024.17

Z. W. Wu, J. Q. Wang, Y. Li, Y. H. An, and S. Fritzsche
Relativistic R-matrix calculations for the photoionization of W^{61+} ions
Physics Of Plasmas **31**, 043301 (2024)
10.1063/5.0201766

T. Yan, L. G. Jiao, A. Liu, Y. C. Wang, H. E. Montgomery Jr, Y. K. Ho, and S. Fritzsche
Bound state energies and critical bound region in the semiclassical dense hydrogen plasmas
Physics Of Plasmas **31**, 042110 (2024)
10.1063/5.0185339

Z. W. Wu, Y. Li, and S. Fritzsche
Competition of the Breit interaction in angular anisotropy of Auger electrons
Physical Review A **109**, 032817 (2024)
10.1103/PhysRevA.109.032817

M. Kiffer, S. Ringleb, Th. Stöhlker, and M. Vogel
Resistive cooling of ions’ center-of-mass energy in a Penning trap on millisecond time scales
Physical Review A **109**, 033102 (2024)
10.1103/PhysRevA.109.033102

R. P. Schmidt, S. Ramakrishna, A. A. Peshkov, N. Huntemann, E. Peik, S. Fritzsche, and A. Surzhykov
Atomic photoexcitation as a tool for probing purity of twisted light modes
Physical Review A **109**, 033103 (2024)
`10.1103/PhysRevA.109.033103`

S. Fritzsche, L. Jiao, and G. Visentin
Rapid Access to Empirical Impact Ionization Cross Sections for Atoms and Ions across the Periodic Table
Plasma **7**, 106 (2024)
`10.3390/plasma7010008`

C. Sevilla-Gutierrez, V. R. Kaipalath, B. Baghdasaryan, M. Graefe, S. Fritzsche, and F. Steinlechner
Spectral properties of transverse Laguerre-Gauss modes in parametric down-conversion
Physical Review A **109**, 023534 (2024)
`10.1103/PhysRevA.109.023534`

Y.-C. Wang, L. G. Jiao, and S. Fritzsche
Generalized binary-encounter-Bethe model for electron impact ionization of atoms
Journal Of Physics B-Atomic Molecular And Optical Physics **57**, 045202 (2024)
`10.1088/1361-6455/ad285e`

F. Karbstein
Towards the full Heisenberg-Euler effective action at large N
Journal Of High Energy Physics **2024**, 180 (2024)
`10.1007/JHEP02(2024)180`

Y.-C. Wang, G. Visentin, L. G. Jiao, and S. Fritzsche
Acceleration correction to the binary-encounter Bethe model for the electron-impact ionization of molecules
Physical Review A **109**, 022804 (2024)
`10.1103/PhysRevA.109.022804`

R. Belikov, D. Merges, D. Varentsov, Z. Major, P. Neumayer, P. Hesselbach, M. Schanz, and B. Winkler
Fast Multi-Wavelength Pyrometer for Dynamic Temperature Measurements
International Journal Of Thermophysics **45**, 29 (2024)
`10.1007/s10765-023-03323-x`

W. Eschen, C. Liu, M. Steinert, D. S. P. Molina, T. Siefke, U. D. Zeitner, J. Kaspar, T. Pertsch, J. Limpert, and J. Rothhardt
Structured illumination ptychography and at-wavelength characterization with an EUV diffuser at 13.5 nm wavelength
Optics Express **32**, 3480 (2024)
`10.1364/OE.507715`

A. I. Bondarev, M. Tamanis, R. Ferber, G. Basar, S. Kroeger, M. G. Kozlov, and S. Fritzsche
Comparison of theory and experiment for radiative characteristics in neutral Thulium
Physical Review A **109**, 012815 (2024)
`10.1103/PhysRevA.109.012815`

B. Lei, B. Liu, M. Shi, A. Seidel, D. Seipt, M. Zepf, and B. Qiao
Shot-to-shot electron beam pointing instability in a nonlinear plasma bubble
Physical Review E **109**, 015204 (2024)
10.1103/PhysRevE.109.015204

A. Seidel, B. Lei, C. Zepter, M. C. Kaluza, A. Saevert, M. Zepf, and D. Seipt
Polarization and CEP dependence of the transverse phase space in laser driven accelerators
Physical Review Research **6**, 013056 (2024)
10.1103/PhysRevResearch.6.013056

M. Awad, A. Manna, S. Hell, B. Ying, L. Abrok, Z. Diveki, E. Cormier, B. Kiss, J. Boehmer, C. Ronning, S. H. Han, A. George, A. Turchanin, A. N. Pfeiffer, and M. Kübel
Few-cycle laser pulse characterization on-target using high-harmonic generation from nano-scale solids
Optics Express **32**, 1325 (2024)
10.1364/OE.508062

X. H. Ji, L. G. Jiao, A. Liu, Y. Z. Zhang, U. Thumm, and Y. K. Ho
Quantum dynamics of positron-hydrogen scattering and three-body bound state formation with an assisting laser field: predictions of a reduced-dimensionality model
Journal Of Physics B-Atomic Molecular And Optical Physics **57**, 015203 (2024)
10.1088/1361-6455/ad1d33

H. Yang, X. Liu, F. Zhu, L. Jiao, and A. Liu
Electron vortices generation of photoelectron of H_2^+ by counter-rotating circularly polarized attosecond pulses
Chinese Physics B **33**, 013303 (2024)
10.1088/1674-1056/ad011a

B. Zhang, X. Liu, F. Zhu, L. Jiao, and A. Liu
Electron vortex generations in photoionization of hydrogen atoms by circularly-polarized chirped attosecond pulses
Communications In Theoretical Physics **76**, 015502 (2024)
10.1088/1572-9494/ad1587

THESES

Alexander Kirsche
Exploring and pushing the boundaries of tunable and waveguide-based high harmonic sources
Dissertation
Friedrich-Schiller-Universität Jena; Physikalisch-Astronomische Fakultät, (December 2024).

S. Ramakrishna
Interaction of vector light with atoms
Dissertation
Friedrich-Schiller-Universität Jena; Physikalisch-Astronomische Fakultät, (November 2024).

Esther B. Menz
Preparation and realisation of first dielectronic recombination experiments at CRYRINGESR
Dissertation
Friedrich-Schiller-Universität Jena; Physikalisch-Astronomische Fakultät, (November 2024).

T. Morgenroth
S-EBIT commissioning
Dissertation
Friedrich-Schiller-Universität Jena; Physikalisch-Astronomische Fakultät, (November 2024).

H. Harsh
Bright and stable betatron beams from laser-driven plasma wakefield
Dissertation
Friedrich-Schiller-Universität Jena; Physikalisch-Astronomische Fakultät, (October 2024).

Wilhelm Eschen
Material-specific and high-resolution imaging using extreme ultraviolet ptychography
Dissertation
Friedrich-Schiller-Universität Jena; Physikalisch-Astronomische Fakultät, (October 2024).

Supriya Rajhans
Few-cycle laser pulses for compact plasma accelerators
Dissertation
Friedrich-Schiller-Universität Jena; Physikalisch-Astronomische Fakultät, (September 2024).

Fang Liu
Strong field dynamic in laser-induced processes
Dissertation
Friedrich-Schiller-Universität Jena; Physikalisch-Astronomische Fakultät, (September 2024).

Philipp Sikorski
Signatures of radiation reaction in electron-beam laser collisions
Masterarbeit
Friedrich-Schiller-Universität Jena; Physikalisch-Astronomische Fakultät, (July 2024).

Felix Wiesner
Spektroskopische Kohärenztomographie im extrem ultravioletten Spektralbereich
Dissertation
Friedrich-Schiller-Universität Jena; Physikalisch-Astronomische Fakultät, (May 2024).

Mohammed Almassarani
Sub-picosecond dynamics during relativistic laser-plasma interaction
Dissertation
Friedrich-Schiller-Universität Jena; Physikalisch-Astronomische Fakultät, (May 2024).